Università degli Studi di Pisa

DIPARTIMENTO DI INGEGNERIA CIVILE E INDUSTRIALE
Corso di Laurea Magistrale in Ingegneria Aerospaziale

Tesi di Laurea Magistrale

Large-Eddy Simulations of Wind Turbines

Candidato:
Umberto Ciri

Relatori:
Prof.ssa Maria Vittoria Salvetti
Prof. Stefano Leonardi

Anno Accademico 2014–2015

Acknowledgements

I first wish to thank my supervisors, Prof. Maria Vittoria Salvetti and Prof. Stefano Leonardi, for the opportunity they gave me to conduct this research and for the precious advice and teachings they provided throughout the work.

I also thank my fellow students at the Lab in Dallas, also including Prof. Giacomo Valerio Iungo, and in Pisa for useful discussions, support and for providing a pleasant atmosphere during working hours.

I also wish to express my sincere gratitude to the professors I have met in my classes at the University of Pisa who have contributed to my formation as an engineer, in particular to Prof. Guido Buresti.

Finally, I would like to thank my family and friends for their continous support over the years.

TACC is acknowledged for providing computational resources as well as The Univeristy of Texas at Dallas for providing support to this work.

Abstract

Over the past years the demand of energy from renewable sources has been increasing due to increased environmental awareness and foreseeable shortage of non-renewable energies. This has had a strong impact on wind energy power-plants. In fact in order to supply large quantities of energy high-density clusters of wind turbines have been designed.

However, the actual production has been lower than the expected because of wake interactions, which are more severe as more densely the turbines are placed, and turbulent motion. It follows that in order to optimize the power extraction from wind a deep understanding of wakes features and dynamics is required.

Historically employed engineering models do not provide such a detailed knowledge and their predictions on wakes characteristics may be quite erroneous due the simplifying assumptions they rely upon. Conversely Large-Eddy Simulations (LES) take into account the dynamics of wind turbine flows without making *a priori* hypotheses on airflow behaviour. Therfore LES results are expected to be more detailed and accurate.

In the present thesis, LES of wind turbine flows have been performed. The results obtained have been discussed and compared to the predictions of the simplified engineering models. The impact of the subgrid-scale (SGS) model, which is a key feature of LES, has also been investigated within the framework of eddy-viscosity subgrid-scale models.

Contents

List of Figures

List of Tables

Chapter 1

Introduction

The increasing environmental awareness and the shortage of long term fossil fuels provisions have stimulated an increasing interest in renewable energies. Among those, wind energy is widely regarded as one of the most promising alternative source of energy and is among the world's most rapidly expanding industries. According to the Wall Street Journal, wind power is the most effiecient source of electricity[1]

Despite these remarkable recent developments, harvesting power from wind is one of the oldest activities humans have carried out over the history. Sails are one of the oldest propulsion devices known by the men and date as far back as 4,000 years BC. Windmills have been used for more than 3,000 years to extract mechanical energy from wind for agricultural purposes and can be considered as the forerunners of modern wind turbines.

These latter machines have a different purpose, which is electricity production. First wind turbines were constructed by the end of the 19th century in Scotland and the United States. They were characterised by rotor diameters around 15-25 m, 10-20 kW generators and pioneristic designs. The evolution of these machines has been quite discontinous over the 20th with the development of new generations of turbines being mainly subjected to the world's current economical trends rather than the availability of new technologies. Renewed interest arose during the World War II because of the supply crises and in the 1970s because of the oil crisis of 1973.

Recently wind power industry has benefited from considerable governing subsidies in various countries of the world which has led to record growing rates because of environmental concerns and strategical interests in renewable energies. Accordingly the technological development has been remarkable. Today utility scale wind turbines have rotor sizes over 100 m and an installed capacity up to 7.5 MW.

In order to live up to the huge demand of energy wind turbines are today clustered in large areas, *wind farms*, with a cumulative production which can reach that of a nuclear powerplant[81]. However the overall production has been lower than the expected, with losses being around 10 to 20% of the total power output. Another major concern is the maintenance and reliability of these large wind parks, with wind turbines actually wearing sooner than predicted.

[1] `http://blogs.wsj.com/numbers/what-is-the-most-expandingcient-source-of-electricity-1754/`

The reason for these setbacks lies in the wake interactions which occur in wind farms. The wake generated by the upstream turbines creates a highly turbulent and inhomogenous flow. As a consequence waked turbines are subjected to fatiguing loads which reduce their lifespan. Moreover, the trailing turbines are also affected in terms of power production since in wakes less kinetic energy is left for energy conversion.

The challenge for wind farm designer and engineers to-date is to understand how to predict and control these wake effects in order to optimize power extraction and loading spectra. The tools which are more commonly used however give little physical insight into flow dynamics and their prediction can be misleading. These so-called *wake models* are often based on simplifying assumptions about flow behaviour which allows to obtain simple analytical relantionship. Though their reliability is limited because these assumptions are often found to be not verified in actual wind turbine flows, their use is so extended because they are very simple to be implemented and do not require significant computational resources.

In order to gain an adequate knowledge of wake interaction, a more accurate flow description is necessary. A detailed numerical description of the flow field past wind turbines, a so called *Direct Numerical Simulation* (DNS), is to-date beyond computer capabilities because of the wide range of scales which are involved and the high Reynolds number. Recently Large-Eddy Simulations (LES) have been applied to wind turbine flows [30, 31]. In LES only the large scales of the flow are simulated, while the small ones are modeled. In the LES approach the turbine rotor is generally not resolved in detail, but is represented with an actuator model. In practice, the turbine blades are replaced with the forces they apply to flow. The two most common model used are the Actuator Disk Model (ADM) [30, 31, 50, 67, 95], which distributes the forces uniformly over a disk corresponding to the area swept by the blades, and the Actuator Line Model (ALM) [86, 87, 28, 48], which distributes the forces over rotating lines mimcking the actual blades motion [83, 52].

LES have shown to have the potential of faithfully reproducing wake features, interaction with the atmospheric boundary layer [9, 1] and predicting overall performances [82]. The ALM has been proved to be the most accurate method presently disposible [94, 48], capable of capturing small scales structures characterising wind turbine wakes. On the other hand the ADM is computationally more efficient and has allowed the simulation of multiple aligned turbines [9] or wind farms [60, 96], even though examples in the literature exist also for the ALM [10].

Overall, the LES approach is definitely the most accurate tool presently disposible for the analysis of wind turbine flows. It provides several information on the flow field which are not accessible with simple wake models. LES have the potential of giving the physical insight in the flow aerodynamics which is necessary to understand, control and master flow mechanisms. This deep knowledge has an invaluable importance since it can be exploited for optimisation of existing wind farm in terms of production and durability as well as for siting and design of new clusters.

The main drawback of the LES is the dramatic increase in computational resources and times connected with its use. Large-eddy simulations of wind turbines requires modern high-performances parallel computers and simulations can take up to several days depending on mesh resolution. This has confined the use of LES to the academic world for fundamental research on wind turbine flows, preventing its diffusion in the industry where wake models still represent the standard methodology.

The aim of this thesis is to show that LES are nontheless necessary to correctly describe the flow past wind turbines and particularly wind farms. As it has been mentioned above, wake interaction plays a fundamental role in wind farm performances and an accurate simulation of wake evolution is thus necessary to carefully study this role. Wake models, because of the assumptions they are based on, do not furnish an accurate description and LES can be used to highlight this weakness and obtain accurate predictions.

In order to preserve the accuracy of the method and at the same time to limit as far as possible the computational requirements, a new turbine parametrisation, the Rotating Actuator Disk (RADM), has been developed. The turbine rotor is represented with a rotating disk over which the force are not distributed smoothly, but according to the actual blades position. The method can be considered as being intermediate between the ADM and the ALM both in terms of accuracy and computational resources.

Another aspect, specific to the LES approach, has been addressed. A key feature of LES is the subgrid-scale (SGS) model which is the way through which the small scale of the flow not directly represented are introduced in the simulation. Various models and hypotheses have been proposed and their influence on the results and validity have been analised in numerous studies and for different kind of flows (see [71]).

However this issue have never been sistematically analised for wind turbine flows. A recent exception is constituted by the work of Sarlak *et al.*[75]. Therein, however, it was concluded that the impact of the SGS model is low compared to that of other parameters. A similar study is carried out in the final part of this thesis. The originality of this analysis consists in the fact in the present simulations the turbine tower and nacelle are explicitly simulated and not represented through virtual forces. Santoni *et al.*[74] have shown that explicit consideration of tower and nacelle provides close agreement with experimental results whereas the virtual forces method do not. The aim of the analysis is then to investigate if this feature can affect the final results and a different impact than in [75] can be found.

The thesis is organised as follows. In Chapter 2 the numerical methodology for performing the simulation is described. A theoretical background on the LES framework and the SGS which will be considered afterwards is given. The turbine modeling is also described in detail.

In Chapter 3 a validation of the numerical code is performed with numerical simulations of the turbulent channel flow. This is classic study case for which well-established numerical and experimental data as well as theoretical results are available. Therefore it is a well-suited case to evaluate and assess the performances of the numerical code.

In Chapter 4 a brief account on the wake models is given. Their performances are then compared to that of Large-Eddy Simulations carried out for utility-scale wind turbine. The large amount of information obtained from these simulations is analysed so as to provide a brief outline of wind turbine wakes aerodynamics. A comparison of the predictions of the ALM and the RADM is presented.

In Chapter 5 the specific argument of the effect of the SGS modeling is addressed. Various models are considered and evaluated with the use of both *a priori* and *a posteriori* tests. Results are also compared with experimental measurements for a model wind turbine.

In Chapter 6 conclusions are presented.

Chapter 2

Numerical Methodology and Modeling

2.1 Physical model and governing equations

The flow around a wind turbine can be assumed as incompressible to a good approximation. This choice is usual in the literature and it is suggested by the low Mach numbers pertaining to wind turbines under normal operating conditions, which allow compressibility effects to be sensibly neglected.

The governing equations of the fluid motion are the *incompressible Navier-Stokes equations* [8, 4]:

$$\nabla \cdot \mathbf{u} = 0 \tag{2.1a}$$

$$\frac{\partial \mathbf{u}}{\partial t} + \mathbf{u} \cdot \nabla \mathbf{u} = -\frac{1}{\rho}\nabla p + \nu \nabla^2 \mathbf{u} \tag{2.1b}$$

where $\mathbf{u} = (u, v, w)$ is the velocity vector, p is the pressure, ρ the fluid density and ν the kinematic viscosity.

Equations (2.1) can be adimensionalised by choosing a length and a velocity scales – which, though in principle can be arbitrary, are usually selected such that they are characteristic of the problem under study –, denoted by L and U respectively.

This procedure yields the *non-dimensional* Navier-Stokes equations, which assume the following form:

$$\nabla_* \cdot \mathbf{u}^* = 0 \tag{2.2a}$$

$$\frac{\partial \mathbf{u}^*}{\partial t^*} + \mathbf{u}^* \cdot \nabla_* \mathbf{u}^* = -\nabla_* p^* + \frac{1}{Re}{\nabla_*}^2 \mathbf{u}^* \tag{2.2b}$$

Quantities denoted by * represents non-dimensional quantities, for instance:

$$\mathbf{u}^* = \frac{\mathbf{u}}{U} \qquad t^* = \frac{tL}{U} \qquad p^* = \frac{p}{\rho U^2}$$

and:

$$[\nabla_*]_i = \frac{\partial}{\partial x_i^*} \qquad \text{with} \qquad x_i^* = \frac{x_i}{L}$$

while Re is the Reynolds number, defined as: $Re = UL/\nu$, and is the only similarity parameter which appears in Equation (2.2).

As a consequence, according to the dynamic similarity principle [41], two flows – geometrically similar –, having the same Re, will obey exactly the same equations, Eq. (2.2), and thus will have the same solution in terms of non-dimensional variables: this feature enlightens the power of the non-dimensional approach and constitutes one of the reason why it is so widely employed in various branches of Physics.

Since all the analysis in the following has been conducted within the framework of the non-dimensional Navier-Stokes equations, for the sake of simplicity of notation, the super-script '*' will be henceforth omitted and all quantities are meant to be conveniently adimensionalised with the appropriate length and velocity scale.

2.2 Numerical Code

Discretisation of Equations (2.2) is required in order to obtain a numerical solution.

The discretisation method, described in [61] and [62], consists of a second-order central finite-difference approximation on a Cartesian orthogonal grid for the spatial derivatives. Time advancement is obtained with a fractional step method which employs Cranck-Nicolson scheme for the linear terms, treated implicitly, and low-storage Runge-Kutta for the non-linear convective term which is treated explicitly.

The large sparse matrix resulting from the implicit terms is then inverted by an approximate factorization technique and a projection method is employed for the pressure correction.

The grid is staggered, i.e. flow variables are defined at different points of the computational cell: such a choice allows to avoid spurious pressure modes in the solution of the Navier-Stokes equations and to increase numerical accuracy while keeping the scheme compact [18].

Velocities are defined at the centre of the faces, while the pressure is computed at the centre of the cell. Vorticity is thus naturally computed at the edges of the cell and each variable may then be computed at the desired position by linear interpolation.

The computational cell is shown, together with the location of the velocity components and pressure, in Figure 2.1.

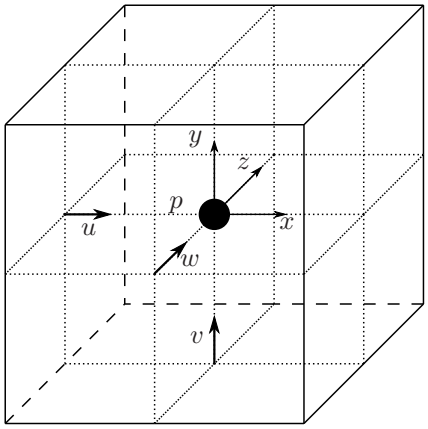

Figure 2.1: Grid cell with staggered velocities.

2.2.1 Discretisation schemes

In this section details are given on the discretisation schemes and on the solution process to numerically evaluate the Navier-Stokes equations.

Linear terms

The linear terms are discretized in time through the Crank-Nicolson scheme, which approximates time derivatives by a centered scheme about the point $t = t_{n+\frac{1}{2}}$:

$$\frac{u_i^{n+1} - u_i^n}{\Delta t} + N_i(\mathbf{u}^n) = \left.\frac{\delta p}{\delta x_i}\right|_{t=t_{n+\frac{1}{2}}} + \frac{1}{Re} L_{jj}\left(\frac{u_i^{n+1} + u_i^n}{2}\right) \tag{2.3}$$

where $\dfrac{\delta}{\delta x_i}$ is the discrete gradient operator – which employs, as reported above, centered finite-difference schemes – and L_{jj} is the discrete Laplacian operator.

The term $N_i(\mathbf{u}^n)$ indicates the non-linear convective term which is explicitly computed as a function of the solution u_i^n at time $t = t_n$; $\Delta t = t_{n+1} - t_n$ is the discrete time step.

Non-linear terms

The non-linear terms, which are the convective transport terms in Eq. (2.2b), are treated in explicit form which is easy to implement and permits to avoid linearisation which decreases the overall accuracy.

The scheme used is a low-storage third-order Runge-Kutta method. This method was developed by A. Wray in 1972 [35]. The convective term is advanced from time $t = t_n$ to time $t = t_{n+1}$ using three intermediate steps (*fractional steps*) which guarantee third-order accuracy in time and also increase the

stability of the numerical scheme, as it will be discussed later.

The scheme is said to be low-storage because it is build such that it requires the same memory storage of a second-order scheme, while actually being third-order accurate: in this sense, the scheme can be regarded as being computationally very efficient.

At each intermediate step l the updated solution is computed as:

$$u_i^{l+1} = u_i^l + \rho_l \Delta t \, N_i(\mathbf{u}^l) + \gamma_l \Delta t \, N_i(\mathbf{u}^{l-1}) \qquad l = 0, \ldots, 2 \tag{2.4}$$

with $u_i^{l=0} = u_i^n$ and $u_i^{l=3} = u_i^{n+1}$. The coefficient ρ_i and γ_i can be determined resorting to the Taylor expansion for u_i^{n+1} centered in u_i^n up to the third order.

The coefficient ρ_0 is set equal to zero because at the first step no previous information are known other then the starting solution u_i^n.

By summing Equations (2.4) for each time step l and comparing with the Taylor approximation one obtains a system for five of the unknown coefficients which has among the possible solutions the following employed in the present code:

$$\begin{aligned} &\rho_0 = 0 \qquad \rho_1 = -\frac{17}{60} \qquad \rho_2 = -\frac{5}{12} \\ &\gamma_0 = \frac{8}{15} \qquad \gamma_1 = \frac{5}{12} \qquad \gamma_2 = \frac{3}{4} \end{aligned} \tag{2.5}$$

Solution procedure and pressure correction

Merging the discretisation schemes in Equations (2.3) and (2.4) one obtains the completely discretized momentum balance.

However, care must be taken when merging the two schemes that the time advancement is consistent, i.e. the same for the linear and non linear terms. This may be accomplished by centering the Crank-Nicolson scheme around the step $l + \frac{1}{2}$ for each Runge-Kutta fractional step. The discrete time step Δt_l may then be computed as:

$$\Delta t_l = \alpha_l \Delta t \tag{2.6}$$

with

$$\alpha_l = \rho_l + \gamma_l \tag{2.7}$$

The discrete counterpart of Equation (2.2b) assumes the form:

$$\frac{u_i^{l+1} - u_i^l}{\Delta t} + \rho_l \, N_i(\mathbf{u}^l) + \gamma_l \, N_i(\mathbf{u}^{l-1}) = -\frac{\delta p}{\delta x_i}\bigg|_{l+\frac{1}{2}} + \alpha_l \frac{1}{Re} L_{jj}\left(\frac{u_i^{l+1} + u_i^l}{2}\right) \tag{2.8}$$

Direct integration of Equation (2.8) is prevented only by the fact that the pressure field is known only at time $t = t_l$ and not at time $t = t_{l+\frac{1}{2}}$.

This may be overcame by using a projection method, which consists in solving Eq. (2.8) with the (known) pressure field at time $t = t_l$ for an intermediate, *non-solenoidal*, velocity field $\hat{u}_i$ and then in projecting $\hat{u}_i$ onto a solenoidal space and updating $p|_{t=t_{l+1}}$ accordingly.

By introducing the variable $\Delta u_i = \hat{u}_i - u_i^l$, Eq. (2.8) may be recast in the following form:

$$\frac{\Delta u_i}{\Delta t} + \frac{\alpha_l}{Re} L_{jj}\left(\frac{\Delta u_i}{2}\right) = -\left.\frac{\delta p}{\delta x_i}\right|_l - \rho_l\, N(\mathbf{u}^l) - \gamma_l\, N(\mathbf{u}^{l-1}) + \frac{\alpha_l}{Re} L_{jj}(u_i^l) \quad (2.9)$$

$$\left(\delta_{ii} + \frac{\alpha_l \Delta t}{2Re} L_{jj}\right) \Delta u_i = b_i \quad (2.10)$$

where b_i embodies all the (known) terms in the right-hand side of Equation (2.9) and δ_{ii} is the conventional Kronecker's delta.

Due to the stencil of the centered second order approximation employed for the discretisation of spatial derivatives, the matrix resulting from the implicit terms on the left-hand side of Equation (2.10) is a seven-diagonal sparse matrix.

Given the dimension which usually reaches such matrix for well-resolved simulations an exact inversion would result in too high computational costs. As a consequence an approximate factorisation scheme [36] in three steps is adopted:

$$\begin{aligned}
\left(I + \frac{\alpha_l \Delta t}{2Re} L_{1\,1}\right) \Delta \mathbf{u}^{**} &= \mathbf{b} \\
\left(I + \frac{\alpha_l \Delta t}{2Re} L_{2\,2}\right) \Delta \mathbf{u}^{*} &= \Delta \mathbf{u}^{**} \\
\left(I + \frac{\alpha_l \Delta t}{2Re} L_{3\,3}\right) \Delta \mathbf{u} &= \Delta \mathbf{u}^{*}
\end{aligned} \quad (2.11)$$

where L_{ii} represents the discrete second derivative operator in the i-th direction. The matrix resulting from the implicit terms involves only three diagonals different from zero for each intermediate step. This makes the inversion feasible at a resonable expense in terms of memory and computations.

In order to obtain the solution $\mathbf{u}^{n+1}$ from $\hat{\mathbf{u}} = \Delta \mathbf{u} - \mathbf{u}^n$ a scalar quantity ψ is used to project $\hat{\mathbf{u}}$ onto a solenoidal space:

$$\mathbf{u}^{n+1} = \hat{\mathbf{u}} - \Delta t \nabla \psi \quad (2.12)$$

The scalar ψ is determined by solving a Poisson equation derived from the divergence of Eq. (2.12):

$$\nabla^2 \psi = \nabla \cdot \nabla \psi = \nabla \cdot \hat{\mathbf{u}} \quad (2.13)$$

Using Eq. (2.12) into Eq. (2.8) permits to compute the new pressure field compatible with a solenoidal velocity as:

$$p^{n+1} = p^n - \psi + \frac{\alpha_l \Delta t}{2Re} L_{jj}(\psi) \tag{2.14}$$

This procedure, Eqs. (2.12)-(2.14), is equivalent to enforce the continuity equation, Eq. (2.2a), which is required for the *discrete* numerical scheme in order to accurately represents the physical, *continous*, model and also shows the role of the pressure in incompressible flows as the enforcer of mass conservation.

2.2.2 Accuracy and Stability

The numerical scheme is second-order accurate in space and time. The Runge-Kutta method used for the discretisation of the convective term is actually third-order accurate in time. Although these higher precision is lost in the complete scheme, it must be recalled that the scheme is low-storage and thus there is no greater computational burden from the memory viewpoint. Furthermore, the real advantage in using this method is rather in the stability globally achieved by the numerical scheme.

In fact, due to the explicit treatment of the convective terms, the so-called CFL condition – named after Courant, Friedrichs and Lewy [13] – applies, i.e.:

$$\mathrm{CFL} = \left| \frac{u_i \Delta t}{\Delta x_i} \right|_{max} \leq 1 \tag{2.15}$$

This limit states that, for the solution to be stable, the (maximum) distance travelled by a material particle in a time step must be smaller than the mesh size and thus acts as a severe constraint on the amplitude of the time step Δt: as the grid is refined the CFL condition becomes more and more limiting.

Using a fractional step Runge-Kutta method allows to relax this condition and one can afford a larger CFL number. For the present three steps method, in fact, the CFL condition actually is formulated as

$$\mathrm{CFL} \leq \sqrt{3} \approx 1.7$$

A larger CFL number allows to use a larger time step Δt, given the mesh size, and therefore allows to reduce the computational time.

It should be noted that condition (2.15) is rigorously derived considering a pure advection problem: including the viscous terms, which appear in the Navier-Stokes equations, acts to stabilise the solution thus to further expand the CFL limit.

Implicit treatment of the convective term would permit to avoid the CFL limit, but this solution is quite laboured due to the non-linearity of the term.

Another restriction which has to be considered is the one related to the explicit treatment of the viscous term [64]:

$$\frac{\Delta t}{\Delta x^2 Re} \leq \frac{1}{2n} \tag{2.16}$$

where n expresses the dimensionality of the problem. This condition basically states that information diffused by the viscous term $\nu\nabla^2\mathbf{u}$ must not propagate for more than one cell-grid size in one time step. This limit becomes particularly severe for tri-dimensional low Reynolds number flows. In this case, given that the viscous term is linear, implicit treatment is a feasible effective way to overcome this limit.

2.2.3 Immersed Boundary

The presence of tower and nacelle in the computational domain is taken into account through the use of the efficient Immersed Boundary Method (IBM).

This method is very versatile since it allows to retain structured grid for describing bodies of complex geometry without recurring to computationally expensive body-fitted curvilinear grids or unstructured meshes. It allows treatment of moving bodies inside the domain without major numerical complications and with no need of re-meshing which is a cumbersome and long procedure when employing different techniques.

The method presently implemented is due to Leonardi [62] and it is developed from the formulation of Mohd-Yusof [53] and Fadlun [17].

The method essentially consists in prescribing in the grid points occupied by the body volume the value of the velocity according to desired boundary condition:

$$\mathbf{u}^{l+1} = \mathbf{V}_{\text{body}} \tag{2.17}$$

While it is relatively easy to treat the interior volume of the body, particular care must be taken when dealing with its boundaries. In fact, unless special recipies are adopted, one would describe a body with a step-wise contour leading inaccurate results, especially when the mesh is not fine (see Figure 2.2).

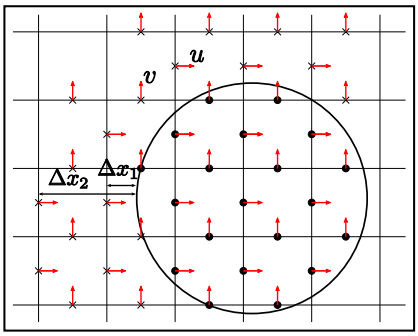

Figure 2.2: Immersed Boundary Method for a $2D$ cylinder: • points inside the body, × points outside the body; Δx_1andΔx_2 indicates the body's contour corrections for first and second derivatives.

As proposed in [43] and [44] the real contour of the body is simulated by replacing the computational mesh distance with the effective distance from the real boundary of the body when computing spatial derivatives that involve points across the body boundaries, Fig. 2.2.

2.3 LES Approach

In order for the numerical simulation to be accurate and physically sound, the discretisation of the Navier-Stokes equations should be fine enough to include in the computation all the relevant time-space scales of the flow under examination.

This means that grid size Δx, and consequently the time step Δt, must be small enough to be able to describe the dynamics of the smallest scales of the flow.

This requirement, which would lead to a so-called *Direct Numerical Simulation* (DNS), may become too challenging to accomplish when a very large range of scales characterises the problem under study: this is definitely the case for turbulence problems. For instance, in the case of isotropic homogeneous turbulence – which is the most studied case and the one for which analytical theories are available – it is possible to derive the ratio of the characteristic lengths of the biggest scale of the flow L to the smallest active one η (i.e. that one whose energy is still large enough to dynamically influence the flow and not to be dissipated by viscosity) within the framework of Kolmogorov theory [38]:

$$\frac{L}{\eta} = \mathcal{O}\left(Re^{3/4}\right) \tag{2.18}$$

Analogously, the ratio of the characteristic times is obtained as follows

$$\frac{T}{t_\eta} = \mathcal{O}\left(Re^{1/2}\right) \tag{2.19}$$

As consequence, a three dimensional well-resolved DNS of isotropic homogeneous turbulence would require at least $\mathcal{O}\left(Re^{11/4}\right)$ unknowns [71, 72].

Equations (2.18)-(2.19), despite being derived for isotropic homogeneous turbulence, represent a fairly good estimate for other types of flows, such as those of engineering interest which are usually anisotropic and inhomogeneous. If one considers that a modern utility scale wind turbine may have a diameter D as large as 100 m and a design wind speed U around $10\,\mathrm{m\,s^{-1}}$, the Reynolds number $Re = UD/\nu$ is of the order $\mathcal{O}(10^8)$. It is clear that, despite the disposal of modern powerful computers, a DNS of wind turbine flow is still beyond present capabilities.

A possible solution to overcome this problem, is the *Large-Eddy Simulation* (LES) approach. The LES approach basically consists in solving only the large scales (the *largest eddies* precisely) which contain most of the energy in flow and which are supposed to be characteristic and directly linked to the particular problem under study.

The smallest scales – which, on the contrary, are considered to be *universal* or, at least, not closely related to the particular flow – are modeled with the *resolved* (simulated) scales.

These assumptions lead to *local isotropy hypothesis*, i.e. that the small scales are independent of the flow and thus, being universal, are isotropic and statiscally homogeneous.

This hypothesis holds better as far as the Reynolds number is greater: in fact, in this case the viscous stresses – responsible for the kinetic energy dissipation

and thus determining the magnitude of the Kolmogorov dissipative scale η – would be significant at very small scales since at bigger scales the convective effects are predominant.

This means that the energy cascade process, which progressively transfers the energy contained in the large scales, would be long and thus it is reasonable to assume that the vortical structures, as their scale decrases and the energy is transferred, lose memory of the large anisotropic flow-dependent eddies and thus becomes locally isotropic [72].

This feature justifies the LES philosophy and makes the modeling effort more rational since it is not an *ad hoc* accommodation to resolve a particular case but is contextualized within a more general framework.

2.3.1 Filtered Navier-Stokes Equations

The scale separation to identify the resolved scales is performed by applying a filtering operation to the Navier-Stokes equations.

The filter is a mathematical tool which allows to remove all the scale lower than a selected cut-off scale (scale high-pass filter or, equivalently, frequency low-pass filter). It is defined as a convolution product between the physical variable $\phi(\boldsymbol{x}, t)$ and the filter kernel $G(\boldsymbol{x}, t)$:

$$\overline{\phi}(\boldsymbol{x}, t) = \int_{-\infty}^{+\infty} \int_{-\infty}^{+\infty} G(\boldsymbol{x} - \boldsymbol{\xi}, t - t')\phi(\boldsymbol{\xi}, t') \, \mathrm{d}t' \, \mathrm{d}\boldsymbol{\xi} \tag{2.20}$$

where $\overline{\phi}(\boldsymbol{x}, t)$ is the *filtered*, resolved, variable. The unresolved part of $\phi(\boldsymbol{x}, t)$ is denoted by a prime and is defined as:

$$\phi'(\boldsymbol{x}, t) = \phi(\boldsymbol{x}, t) - \overline{\phi}(\boldsymbol{x}, t) \tag{2.21}$$

The filter kernel is associated with a length cutoff scale $\overline{\Delta}$ and a time cutoff scale τ_c and is required to meet some properties such as linearity, conservation of constants and commutation with derivatives [71].

Application of Eq. (2.20) to the Navier-Stokes equations, Eqs. (2.1), yields the *filtered* Navier-Stokes equations:

$$\frac{\partial \overline{u}_i}{\partial x_i} = 0 \tag{2.22a}$$

$$\frac{\partial \overline{u}_i}{\partial t} + \frac{\partial}{\partial x_j}\left(\overline{u}_i \overline{u}_j\right) = -\frac{\partial \overline{p}}{\partial x_i} + \frac{1}{Re}\frac{\partial^2 \overline{u}_i}{\partial x_j \partial x_j} + \frac{\partial \tau_{ij}}{\partial x_j} \tag{2.22b}$$

where τ_{ij} is the so-called subgrid-scale (SGS) tensor which represents the interaction between the resolved scales and the unresolved ones which otherwise would not be present in the simulation. The subgrid tensor is defined as:

$$\tau_{ij} = \overline{u_i u_j} - \overline{u}_i \overline{u_j} \tag{2.23}$$

The appearance of this term in Equation (2.22b) is due to the non-linearity of the convective term and reflects the coupling between the large resolved eddies and small scales. Considering the filtered convective term and definitions (2.20) and (2.21) one can write:

$$\begin{aligned}\overline{u_i u_j} &= \overline{\left(\bar{u}_i + u'_i\right)\left(\bar{u}_j + u'_j\right)} \\ &= \overline{\bar{u}_i \bar{u}_j} + \overline{\bar{u}_i u'_j} + \overline{u'_i \bar{u}_j} + \overline{u'_i u'_j} \\ &= \overline{\bar{u}_i \bar{u}_j} + C_{ij} + R_{ij} \end{aligned} \tag{2.24}$$

where $C_{ij} = \overline{\bar{u}_i u'_j} + \overline{u'_i \bar{u}_j}$ is the *cross-stress tensor* which represents the interactions between the resolved and the subgrid scales, while $R_{ij} = \overline{u'_i u'_j}$ is the *SGS Reynolds tensor* which represents the interactions among the subgrid modes.

From a theoretical point of view it should possible to evaluate all the terms which appear in the filtered momentum equation directly from the filtered field itself. Since the term $\overline{\bar{u}_i \bar{u}_j}$ would require a second application of the filter, Eq. (2.24) can be further manipulated into:

$$\overline{u_i u_j} = \overline{u}_i \overline{u}_j + L_{ij} + C_{ij} + R_{ij} \tag{2.25}$$

where $L_{ij} = \overline{\bar{u}_i \bar{u}_j} - \overline{u}_i \overline{u}_j$ is the *Leonard tensor*, which represents the interactions among the resolved scales. The subgrid tensor is then composed of three contributions:

$$\tau_{ij} = L_{ij} + R_{ij} + C_{ij} \tag{2.26}$$

This is the so-called Leonard triple decomposition, named after Leonard who first proposed this viewpoint in 1974[42], and it provides a physical interpretation of the mechanisms which the SGS tensor accounts for. This is not the only 'interpretation' of the SGS term since other decompositions are possible based on different observations or definitions. Examples are the Leonard double decomposition[42], which arises from Eq. (2.24), or the Germano consistent decomposition[22] which is formally identical to Eq. (2.26) and can be seen as a generalization of the Leonard triple decomposition[71].

To close the system of equations (2.22) the subgrid tensor has to be modeled as function of the filtered velocity field $\overline{\mathbf{u}}$.

Before giving a description of some of the various SGS models developed over the years, some remarks should be made over operation (2.20) and the interpretation of the results obtained with Eqs (2.22) respect to those arising from a DNS.

Though many filters can be built rather easily which have the required properties [71], explicit application of Equation (2.20) is seldom performed, mostly because of its high computational expense.

The filtering operation is instead meant to be implicitly applied by the computational grid.

This procedure has the advantage of being completely inexpensive from a computational point of view and exploit the sampling effect of the computational grid which, due to Nyquist theorem, is equivalent to the application of filter with cut-off frequency $f_c = 1/(2\Delta x)$ – or, as more common, with cut-off wavenumber $k_c = \pi/\Delta x$ – and thus filters out all the structures of scale lower than the grid spacing.

The choice of the mesh size has to ensure that the cut-off includes all the dynamically active scales of the flow, i.e. the cut-off wavenumber has to be in

the dissipative range of the energy spectrum of the solution. Of course, this size Δx is not known *a priori* and that is a potential source of error in the numerical simulation. Grid independence studies are performed to check the convergence of the solution

Another common problem which may arise especially when simulating complex geometries is related to the topology of the grid: if the grid, or the filter, is not uniform then commutation with the derivatives is not guaranteed and this generates a commutation error.

In this case the error should be eliminated or controlled, for example by employing high-order commuting, explicit, filters [89].

2.3.2 Subgrid-Scale Modeling

The filtering operation removes a number of degrees of freedom from the solution of the Navier-Stokes equations which however still have an effect on it due to the non-linearity of the convective term which gives rise to the appearance of an extra term in the momentum balance: expressing this term as function of the filtered solution is often referred to as the closure problem of LES [45], which many reaserchers have tackled over the years through their modeling efforts.

In the following we focus on the so-called *eddy-viscosity models*. These models describe the effects of the SGS terms analogously to the viscous mechanisms which take place at a molecular level in the fluids such as momentum or thermal exchanges.

In practice the motion of the subfilter eddies is assumed to be analogous to the Brownian motion of the molecules and the interactions which in the gaskinetic theory occur at *microspic* level in turbulent motions are assumed to occur at *macroscopic* level and to be relevant to the fluid particle.

As the molecular viscosity ν characterises those phenomena, so a subgrid, or eddy, viscosity ν_{sgs} is defined to characterise the turbulent energy cascade. According to the so-called Boussinesq's hypothesis [45, 19], the deviatoric part[1] of the subgrid stress tensor is the expressed as a function of the symmetric part of the velocity gradient tensor (rate of strain tensor):

$$\tau^d = -\nu_{\text{sgs}} \left(\nabla \overline{\mathbf{u}} + \nabla^t \overline{\mathbf{u}} \right) \tag{2.27}$$

where the superscript 't' indicates the transpose operator. Notice that with definition (2.27) the structure which describes the interactions between the resolved and unresolved scales is exactly the same as that which accounts for the viscous stresses:

$$\nu \nabla^2 \mathbf{u} = \nabla \cdot \left[\nu \left(\nabla \mathbf{u} + \nabla^t \mathbf{u} \right) \right]$$

as assumed by the eddy-viscosity hypothesis.

The major drawback of this formulation, which on the other hand is based on sensible physical arguments, is that the subgrid tensor principal axes are parallel to those of the strain rate tensor and this is not the case for many types of flows [72, 71].

Other approaches are possible, such as the mixed models [2, 97, 73], gradient models [11, 47] and others (see [71] for a review), and often the choice of the employed model depends upon a number of factors such as the type of flow, the computational resources or the authors' expertises in treating one model.

Smagorinsky model

Historically, the first model which has been proposed, and still today one of the most used, is the one described by Joseph Smagorinsky in 1963 [79].

The subgrid viscosity is modelled as:

$$\begin{aligned} \nu_{\text{sgs}} &= \left(C_s\overline{\Delta}\right)^2 \sqrt{2\overline{S}_{ij}\overline{S}_{ij}} \\ &= \left(C_s\overline{\Delta}\right)^2 \left|\overline{S}\right| \end{aligned} \tag{2.28}$$

where S_{ij} is the rate of strain tensor and C_s is the so-called Smagorinsky constant, which in general depends upon the type of flow and usually ranges between $C_s = 0.1$–0.2.

The simplicity of the model has contributed in making it successful as well as the fact that it allows to obtain quite good results. The reason for this is probably that the model well represents the globally dissipative nature of turbulence: in fact the subgrid dissipation provided by the model, defined as $\varepsilon = -\tau^d_{ij}\overline{S}_{ij}$, is by construction always positive, i.e. the subfilter modes drain energy from the large scale (*forward energy cascade*).

Although this well describes the average behaviour of turbulence, it must be pointed out, however, that locally the dissipation could be negative (*backscatter* or *backward energy cascade*), that is the subgrid modes provide energy to the resolved ones: this mechanism is not considered by the Smagorinsky model and that may be a problem when a detailed analysis of the flow features is sought.

Another major problem of the Smagorinsky model is its behaviour near a solid wall. Indeed very near the wall, the flow is always essentially laminar (see Section 3.3) and the subgrid, turbulent, viscosity is then expected to vanish as a suitable power of the distance from the wall.

Without loss of generality, let us consider a solid wall in (x, z) plane at $y = 0$; if one performs a Taylor expansion in the limit $y \to 0$ then, in virtue of the no-slip condition and of the incompressibility constraint, Eq. (2.1a), it is obtained:

[1] The decomposition is necessary since the strain rate tensor has zero trace. The isotropic, or sferic, part of the tensor $\frac{1}{3}\tau_{kk}\delta_{ij}$ which is not taken into account by $\tau^d_{ij} = \tau_{ij} - \frac{1}{3}\tau_{kk}\delta_{ij}$ is then lumped into the pressure term of the Navier-Stokes equation.

That is, the filtered pressure $\overline{p}$ is replaced by the modified pressure $p^\star$:

$$p^\star = \overline{p} + \frac{1}{3}\tau_{kk}$$

The subgrid contribution to the pressure may be significant and may be computed with the aid of some kind of estimate for the subgrid kinetic energy $q_{\text{sgs}} = \frac{1}{2}\tau_{kk}$

$$u(x,y,z,t) = a(x,z,t)y \ + o(y^2) \tag{2.29a}$$
$$v(x,y,z,t) = b(x,z,t)y^2 + o(y^3) \tag{2.29b}$$
$$w(x,y,z,t) = c(x,z,t)y \ + o(y^2) \tag{2.29c}$$

where a, b and c are functions which describe the space and time evolution of the velocity components but are not dependent on the distance from the wall (this is an approximation in the limit $y \to 0$). An analogous expression holds for the expansion of the filtered field since it has to respect the same boundary and incompressibility conditions:

$$\bar{u}(x,y,z,t) = \bar{a}(x,z,t)y \ + o(y^2) \tag{2.30a}$$
$$\bar{v}(x,y,z,t) = \bar{b}(x,z,t)y^2 + o(y^3) \tag{2.30b}$$
$$\bar{w}(x,y,z,t) = \bar{c}(x,z,t)y \ + o(y^2) \tag{2.30c}$$

From Eq. (2.27) with the scalings in Eqs. (2.29)-(2.30) it can be seen that the only way for the subgrid stresses τ^d_{xy} and τ^d_{yz} to vanish at the wall – and with the proper asyntotic behaviour – is that $\nu_{\text{sgs}} = o(y^3)$. At the same time, it is clear that if the eddy viscosity is given by Eq. (2.28) it remains finite as the distance from the wall diminishes.

A possible solution, which has been employed in the present simulations, is the adoption of the so-called Van Driest's damping [88] which modifies the constant C_s in the vicinity of the wall by means of a suitable damping function:

$$(C_s\Delta)^2_{\text{damped}} = \left[C_s\Delta\left(1 - e^{(y^+/A)}\right)\right]^2 \tag{2.31}$$

where $y^+ = u_\tau\delta/\nu$, where δ is the distance from the wall and $u_\tau = \sqrt{\tau_w}$ is the friction velocity (more details will be given in Section 3.2), and $A = 25$ is the Van Driest's constant.

This correction ensures that turbulent viscosity goes to zero as approaching a solid wall, but still not with the correct asymptotic behaviour which is $o(y^3)$.

Dynamic Model

The introduction by Germano *et al.* in 1991 [24] of the dynamic model represented a significant improvement in turbulence modeling: indeed, the dynamic procedure for computing the model constant allows to overcome some of the most critical problems of Smagorinsky.

The dynamic procedure requires the use of a second, necessarily explicit, filter, often referred to as the *test filter* (in contrast to the *grid filter*), and is based on a mathematical identity due to Germano [23].

From the definition of subgrid tensor, Eq. (2.23), if follows that the SGS tensor due to the application of the second filter is:

$$T_{ij} = \widetilde{\overline{u_i u_j}} - \tilde{\overline{u}}_i \tilde{\overline{u}}_j \tag{2.32}$$

where the $\tilde{\cdot}$ indicates the test filter level, of width $\tilde{\overline{\Delta}}$. The Germano identity states that:

$$\mathscr{L}_{ij} = T_{ij} - \tau_{ij} \tag{2.33}$$

where $\mathscr{L}_{ij} = \widetilde{\overline{u_i}\overline{u_j}} - \tilde{\overline{u}}_i \tilde{\overline{u}}_j$ is the so called Leonard tensor. It is important to notice that this latter term can be computed exactly from the filtered field.

At this point, if one assumes *scale invariance*, it is possible to describe the two subgrid tensors with same functional form. For example, by using the Smagorinsy model, Eq. (2.28), one can write:

$$\tau_{ij} - \frac{1}{3}\tau_{kk}\delta_{ij} = -2(C_d \overline{\Delta}^2)\left|\overline{S}\right|\overline{S}_{ij} \tag{2.34}$$

$$T_{ij} - \frac{1}{3}T_{kk}\delta_{ij} = -2(C_d \tilde{\overline{\Delta}}^2)|\tilde{\overline{S}}|\tilde{\overline{S}}_{ij} \tag{2.35}$$

Substituting Equations (2.34)-(2.35) into Eq. (2.33) one obtains six equations to determine the constant $C(\mathbf{x},t) = C_d(\mathbf{x},t)\overline{\Delta}^2$:

$$\mathscr{L}_{ij} - \frac{1}{3}\mathscr{L}_{kk}\delta_{ij} = 2C(\mathbf{x},t)M_{ij} \tag{2.36}$$

with

$$M_{ij} = \frac{\tilde{\overline{\Delta}}^2}{\overline{\Delta}^2}|\tilde{\overline{S}}|\tilde{\overline{S}}_{ij} - \widetilde{|\overline{S}|\overline{S}}_{ij} \tag{2.37}$$

Following the proposal of Lilly [46], in order to obtain one single relationship to determine the constant, we contract Eq. (2.36) with Eq. (2.37) and thus obtain:

$$C(\mathbf{x},t) = C_d(\mathbf{x},t)\bar{\Delta}^2 = -\frac{1}{2}\frac{\mathscr{L}^d_{ij}M_{ij}}{M_{kl}M_{kl}} \tag{2.38}$$

The subgrid tensor is then given by:

$$\tau^d_{ij} = -2C|\overline{S}|\overline{S}_{ij} \tag{2.39}$$

There is no more need to assign an input value to the model constant, since it is computed dynamically during the simulation. Furthermore, in principle, the model constant is computed tridimensionally, in every grid point, so that it can adapt to local condition of the flow: it can also be negative and thus account for backscatter of energy.

Also, the model constant is automatically adjusted to have to correct behaviour in proximity of a solid wall.

However the model still has some drawbacks which attenuate the advantages. In practice, the three-dimensional constant presents strong oscillations and may

remain negative for long periods: these features are critical for the numerical stability and thus some sorts of regularization procedures are needed.

Usually the numerator and denominator of Equation (2.38) are averaged along homogeneous directions (if they exist) or using other kind of average such as the Lagrangian average [49].

Also the subgrid viscosity is usually 'clipped' such that the total dissipation remains positve or equal to zero ($\nu + \nu_{\text{sgs}} \geq 0$).

These numerical recipes have the consequences that the local character of the constant is obviously lost and backscatter is considered only in an average sense, but nevertheless they are necessary for the stability of the simulation.

Other Eddy-Viscosity models

Besides the classical Smagorinsky model, some other static eddy-viscosity models have been considered in the present thesis for the reason that they are expected to have a better behaviour than the Smagorinsky model in the neighborhood of a solid wall without the need of a dynamic procedure, which involves an increase in the computational costs.

These models are simple to be implemented, since they involve only local quantities, but compared to the Dynamic model present the disadvantge, in their static version, of requiring as input parameter the specification of a model constant whose value is in general flow-dependent and quite arbitrary (as is the case for the static Smagorinsky model).

Those models, being part of the eddy-viscosity models family, have the structure reported in Eq. (2.27) and differ in the definition of the subgrid viscosity. One of the considered models is the Wall-Adapting Local-Eddy (WALE) model [59], in which the eddy-viscosity is given by:

$$\nu_{\text{sgs}} = (C_W \bar{\Delta})^2 \frac{(\overline{\mathscr{S}}^d_{ij} \overline{\mathscr{S}}^d_{ij})^{3/2}}{(\overline{S}_{ij}\overline{S}_{ij})^{5/2} + (\overline{\mathscr{S}}^d_{ij}\overline{\mathscr{S}}^d_{ij})^{5/4}} \tag{2.40}$$

where:

$$\overline{\mathscr{S}}^d_{ij} = \frac{1}{2}(g^2_{ij} + g^2_{ji}) - \frac{1}{3} g^2_{kk}\delta_{ij} \tag{2.41}$$

with $g^2_{ij} = g_{ik}g_{kj}$ being the square of the transpose of the velocity gradient tensor:

$$g_{ij} = \left(\nabla^t \mathbf{u}\right)_{ij} = \frac{\partial \overline{u}_i}{\partial x_j} \tag{2.42}$$

The model constant C_W has been evaluated numerically for isotropic turbulence and is reported by the authors to be in the range $C_W = 0.5 - 0.6$.

Another model is the one proposed by Vreman [91] which defines the eddy viscosity as:

$$\nu_{\text{sgs}} = C_V \sqrt{\frac{B_\beta}{\alpha_{ij}\alpha_{ij}}} \tag{2.43}$$

where

$$\alpha_{ij} = (\nabla \mathbf{u})_{ij} = \frac{\partial \overline{u}_j}{\partial x_i} \tag{2.44}$$

is the velocity gradient tensor while B_β is the second invariant of the matrix $\beta_{ij} = \bar{\Delta}^2 \alpha_{ki}\alpha_{kj}$. The model coefficient is related to the usual Smagorinsky constant by the formula:

$$C_V \approx 2.5 C_s^2 \tag{2.45}$$

and is obtained from a realizability condition for the subgrid dissipation within the framework of isotropic homogeneous turbulence [92].

Finally, the σ-model proposed by Nicoud *et al.* [58] has also been taken into account. The subgrid viscosity is defined in this case as:

$$\nu_{\text{sgs}} = (C_\sigma \bar{\Delta})^2 \frac{\sigma_3(\sigma_1 - \sigma_2)(\sigma_2 - \sigma_3)}{\sigma_1^2} \tag{2.46}$$

where σ_i are the singular value of the matrix $\nabla^t \mathbf{u}$. The model constant is evaluated numerically by comparison with the subgrid dissipation provided by the Smagorinsky model and is reported to be $C_\sigma \approx 1.35$.

As already stated above, all these models have a vanishing viscosity near a solid wall: in particular the WALE model, Eq. (2.40), and the σ-model, Eq. (2.46), present the correct asymptotic behaviour $o(y^3)$, while the Vreman model is only $o(y)$ which is, anyway, still better than the undamped Smagorinsky eddy-viscosity [58].

2.4 Turbine modeling

It is beyond the present computational resources to carry out a numerical simulation which can capture physical phenomena within such a wide range of scales as those which take place in wind farm and wind turbine aerodynamics: it is impossible to treat with the adequate accuracy the boundary layer which develops on the skin of the turbine blade and characterises the forces over the blade responsible of the power production and at the same time describing the dynamics of the large scale wake features which significantly affect the performance of downstream turbines in the aligned operational configuration.

Modeling the rotor effect on the flow field, instead of directly simulating the presence of the blades, has made numerical simulations of the flow past wind turbines feasible.

The two most popular models for wind turbine parametrization are the Actuator Disk Model (ADM) and the Actuator Line Model (ALM). They both replace the actual rotor with the forces it applies to the flow: while the ADM distributes the forces over a circular area corresponding to the area swept by the turbines blades, the ALM spreads the forces over a rotating line which mimics the rotor blade motion.

The ADM has been the first model to be employed in conjunction with LES [30] and counts several examples in the literature especially for the simulation of large array of wind turbines [96, 9, 50] due to its lower computational cost with respect to the ALM.

The ALM has been widely used as well [86, 87, 66, 67] and it is recognized as the most accurate method due to its capability of representing detailed features of the wind turbine wake [48].

In the present thesis a new model has been developed, the Rotating Actuator Disk Model (RADM), which, contrarily to the classic ADM formulation, takes explicitly into accounts the rotation of the blades and is thus expected to provide a more realistic description of the wake characteristics.

2.4.1 Actuator Line Model

The Actuator Line Model was introduced by Sørensen and Shen [83]. In the ALM approach each turbine blade is represented as a rotating line which is then divided into a number of discrete sections.

For each section of the line the blade forces per unit length, lift F_L and drag F_D are computed using a bidimensional approach as:

$$F_L = \frac{1}{2}\rho U_{\text{rel}}^2 C_L(\alpha) c \tag{2.47}$$

$$F_D = \frac{1}{2}\rho U_{\text{rel}}^2 C_D(\alpha) c \tag{2.48}$$

where C_L and C_D are respectively the blade's airfoil lift and drag coefficient, c is the airfoil's chord, α is the local angle of attack and U_{rel} is the relative velocity approaching the blade leading edge, see Figure 2.3

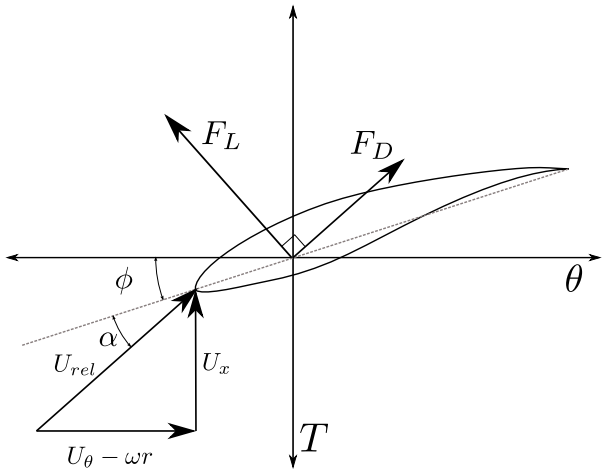

Figure 2.3: Blade cross-section in the $T-\theta$ plane, where T is the direction of the thrust force and θ is the azimuthal direction.

The relative velocity magnitude U_{rel} is obtained from the local flow velocity considering the effect of the rotational speed of the blade:

$$U_{\text{rel}} = \sqrt{U_x^2 + (U_\theta - \omega r)^2} \tag{2.49}$$

where ω is the rotational speed of the rotor and r the radial distance of the considered section from the rotor centre.

The angle of attack is computed as (Fig. 2.3):

$$\alpha = \arctan\left(\frac{U_x}{U_\theta - \omega r}\right) - \phi \tag{2.50}$$

where ϕ is the local twist angle of the blade. To consider the root and tip vortices the angle of attack is then corrected by means of modified Prandtl correction factor [5]:

$$F = \left(\frac{2}{\pi}\right)^2 \cos^{-1}\left(e^{-f_t}\right) \cos^{-1}\left(e^{-f_r}\right) \tag{2.51}$$

where

$$f_t = \frac{B}{2}\frac{D/2 - r}{r\sin(\alpha + \phi)} \qquad \text{and} \qquad f_r = \frac{B}{2}\frac{r - D_h/2}{r\sin(\alpha + \phi)} \tag{2.52}$$

where D_h is the nacelle diameter and B is the number of blades.

The forces computed with Eqs. (2.47)-(2.48) are then projected onto the computational axes as components of the vector $\mathbf{F}_{turb}$ and distributed among the nearest gridpoints within a cylinder with axis parallel to the actuator line according to a gaussian regularization kernel:

$$\eta = e^{-\left(\frac{r}{\epsilon}\right)^2} \tag{2.53}$$

$$\mathbf{f}_{turb} = \frac{\mathbf{F}_{turb}\,\eta}{\iint_{A_{cyl}} \eta \,\mathrm{d}A} \tag{2.54}$$

where r is the radial distance of the gridpoint from the centre of the blade (actuator line), ϵ a parameter which determines the spreading of the force and, consequently, the area of the cylider A_{cyl}. This is done because the application of singular point force is likely to cause numerical instabilities [48]. The issue of numerical stability is also important when the simulation time step Δt is concerned: indeed, in order to guarantee a smooth transition in the force application as the blade rotates, the time advancing is limited in order that at each time step the actuator line advances of one gridpoint. This is obtained by restricting the Courant number (see Section 2.2) $\text{CFL}_{\text{ALM}} = \text{CFL}/TSR$ where the tip speed ratio TSR is an important performance parameter of the turbine defined by:

$$TSR = \frac{\omega R}{U_\infty} \tag{2.55}$$

where $R = D/2$ is the blade radius and U_∞ is the freestream velocity impinging the blade.

2.4.2 Rotating Actuator Disk Model

With the RADM approach the force is computed exactly as in Eqs. (2.47)-(2.48) but is then spreaded by means of Gaussian function on the whole rotor area:

$$\eta = e^{-\left(\frac{x-x_c}{\epsilon}\right)^2} e^{-\left(\frac{\phi-\theta}{2\pi}\right)^2} \tag{2.56}$$

$$\mathbf{f}_{turb} = \frac{\mathbf{F}_{turb}\,\eta}{\iint_A \eta \,\mathrm{d}A} \tag{2.57}$$

where $x - x_c$ is the distance of the considered gridpoint in the streamwise direction from the rotor location x_c, ϵ is a spreading regulation parameter which determines the thickness of the disk and $\phi - \theta$ is the angular distance from the angular position of the blade θ; A is the annular ring over which the force is spreaded. Therefore, the distribution over the disk is not constant but depends on the radial and azimuthal coordinate of each gridpoint. As the blade moves, the section at which the forces are computed changes accordingly and thus the disk rotates.

In Figure 2.4 colour contours of the axial force (thrust) are reported for both the RADM and the ALM for qualitative comparison.

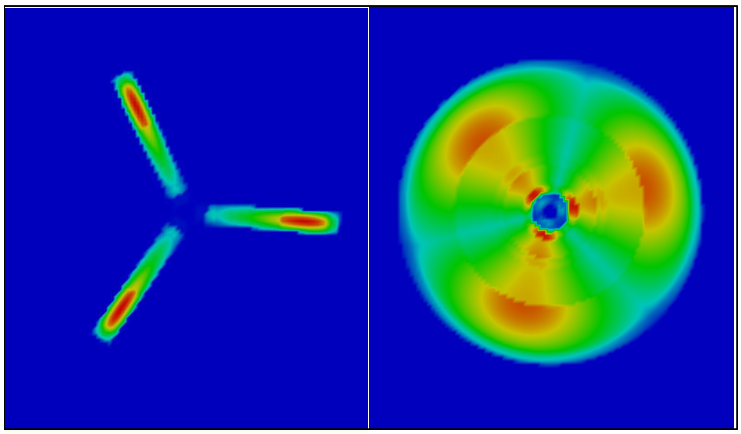

Figure 2.4: Thrust force: ALM (left), RADM (right). Colours level in the figure are different, the integral of the forces in the disk being equal to the integral of the forces over the 3 blades.

With the Rotating Actuator Disk Model the forces are distributed over a larger area and this greatly weakens the stability concerns encountered with the ALM. Furthermore, the field associated with the RADM in the rotor area is globally smoother, due to the enhanced force spreading, and this allows the use of larger time steps, thus diminishing the computational cost of the simulation which is the major drawback connected with the ALM approach.

However, this gain in computational time is associated with a loss of accuracy in depicting wake details such as, for instance, the tip vortex as can be

appreciated in Figure 2.5.

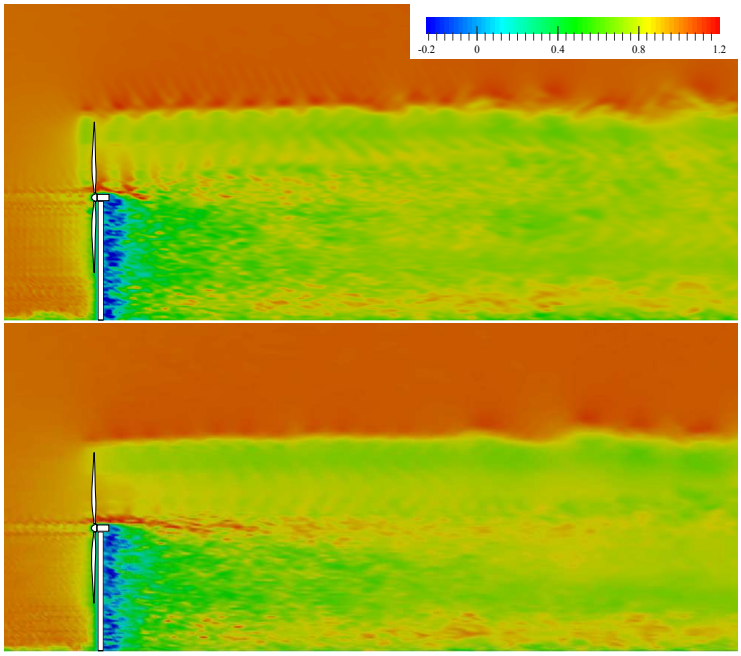

Figure 2.5: Instantaneous streamwise velocity in a vertical plane through the tower axis: ALM (top), RADM (bottom)

Chapter 3

Turbulent channel flow

3.1 Outline

The turbulent channel flow is one of the most studied case of turbulent motion. The simplicity of its geometry and nonetheless the possibility of studying some of the most essential features of turbulent flows are the major factors that had made it attractive for researchers, both in the experimental and in the numerical field.

One of the first examples of LES is actually the plane channel simulation by J.W. Deardoff in 1970[14].

The now classic Smagorinsky SGS model [79] was then used for the first time in a channel simulation, after having had considerable success in meteorological applications [80, 34]. Despite the very coarse mesh employed, with only 6720 grid points, fairly good results were obtained, thus showing the potentiality of the LES approach to the study of turbulent motion.

This early, pioneeristic work was then followed by a number successive studies which took advantage of the rapidly increasing computer capabilities and of the disposal of much sofisticated turbulent models.
Among the first to follow Deardoff's footsteps were the Karlsruhe group [77, 78, 27] and the Stanford group [55, 54].

By the end of the '80s Direct Numerical Simulations at moderately high Reynolds number, with the employment of very fine mesh able to guarantee accurate results, also became feasible.
Early examples are represented by the works of Kim *et al.*[37] and Spalart[84].

Although the essential dynamics and kinematics of the turbulence motions is far from being completely understood, however those works provided a clear description of the velocity and vorticity statistics

Even though some doubts were recently casted by Meyers & Sagaut [51] on whether the plane channel flow is the most appropriate case for assessing the performance of SGS models – due to its sensitivity to the computational grid arrangement –, it still represents the most common, and thus broadenly accepted, benchmark to evaluate the characteristics of various LES closure hypotheses.

3.2 Geometrical setup

In Figure 3.1 the geometry of the channel is shown as well as the reference system used.

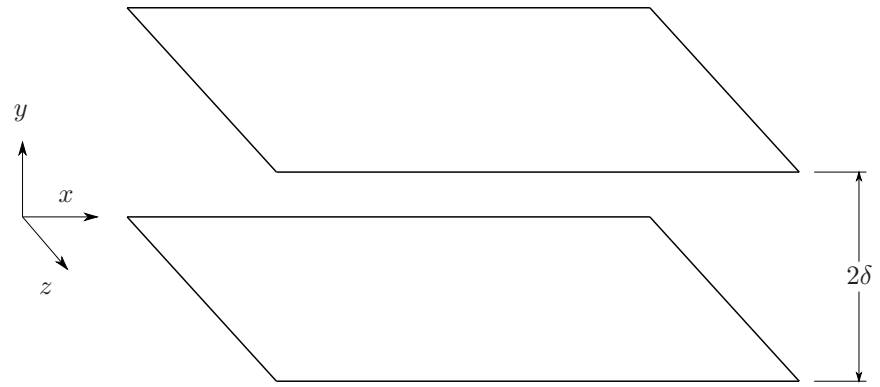

Figure 3.1: Geometry of the channel and reference system: x-direction is the streamwise direction

In both the spanwise and streamwise directions periodic boundary conditions are applied. Such a choice, which is widely employed in channel simulations, allows to adopt a smaller computational domain which greatly reduces the cost of the simulation.

The simulations of the channel flow were performed at a Reynolds number, based on the laminar inflow centre-line velocity U_c and the channel semi-height δ, of :

$$Re = \frac{U_c \delta}{\nu} = 10400$$

At this point it is worthwhile to introduce the concept of friction velocity (or, also, wall shear velocity) u_τ. It is defined as

$$u_\tau = \sqrt{\tau_w} \tag{3.1}$$

where τ_w is the shear at wall.

This leads to an alternative definition of the Reynolds number which is often used for the turbulent channel:

$$Re_\tau = \frac{u_\tau \delta}{\nu} \tag{3.2}$$

The shear at the wall can be computed equivalently in two differnt way. In fact, it can be obtained either from its definition as:

$$\tau_w = \frac{1}{Re} \left(\frac{\partial U}{\partial y} \right) \Bigg|_{y=0} \tag{3.3}$$

or from equilibrium considerations by noticing that for the balance of momentum in the streamwise direction the wall shear must compensate for the pressure gradient which drives the flow.

This relation can be directly derived from the Navier-Stokes equations, assuming that the flow is steady and fully-developed:

$$0 = -\frac{\partial \bar{p}}{\partial x} - \frac{d}{dy}(\overline{u'v'}) + \frac{1}{Re}\frac{d^2U}{dy^2} \tag{3.4a}$$

$$0 = -\frac{\partial \bar{p}}{\partial y} - \frac{d}{dy}(\overline{v'v'}) \tag{3.4b}$$

By taking the derivative along the x-direction of equation (3.4b) and recalling that the velocity is function of wall-normal coordinate only, it is straightly obtained that the streamwise pressure gradient $\partial\bar{p}/\partial x$ is independent of y coordinate.

Thus, integration along the y-direction of equation (3.4a) yields:

$$y\frac{\partial \bar{p}}{\partial x} = \frac{1}{Re}\frac{dU}{dy} - \overline{u'v'} + const. \tag{3.5}$$

The constant can be easily determined by observing that, for symmetry, at the channel semi-height($y = \delta$) both $\frac{dU}{dy} = 0$ and $\overline{u'v'} = 0$, hence $const. = \delta\frac{\partial \bar{p}}{\partial x}$. Then equation (3.5) can be re-written as follows:

$$\left(1 - \frac{y}{\delta}\right)\delta\frac{\partial \bar{p}}{\partial x} = \frac{1}{Re}\frac{dU}{dy} - \overline{u'v'} \tag{3.6}$$

By evaluating the equation (3.6) at the wall ($y = 0$), recalling equation (3.3) and that the Reynolds stresses vanish at the wall due to the non-slip conditions, it is finally obtained that:

$$\tau_w = \delta\frac{\partial \bar{p}}{\partial x} \tag{3.7}$$

This result provides an alternative way to compute the wall stress and the friction velocity.

Equation (3.7) could also have been obtained by application of the integral momentum balance equation to the whole domain.

For the present cases the Reynolds number Re_τ is nominally equal to $Re_\tau = 395$, while the actual value depends on the particular simulation. The turbulent database provided by the work of Kim *et al.*[57] is taken as reference in the present thesis for evaluating the results obtained.

The choice of the computational domain and the grid spacing is mainly influenced by the available computational resources, once the requirements on the minimum size for avoiding the periodic boundary conditions to spuriously affect the results have been accomplished.

Schumann[77] pointed out that artificialities due to these non-physical boundary conditions can be avoided if the domain is large enough for the two points correlations to be negligible for points separated by half the extension of the grid in each periodic direction. Comte-Bellot[12] reported typical distances (for the two point correlation to vanish) to be 1.6δ in the spanwise direction and 3.2δ in the streamwise direction.

The grid spacing should be small enough to capture all the significant scales of the flow in order to obtain trustworth results. Those requirements are dependent on the Reynolds number and they can become severely limiting for high values of Re. During the years the increase of computational power and the use of parallel computing has allowed to perform numerical simulations with higher Reynolds number.

Actually, Jiménez and Moin [32] has also shown that the domain has to be large enough to contain the all the flow structures, but the largest characteristc scales diminishes as the Re increases. Consequently the computational box may be smaller.

Considering the present Reynolds number and the fact that when dealing with a LES approach the constraint on the grid spacing can be relaxed because the SGS model is expected to provide the information which are lost by neglecting the smallest scales, the grid parameters shown in Table 3.1 were chosen.

axis	range	N_{pt}		Δ_{min}	Δ_{max}
x	$[0:2\pi]$	128		0.049	0.049
y	$[-1:1]$	128	uniform	0.016	0.016
			non-uniform	0.005	0.026
z	$[0:\pi]$	64	coarse	0.049	0.049
		128	fine	0.025	0.025

Table 3.1: Mesh details

The meshes employed are rather coarse with respect to those used in the reference work which, in the same computational box, constitute of $256 \times 193 \times 192$ grid points for streamwise, wall normal and spanwise direction respectively. Further comparisons with the reference data grid is provided in Table 3.2 which shows in detail the grid spacing in the three directions in terms of wall units.

Wall units are defined by adimensionalization of the physical coordinates with the friction velocity and the kinematic viscosity as follows:

$$x_i^+ = \frac{x_i u_\tau}{\nu} \qquad i = 1, 2, 3 \tag{3.8}$$

Δ^+_{axis}		*coarse*	*fine*	KMM
x		19.7	19.7	10.5
y	uniform	6.4	6.4	
	non-uniform (min)	2.0	2.0	0.03
	non-uniform (max)	10.4	10.4	6.5
z		19.7	9.8	6.5

Table 3.2: Grid spacings in terms of wall units Δx_i^+. KMM indicates the reference work by Kim, Moser and Mansour [57].

The non-uniform distribution of points along the wall-normal direction accumulates more points towards the walls of the channel to have a finer resolution in the area where the gradients are more severe and where the most complex and physically relevant phenomena of turbulence motions take place.

Points are distributed according to the following law:

$$y_j = \frac{\tanh \alpha \left(\frac{j-1}{N} - \frac{1}{2} \right)}{\tanh \frac{\alpha}{2}} \qquad j = 1, \ldots, N \tag{3.9}$$

where N is the total number of points in the y-direction.

The values of the ordinates as well as the evolution of the grid spacing along the wall-normal directions are shown in Figure 3.2.

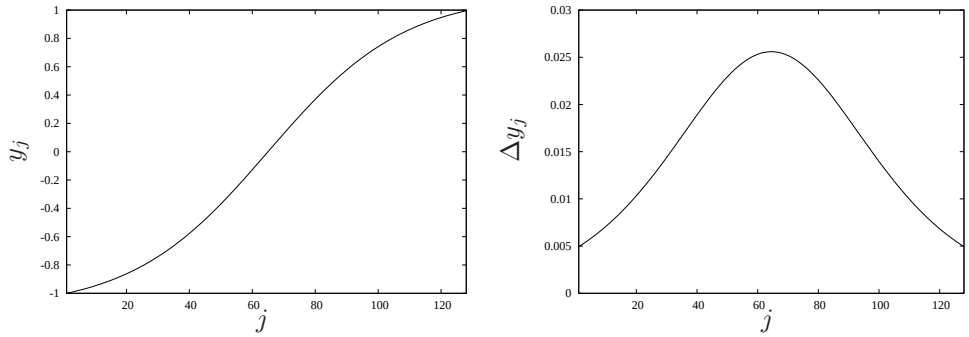

(a) Ordinate value (b) Grid spacing

Figure 3.2: Wall normal grid details

The grid distribution used by Kim *et al.* is different from (3.9). In fact, in view of the pseudo-spectral method which was employed for the discretization in the wall-normal direction, they adopted as grid-points the Chebychev nodes given by:

$$y_j = \cos\left(\pi \frac{2j-1}{2N} \right) \qquad j = 1, \ldots, N$$

Such a distribution, besides being well suited for the numerical method there employed, has also the feature of providing, given the number of point N, a major accumulation towards the ends of the interval then equation (3.9). Thus it allows to have very fine near-wall resolution, which is a primary requirements for an accurate Direct Numerical Simulations.

3.3 Results

Two no-model simulations were carried out on two different grids to evaluate the sensitivity of the results to the mesh employed in the computation. Further the various SGS models described in Sec. 2.3.2 have been tested on the finest of the two grids.

The models input parameters have been chosen according to respective authors' suggestions or, as was the case for the Smagorinsky model, according to usual values found in the literature. As for the Dynamic version of the

Smagorinsky, model the Germano-Lilly procedure [24, 46] has been adopted for the computation of the constant which has later been averaged in spanwise and streamwise directions for numerical stability purposes, i.e.:

$$C(y,t) = C_d(y,t)\bar{\Delta}^2 = -\frac{1}{2}\frac{\langle \mathscr{L}_{ij} M_{ij} \rangle}{\langle M_{ij} M_{ij} \rangle} \tag{3.10}$$

where $\langle \dots \rangle$ indicates the streamwise and spanwise average.

In Figure 3.3 is reported the time-averaged value assumed by $\sqrt{\overline{C_d}(y)}$ which can be compared with Smagorinsky model constant.

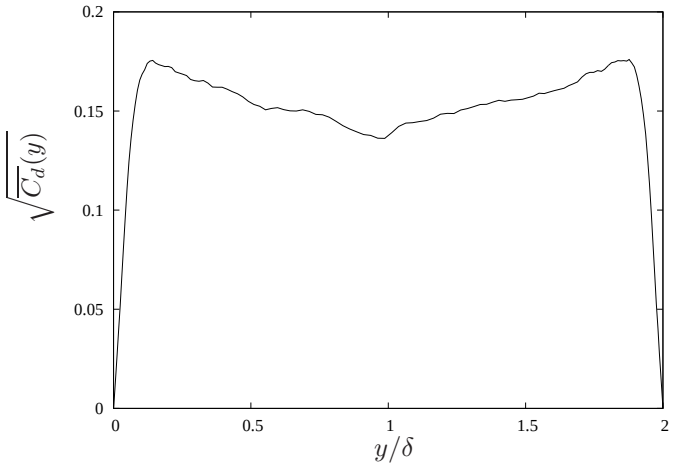

Figure 3.3: Time-averaged Dynamic Smagorinsky constant

Large-Eddy simulation parameters are reported in Table 3.3.

SGS model	constant
Smagorinsky	$C_s = 0.17$
σ-model	$C_\sigma = 1.35$
Vreman	$C_V = 2.5\, C_s^2$
WALE	$C_W = 0.5$

Table 3.3: LES models input parameters

The initial condition of the simulation is the laminar Poiseuille profile with super-imposed random perturbations of the order of the 15% of the mean centreline velocity. The governing equations were then integrated in time until a fully-developed turbulent flow was obtained. Such a state is identified by the value assumed by the pressure forcing, which is applied to the flow in order to keep a costant mass-flow rate.

The pressure gradient to keep a constant flow rate is computed by integrating over the whole domain the streamwise momentum equation:

$$\iiint_{\mathcal{V}} \left(\frac{\partial u_1}{\partial t} + \frac{\partial}{\partial x_j} u_1 u_j \right) \mathrm{d}\mathcal{V} = \iiint_{\mathcal{V}} \left(-\frac{\partial p}{\partial x_1} + \frac{1}{Re} \frac{\partial^2 u_1}{\partial x_j \partial x_j} \right) \mathrm{d}\mathcal{V} \tag{3.11}$$

where $\mathrm{d}\mathcal{V} = \mathrm{d}x_1\ \mathrm{d}x_2\ \mathrm{d}x_3$. It is easily verified that the second term on the left-hand-side vanishes because of periodic boundary conditions in x_1 and x_2 directions (terms $u_1 u_1$ and $u_1 u_3$) and because of the no-slip conditions in the wall normal direction (term $u_1 u_2$). The first term represents instead the variation of the total mass-flow rate. By posing:

$$Q = \iiint_{\mathcal{V}} u_1 \, \mathrm{d}\mathcal{V}$$

$$\Pi = -\frac{\partial p}{\partial x_1} = const.$$

equation (3.11) may be recast as follows:

$$\frac{\partial Q}{\partial t} = \Pi \cdot \mathcal{V} + \frac{1}{Re} \iiint_{\mathcal{V}} \frac{\partial^2 u_1}{\partial x_j \partial x_j} \, \mathrm{d}\mathcal{V} \tag{3.12}$$

For the mass-flow rate to be constant, then the pressure gradient must posed equal to:

$$\Pi = -\frac{1}{\mathcal{V}} \frac{1}{Re} \iiint_{\mathcal{V}} \frac{\partial^2 u_1}{\partial x_j \partial x_j} \, \mathrm{d}\mathcal{V} \tag{3.13}$$

For the laminar Poiseuille, as can be determined by equation (3.13), the pressure gradient assumes the typical value of $-\frac{2}{Re}$. As the flow becomes turbulent, the pressure gradient rises abruptly (in absolute value) since more energy is dissipated by the internal mechanisms of turbulence. When the flow reaches the fully-developed state, the the pressure gradient assumes a steady value, much higher than the starting one. A typical time hystory of the pressure gradient is shown in Figure 3.4.

All statistical quantities were computed considering only fully-developed velocity field. The mean of a generic quantity $q(x, y, z, t)$ is obtained by averaging in time and in spanwise and streamwise directions, which are the directions of homogeneity of the flow, and will be denoted by $\langle q \rangle$:

$$\langle q \rangle(y) = \frac{1}{T} \frac{1}{L_x \cdot L_z} \int_T \int_{L_x} \int_{L_z} q(x, y, z, t) \, \mathrm{d}x\ \mathrm{d}z\ \mathrm{d}t \tag{3.14}$$

The fluctuations from the mean value will be denoted by a prime, q':

$$q'(x, y, z, t) = q(x, y, z, t) - \langle q \rangle(y) \tag{3.15}$$

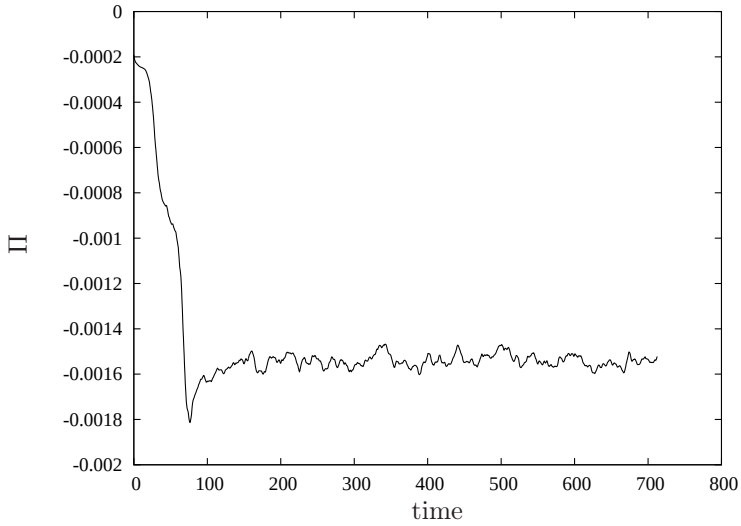

Figure 3.4: Pressure gradient time history

3.3.1 Mean velocity

One of the primary quantities of interest in the plane channel simulation is undoubtedly the mean streamwise velocity $U = \langle u \rangle$. An example of the typical fully-developed velocity profile is shown in Figure 3.5, together with the initial laminar Poiseuille profile.

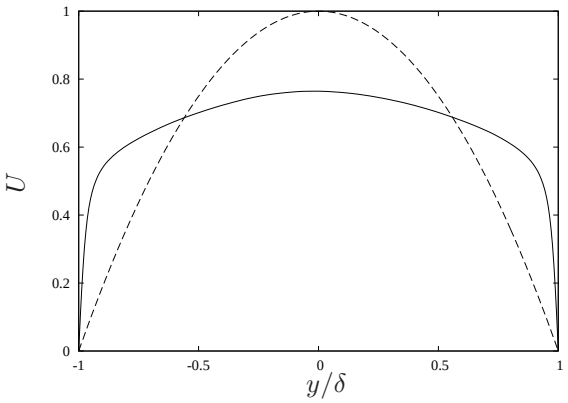

Figure 3.5: Mean velocity profile: (——) U, (- - - -) Poiseuille profile $u = 1 - y^2$

Turbulence enhances the mixing processes in the flow, including the exchange of momentum between fluid particles: this is clearly visible in Figure 3.5 as the central, high velocity region of the channel experiences additional drag due to the transport of low velocity fluid particles from the near-wall regions which, in turn are accelerated by high velocity fluid particle from the centre of the channel.

Such a mechanism is analogous to the *microscopic* mixing of molecules which occurs in laminar flows, but is much more efficient since in turbulent motion it concerns particles of fluid, i.e. it takes place at *macroscopic* level. This results in a velocity profile which is more flat in the central region of the channel and presents higher gradients near the wall, meaning that the skin friction would be higher too.

The behaviour of the velocity in the near wall region is a key feature for understanding the dynamic of wall-bounded turbulent flow and has been one of the principal subject of study since the introduction of the boundary layer concept in 1904 [68].

A major step forward was made in 1925 when Prandtl [69] postulated the existence of two zone within the turbulent boundary layer: the inner region, dominated by viscous effects, end the outer region (also called wake region) controlled by turbulence.

Following the path traced by Prandtl, von Kármán in 1930 [90] was able to derive, thanks to his similarity theory, a mathematical relationship for the velocity profile which is commonly referred to as the *log–law*:

$$u^+ = \frac{\langle u \rangle}{u_\tau} = \frac{1}{\kappa} \ln y^+ + A \tag{3.16}$$

where κ is the *von Kármán constant* and A is a constant which depends upon the type of flow. Both the constants are to be determined through eperimental measurements. Two common values reported in the literature [76, 65] are:

$$\kappa = 0.41 \qquad A = 5.5 \tag{3.17}$$

This law predict well the value of the velocity in the external parts of the inner region and the initial part of the wake region (in wall units, approximately $y^+ \geq 30$), which is therefore called the *logarithmic layer*.

In the immediate neighbourhood of the wall the flow is dominated by the laminar viscous shear and a linear relationship between velocity and distance from the wall may be extracted:

$$u^+ = y^+ \tag{3.18}$$

Equation (3.18) is accurate for $y^+ \leq 5$, i.e. in the so-called *viscous sublayer*. The transition zone between the two layers is often called *buffer layer* and it is described by empiric relationship which connects the two laws.

The velocity profiles obtained from the various simulations are reported in Figure 3.6, where a logarithmic grid is used for the distance from the wall in order to better reveal the variations of the velocity in the near wall layers. Comparison with reference data is also provided.

The results show overall good agreement with data despite the much coarser grid than KMM, especially in the immediate vicinity of the solid wall. As the central part of the channel is approached, accuracy generally decreases. This is partly due to the differences in the actual Re_τ of each simulation as well as to the coarsening of the mesh towards the centre of the channel.

However, this does not seem to be the case for the LES cases, where the SGS models prove to be effective at compensating for the poor grid resolution. The profiles obtained fit well also the theoretical results reported above, as it

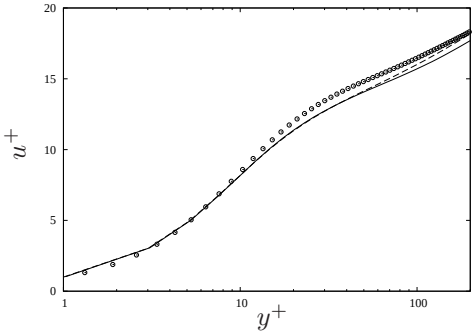

(a) No model simulations: fine grid (———), coarse grid (– – – –); KMM ∘

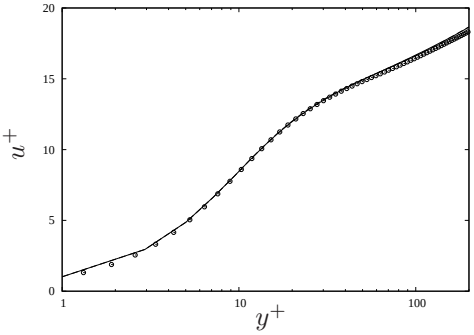

(b) LES: Dynamic model (———), constant Smagorinsky model (– – – –); KMM ∘

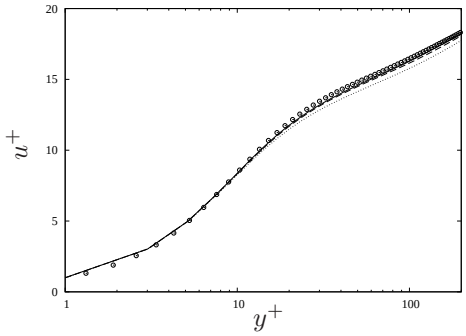

(c) LES: σ-model (———), Vreman (– – – –), WALE (·····); KMM ∘

Figure 3.6: Near-wall velocity profile

can be seen in Figure 3.7, where the data from the Dynamic model simulation are reported as an example: the agreement with reference data is excellent.

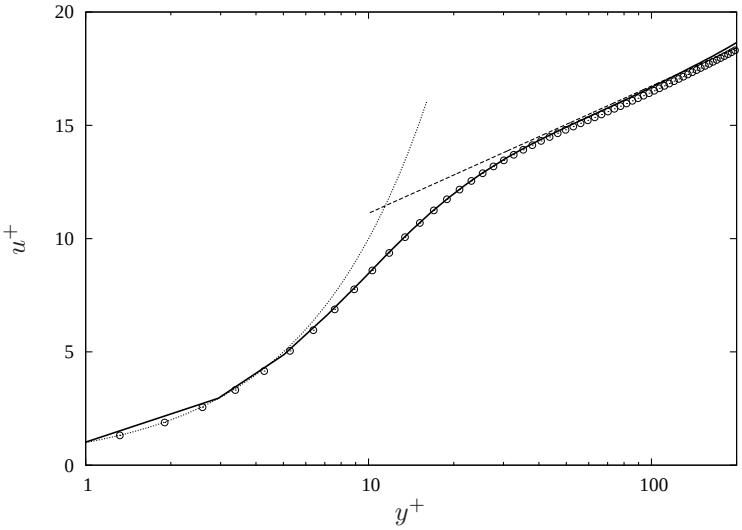

Figure 3.7: Near-wall mean velocity profile: ——— LES with Dynamic model, ∘ KMM. Theoretical results are also shown for the viscous sublayer, ····· eq. (3.18), and the log region, – – – – eq. (3.16)

3.3.2 Velocity fluctuations

The root mean square values of the velocity fluctuations, defined as $u_{rms} = \langle u'^2 \rangle^{\frac{1}{2}}$ (and analogously for the other components), normalized by the wall shear velocity are shown in Figure 3.8 -3.10 for half the channel height.

The results depend on the grid resolution, especially in the spanwise and wall normal components: this suggests that the coarse grid may not include all the relevant small-scale eddies responsible for the turbulent fluctuation. The streamwise component, instead, is nearly insensitive to the computional resolution, as was also the case for the computed average value.

The implementation of a SGS model has a moderate impact on the results, compared to the that of the mesh size, probably suggesting that the resolution employed may yet be enough fine to include most of the relevant scales. It may be interesting to notice that in some cases, as for the v_{rms} component with the Smagorinsky model, the implementation of a subgrid-scale model produces on the same grid produces a light worsening of the results, altough the general accordance remains satisfactory.

The shape of the velocity fluctuations is characteristic of the flow, with large amplitude concentrated in the near wall region where most of the turbulence is producted by the complex mechanisms taking place in the boundary layer.

At the center of the channel the amplitude decreases for all the components and approaches nearly the same value indicating that the nature of the turbulent eddies becames *quasi*-isotropic.

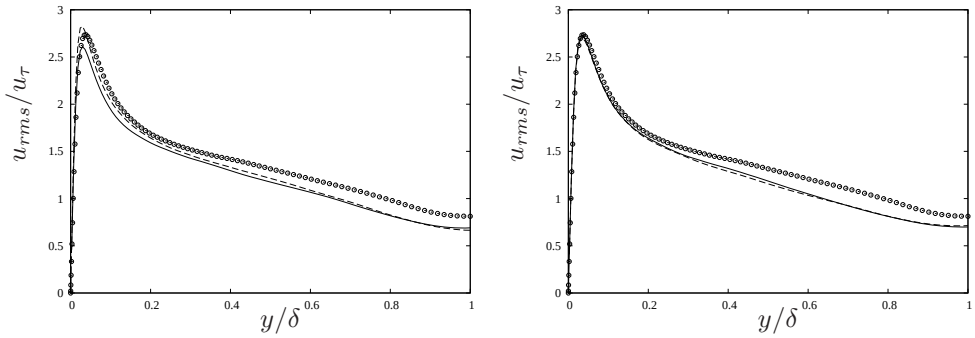

(a) No model simulation: fine grid (———), coarse grid (– – – –);KMM ∘

(b) LES: Dynamic model (———), Smagorinsky model (– – – –); KMM ∘

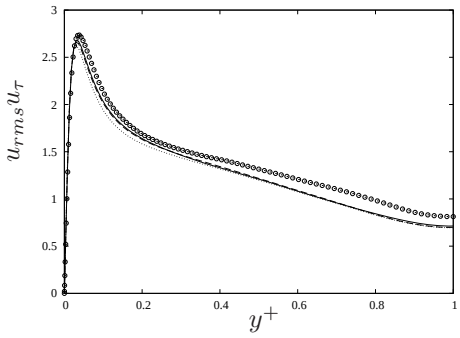

(c) LES: σ-model (———), Vreman (– – – –), WALE (·····); KMM ∘

Figure 3.8: Root mean square velocity fluctuations: streamwise component

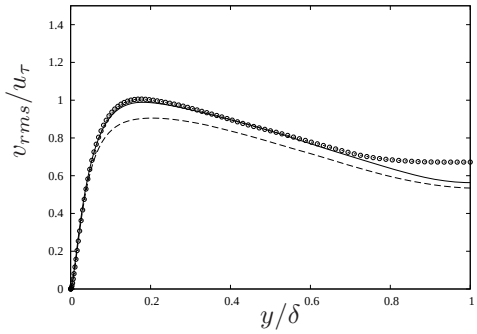

(a) No model simulation: fine grid (———), coarse grid (– – – –);KMM ∘

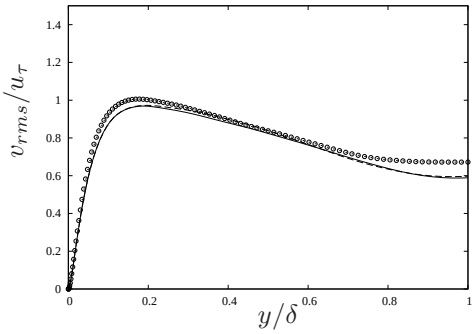

(b) LES: Dynamic model (———), Smagorinsky model (– – – –); KMM ∘

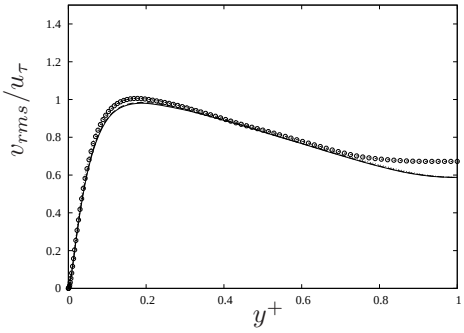

(c) LES: σ-model (———), Vreman (– – – –), WALE (·····); KMM ∘

Figure 3.9: Root mean square velocity fluctuations: wall-normal component

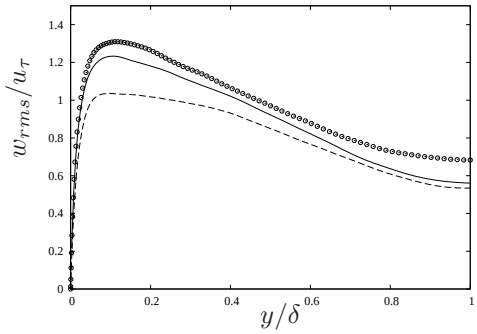

(a) No model simulation: fine grid (———), coarse grid (– – – –);KMM ∘

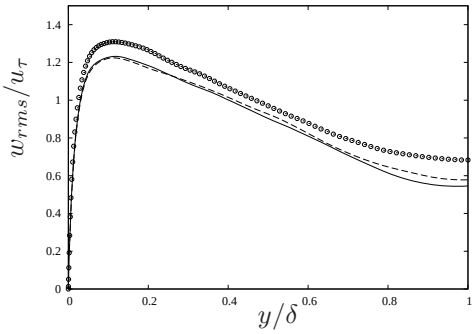

(b) LES: Dynamic model (———), Smagorinsky model (– – – –); KMM ∘

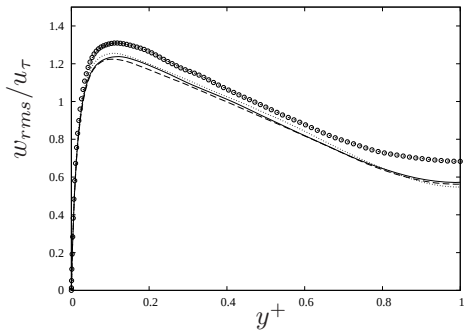

(c) LES: σ-model (———), Vreman (– – – –), WALE (·····); KMM ∘

Figure 3.10: Root mean square velocity fluctuations: spanwise component

3.3.3 Shear stress

The Reynolds stresses $-\langle u'v' \rangle$ are shown in Figure 3.11, where comparison with reference data is provided too.

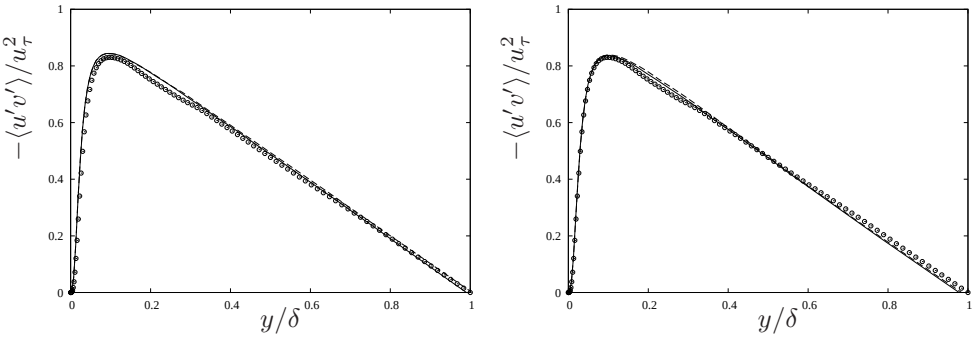

(a) No model simulations: fine grid (———), coarse grid (– – – –); KMM ∘

(b) LES simulations: Dynamic model (———), Smagorinsky model (– – – –), KMM ∘

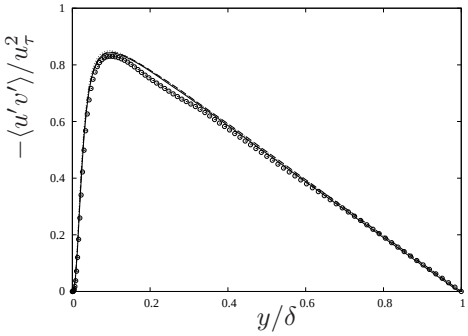

(c) LES: σ-model (———), Vreman (– – – –), WALE (·····); KMM ∘

Figure 3.11: Reynolds stresses $-\langle u'v' \rangle$

The total shear τ in the channel is given by the sum of the viscous stress and turbulent Reynolds stresses:

$$\tau = -\langle u'v' \rangle + \frac{1}{Re}\frac{dU}{dy} \tag{3.19}$$

The behaviour of the total shear with the distance from the wall can be determined from the streamwise momentum balance recalling equation (3.7). Upon integration in the y-direction, the following law for the total shear stress is derived:

$$\tau = \tau_w \left(1 - \frac{y}{\delta}\right) \tag{3.20}$$

Hence the total shear decreases linearly from his proper value at wall, τ_w, to the null value at the centre of the channel where both the viscous and Reynolds contribution are zero due to simmetry.

The linearity of the shear stress implies that the simulation has reached a fully developed state [37, 54].

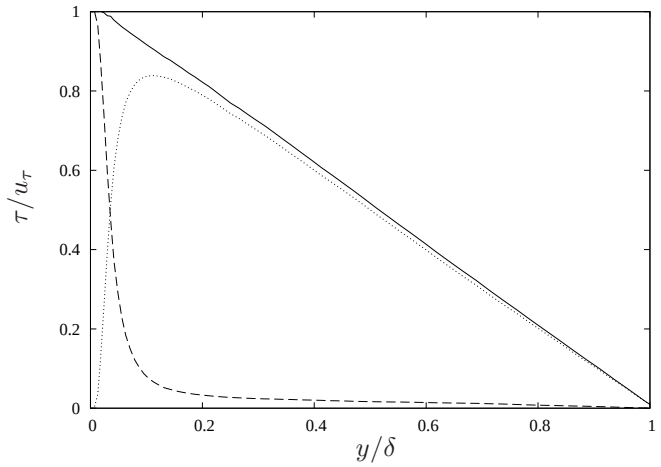

Figure 3.12: Shear stress balance: turbulent stress $-\langle u'v' \rangle$ (⋯⋯), viscous stress $\frac{1}{Re}\frac{dU}{dy}$ (- - - -),total (———).

With regards to Equation (3.19) it is possible to determine the contribution of the two component of the shear stress across the channel. As it shown in Figure 3.12 the viscous term is prevailing within a very short distance from the wall while departing from it the turbulent contribution becomes dominant and nearly accounts for the whole shear stress in the core of the channel.

This behaviour could have been easily predicted from the previous arguments. In fact, the mean profile shown in Figure 3.5 is characterised by a steep raise in the near wall region, thus yielding a high value of the wall-normal gradient and hence a high shear, and a *plateau* in the central zone.

One the other hand, the Reynolds stress can be expected to be maximum where the turbulence is most intense, i.e. in the *log region* of the turbulent boundary layer.

The behaviour in the near-wall region can be better appreciated by plotting the stress in wall units.

Figure 3.13 clearly shows as in the *viscous sublayer* the turbulent friction may be neglected compared to the shear due to the physical viscosity: this means that very near the wall the flow is essentially *laminar*.

Conversely, as the distance from the wall increases the flow is dominated by the turbulent structures which develops in the boundary layer and the turbulent stress becomes the most significant term in the total shear.

It is interesting to notice that the point where the viscous shear and the turbulent stress are equal coincides (nearly) with the point at which the turbulent production, $\mathcal{P} = -\langle u_i' u_j' \rangle \frac{\partial}{\partial x_j} \langle u_i \rangle$, reaches its maximum.

In fact, considering that – for the channel flow – one has $|S| = \sqrt{2 S_{ij} S_{ij}} =$

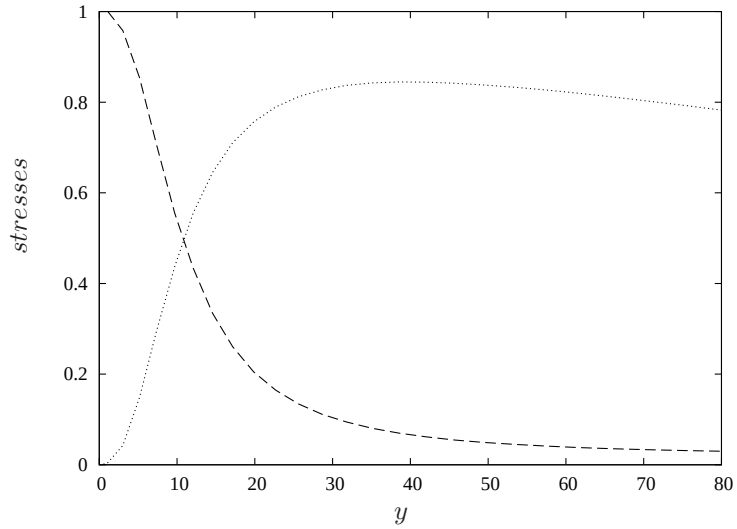

Figure 3.13: Near wall shear stresses: viscous stress (- - - -), turbulent stress (.....)

$\frac{dU}{dy}$, from equations (3.19) and (3.20) it is derived that:

$$-\langle u'v' \rangle = \tau_w \left(1 - \frac{y}{\delta}\right) - \frac{1}{Re}|S| \tag{3.21}$$

By multiplying each side with $|S|$, the profile of the turbulent production $\mathcal{P}$ is obtained:

$$\mathcal{P} = \tau_w \left(1 - \frac{y}{\delta}\right)|S| - \frac{1}{Re}|S|^2 \tag{3.22}$$

In the near-wall region, which is the zone under consideration, a dimensional analysis reveals that:

$$\frac{y}{\delta} = \frac{yu_\tau}{\nu}\frac{\nu}{u_\tau \delta} = y^+ \frac{1}{Re_\tau} \tag{3.23}$$

Hence, for a sufficiently high value of Re_τ, in the near-wall region (where $y^+ \backsim 1$) equation (3.22) may be re-written as:

$$\mathcal{P} = \tau_w|S| - \frac{1}{Re}|S|^2 \approx \tau|S| - \frac{1}{Re}|S|^2$$

By derivation along the wall-normal direction, it is possible to find the distance from the wall y_{max} at which the turbulent production attains a maximum:

$$\frac{1}{Re}|S|(y_{max}) = \frac{1}{2}\tau(y_{max}) \tag{3.24}$$

As a consequence it remains proved that – up to the order $\mathcal{O}(Re_\tau^{-1})$ – the Reynolds stresses are equal to the the viscous shear at the point where the turbulence production is maximum.

We notice that this point is nearly the same point at which the the streamwise velocity fluctuation reaches its maximum (see Figure 3.14) which shows, again,

the extremely intense turbulence activity which takes place in that zone of the channel.

3.3.4 Vorticity

In Figures 3.15 -3.17 it is shown the root mean square values of the vorticity fluctuations, $\langle \omega_i'^2 \rangle^{\frac{1}{2}}$, normalized by the kinematic viscosity and the friction velocity:

$$\omega_i^+ = \frac{\langle \omega_i'^2 \rangle^{\frac{1}{2}} \nu}{u_\tau^2}$$

The overall agreement with the reference result is good. The shape of the fluctuation is well captured by the simulation and minor discrepancies can be attributed to the rather coarse mesh.

Contrarily to the velocity fluctuations, the behaviour of each of the three components is very different in the near wall region and no similarity can be identified.

However, departing from the wall the three profiles tend to collapse in one curve, suggesting, as was the case for the velocity *rms* values, that the small scales of the, responsible for the vorticity fluctuations, tend to be isotropic.

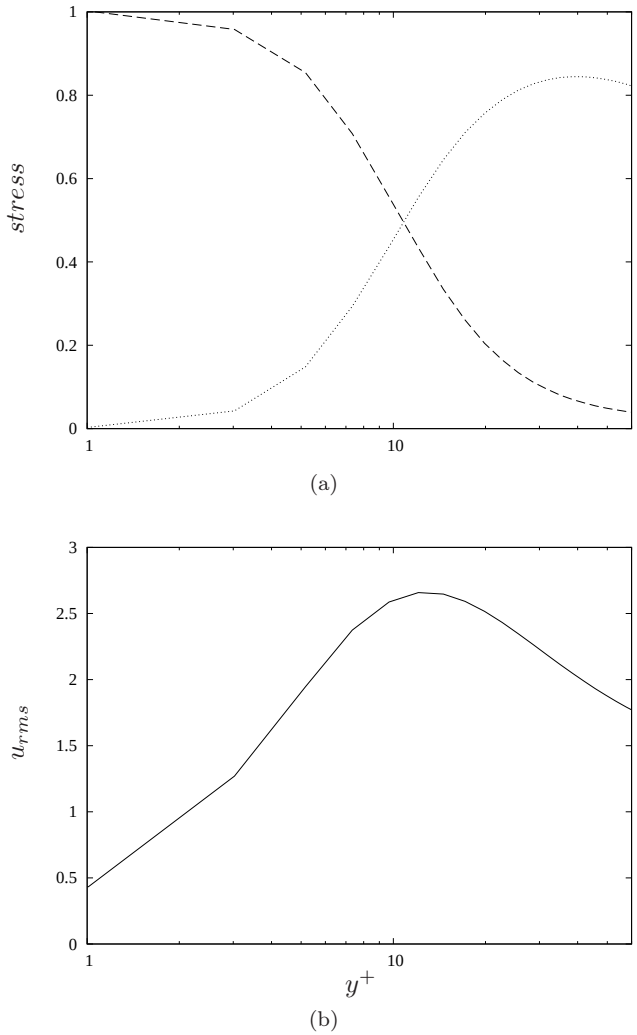

Figure 3.14: (a) Near wall shear stresses: viscous stress (- - - -), turbulent stress (·····); (b) Streamwise velocity fluctuation

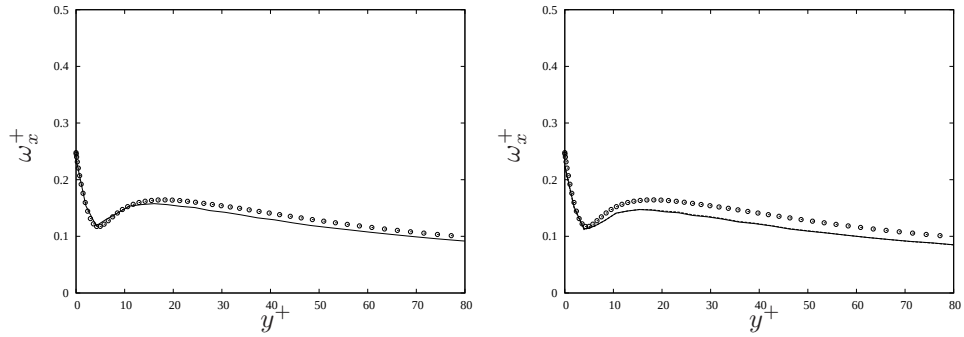

(a) No model simulations: fine grid (———), KMM ∘

(b) LES: Dynamic model (———), Smagorinsky model (– – – –), KMM ∘

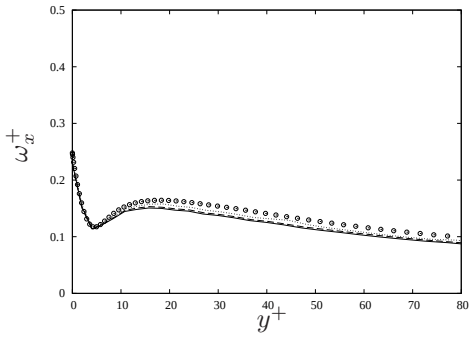

(c) LES: σ-model (———), Vreman (– – – –), WALE (·····); KMM ∘

Figure 3.15: Streamwise vorticity fluctuations

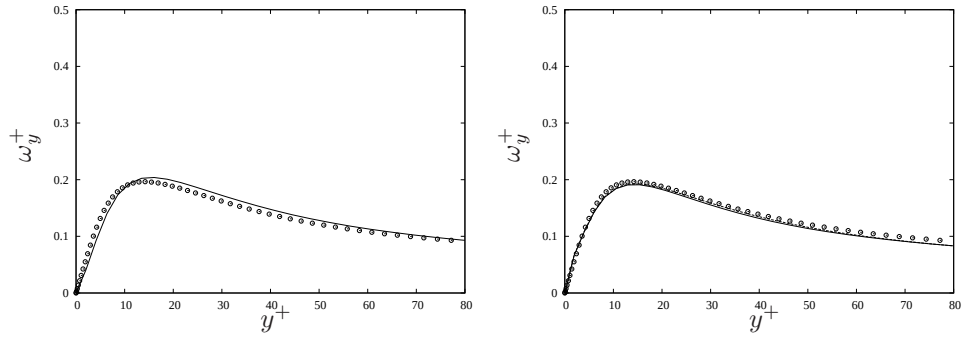

(a) No model simulations: fine grid (———), KMM ∘

(b) LES: Dynamic model (———), Smagorinsky model (- - - -), KMM ∘

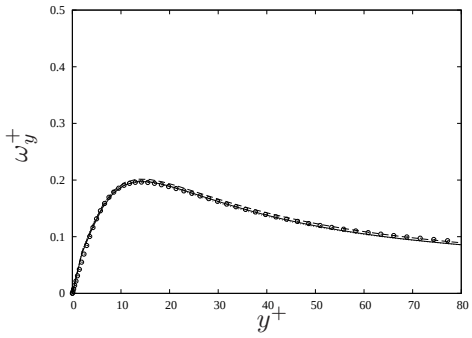

(c) LES: σ-model (———), Vreman (- - - -), WALE (·····); KMM ∘

Figure 3.16: Wall-normal vorticity fluctuations

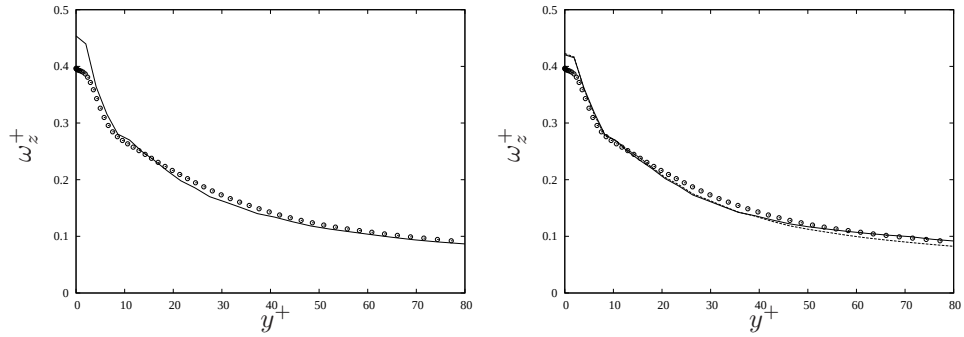

(a) No model simulations: fine grid (———), KMM ∘

(b) LES: Dynamic model (———), Smagorinsky model (- - - -), KMM ∘

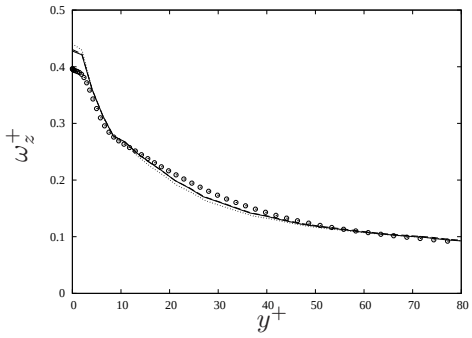

(c) LES: σ-model (———), Vreman (- - - -), WALE (·····); KMM ∘

Figure 3.17: Spanwise vorticity fluctuations

Chapter 4

Aerodynamics and Performances of Wind Turbines

In this chapter the numerical results obtained with the code described in Section 2.2 are presented and discussed. A brief outline of the anaylsis methods, other than the LES approch, historically used for the prediction of wind turbines and wind farms perfomances is first given. A description of the numerical setup follows and then the results of the computations are analysed with particular attention to advantages and disadvantadges which LES carries respect to the methods mentioned before.

The effect of the turbine parametrisation within the LES approach (Section 2.4) is also investigated as well as that of other parameters such as the Reynolds number and the operating conditions.

4.1 Simplified models

Historically a large interest has always been devoted to the analysis of rotating bladed disks immersed in a fluid stream because of the several practical applications which can be related to this generalized abstract scheme: besides wind turbines, ships and aircrafts propellers, helicopters rotors and windmills (which are the forerunners of modern wind turbines)

For this reason, long time before a numerical solution of the relevant governing equations was even foreseeable, analytical theories were developed. They were mainly focused in predicting those quantities which were of most immediate interest for practical use (rotor torque or rotor thrust, for instance) rather than in thoroughly describing the flow dynamics. Those theories are based on simplifying assumptions on the fluid and on the flow behaviour and are thus often referred to as simplified models.

Momentum Theory

The works of Rankine (1865, [70]), W. Froude (1878, [21]) and R.E. Froude (1889, [20]) led to the so-called *Momentum Theory*, which is the first and most simple description of wind turbine flow.

The theory assumes that the flow is:

i. incompressible

ii. inviscid

iii. non-rotating

iv. mono-dimensional

The rotor disk is modeled as an infinitely thin porous disk which applies a uniform force in the axial direction to the flow. An expression for the thrust force T applied by the disk might be determined by resorting to Bernoulli's theorem, which, due to hypothesis (i) and (ii), is equivalent to apply momentum conservation[8], and hence the name of the theory. By applying the Bernoulli's theoreme to the region upstream and downstream the rotor and further assuming that the wake is completely recovered and thus in equilibrium with the asymptotic pressure, $p_2 = p_\infty$ (see Fig 4.1 for notation):

$$T = \rho A u (U_\infty - u_w) \tag{4.1}$$

with:

$$\frac{1}{2}(U_\infty + u_w) = u \tag{4.2}$$

The velocity at the rotor u may be computed once the axial interference factor, or induction factor, a is known. This quantity is defined as:

$$a = 1 - \frac{u}{U_\infty} \tag{4.3}$$

The axial interference factor is related to the rotor operating conditions and it is possible to parametrise wind turbine performances as functions of a.

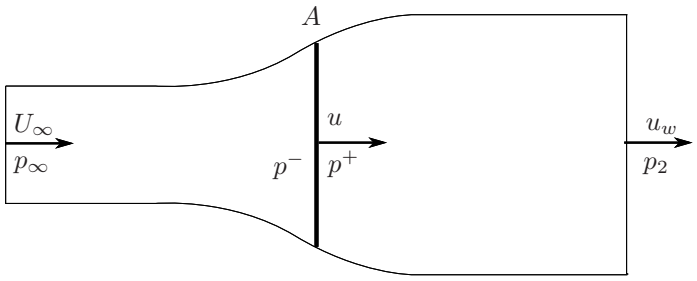

Figure 4.1: Momentum Theory: flow arrangement and notations

In fact, by application of the energy conservation principle it is possible to derive the relationship between the power extracted from the flow and the axial interference factor. In terms of the adimensional power coefficient C_P this expression reads as:

$$C_P = \frac{Power}{\frac{1}{2}\rho U_\infty^3 A} = \frac{Tu}{\frac{1}{2}\rho U_\infty^3 A} = 4a(1-a)^2 \tag{4.4}$$

By differentiation of expression (4.4) in a it is possible to derive the value of the induction factor which yields the maximum power extraction. This happens when $a = 1/3$ and the maximum power coefficient is found to be:

$$C_{P_{max}} = \frac{16}{27} \approx 0.59 \tag{4.5}$$

This $C_{P_{max}}$ constitutes an upper limit for the power extraction and is known as the Betz limit, after Albert Betz who first published its derivation in 1920 [6]. It is worthy to notice that this limit is not practically reacheable since all 'real' rotors induce a rotation in the flow which produces further momentum losses which are not taken into account by the Momentum Theory.

It is possible to derive an expression similar to Eq. (4.4) also for the thrust coefficient C_T:

$$C_T = \frac{T}{\frac{1}{2}\rho U_\infty^2 A} = 4a(1-a) \tag{4.6}$$

From Equations (4.4) and (4.6) it is possible to determine the *performance curves* of a wind turbine as it is shown in Figure 4.2.

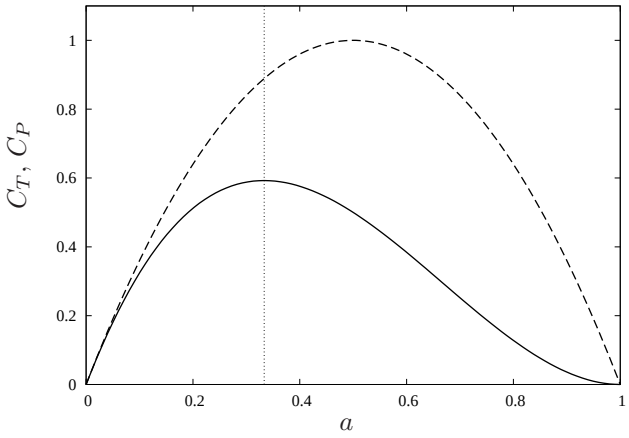

Figure 4.2: Wind turbine performance curves: C_T (- - - -), C_P (———). Optimal operating condition, $a = 1/3$, are also shown

An important remark has to be made regarding the curves shown in Figure 4.2 and the validity range of the Momentum Theory: in fact, from Eqs. (4.2) and (4.3) it derives that:

$$u_w = U_\infty(1-2a) \tag{4.7}$$

Thus it follows that if $a = 1/2$ then $u_w = 0$ which means that the streamlines which compose the streamtube that impinges the rotor cease to exist: this configuration is physically unacceptable and violates the underlying assumptions

of continuum mechanics [93, 85]. For $a > 1/2$ the velocity in the far wake would actually be negative according to Equation (4.7). What happens in reality is that particles from the surrounding high velocity region entrain in the wake due to turbulence. The velocity in the wake does not become negative, but the streamtube shown in Figure 4.1 does not exists anymore because of the entrainment. One should instead considers a larger area upstream to guarantee mass conservation. This would lead to a continous increase in the thrust force, contrarily of what it is shown in Fig. 4.2.

The Momentum Theory can not account for this mechanism since it assumes the flow to be one-dimensional and conservation of mass has to be respected within the streamtube which contains the rotor disk. Therefore it follows that the curves in Figure 4.2 are valid only for:

$$a < 1/2 \tag{4.8}$$

Blade Element Momentum Theory

The major drawback of the Momentum Theory lies in the fact that it is not possible to compute the axial interference factor. To overcome this problem, Glauert in 1926 [26] combined the results of the Momentum Theory with the Blade Element approach and developed the so-called Blade Element Moment (BEM) theory.

This theory is based on the same assumptions of the Momentum Theory, except for the fact that the rotation of the rotor is now taken into account and hypothesis (iii) is now dropped.

The rotor is divided into various annuli (see Fig 4.3) and independence between each annulus is assumed.

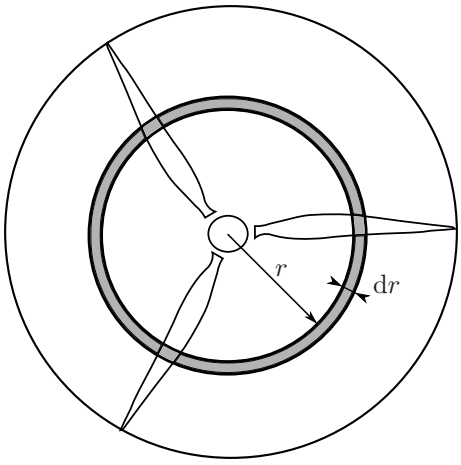

Figure 4.3: BEM Theory: rotor scheme

The blades are supposed to be rotating with angular velocity ω and to induce an azimuthal velocity in the flow given by:

$$u_\theta = \omega r a' \tag{4.9}$$

where a' is the tangential induction factor. The loading conditions under which the turbine blades are operating are computed resorting to the two-dimensional airfoil theory for each annulus the rotor is divided into. In fact, it is possible to determine the forces that each section of the blade produces, once the geometry and the performances (in terms of lift and drag coefficients) of the airfoil and the local flow conditions are known. As it shown in Figure 4.4, the lift and drag forces per unit length are given by:

$$F_L = \frac{1}{2}\rho V_{\text{rel}}^2 c\, C_L(\alpha) \tag{4.10}$$

$$F_D = \frac{1}{2}\rho V_{\text{rel}}^2 c\, C_D(\alpha) \tag{4.11}$$

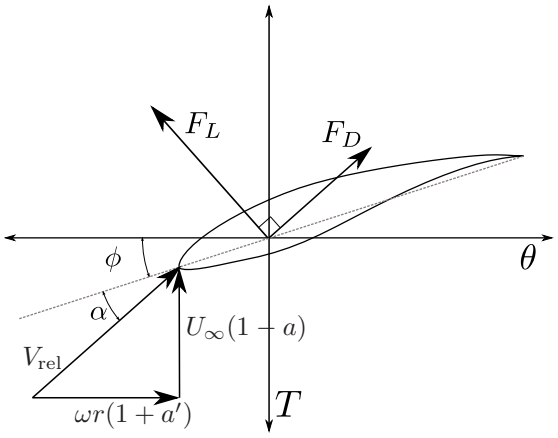

Figure 4.4: Blade section; T is the thrust direction, θ is the azimuthal direction

where c is the local airfoil chord, and C_L and C_D are the airfoil lift and drag coefficients respectively. The relative velocity impinging the blade leading edge depends on the interference that the rotor creates to the flow and can be expressed as a function of the induction factors:

$$V_{\text{rel}}^2 = U_\infty^2(1-a)^2 + \omega^2 r^2(1+a')^2 \tag{4.12}$$

Analogously the local angle of attack is given by:

$$\alpha = \arctan\left[\frac{\omega r(1+a')}{U_\infty(1-a)}\right] - \phi \tag{4.13}$$

where ϕ is the local twist angle of the blade section. By projecting the lift and drag forces onto the T–θ plane (see Figure 4.4) it is possible to derive the

expressions of the thrust and tangential forces (per unit length) which are more directly linked to the wind turbine performances:

$$F_T = N_b \frac{1}{2} \rho V_{\text{rel}}^2 c (C_L \cos\beta + C_D \sin\beta) \tag{4.14}$$

$$F_\theta = N_b \frac{1}{2} \rho V_{\text{rel}}^2 c (C_L \sin\beta - C_D \cos\beta) \tag{4.15}$$

where $\beta = \alpha + \phi$ and N_b is the number of the blades. We can express the local thrust force per unit length acting on annulus of area $\mathrm{d}A = 2\pi r \mathrm{d}r$ as:

$$F_T = \frac{1}{2} \rho U_\infty^2 \, \mathrm{d}A \, C_T^{\text{loc}} \tag{4.16}$$

We further assume that Momentum Theory equation (4.6) holds for the local thrust coeffient too: consequently Equation (4.16) assumes the form:

$$F_T = 4\pi r \rho U_\infty^2 (1-a) a \tag{4.17}$$

Analogously, the conservation of angular momentum yields an expression for the thrust force:

$$F_\theta = 4\pi r^3 \rho U_\infty \omega (1-a) a' \tag{4.18}$$

By comparing Eqs. (4.14)-(4.15) with Eqs. (4.17)-(4.18) it is derived that:

$$a = \left[\frac{4 \sin\beta}{\sigma \left(C_L \cos\beta + C_D \sin\beta \right)} + 1 \right]^{-1} \tag{4.19}$$

$$a' = \left[\frac{4 \sin\beta}{\sigma \left(C_L \sin\beta - C_D \cos\beta \right)} - 1 \right]^{-1} \tag{4.20}$$

where $\sigma = N_b c / 2\pi r$ is the solidity of the rotor. These last two equations fill the gap in the Momentum Theory which does not permit to compute the induction factor. With the help of Eqs. (4.19) and (4.20) it is now possible to implement an iterative procedure which allows the determination of a and a' and thus the knowledge of the loading conditions and the performances of an operating wind turbine. In fact, the thrust and power coefficient are now easily obtained by integration along the rotor radius of Eqs. (4.14) and (4.15):

$$Thrust = \frac{1}{2} \rho U_\infty^2 A \, C_T = \int_0^R F_T \, \mathrm{d}r \tag{4.21}$$

$$Power = \frac{1}{2} \rho U_\infty^3 A \, C_P = \int_0^R F_\theta \omega r \, \mathrm{d}r \tag{4.22}$$

The drawback of this approach is still represented by the limit in Eq. (4.8), which holds for the BEM theory too. To overcome this problem various authors

have proposed empirical corrections to account for the cases $a \geq 1/2$. Among others, Glauert itself derived a parabola fitted on data of highly loaded rotor helicopters [7] which reads as:

$$C_T = 0.889 - \frac{0.0203 - (a - 0.143)^2}{0.6427} \tag{4.23}$$

which is tangent to Eq. (4.6) in $a = 0.4$ for $C_T = 0.96$ (see Figure 4.5). It must be noted, however, that Glauert derived this relation for the thrust coefficient of the whole rotor (C_T). Nevertheless it has been applied locally, as C_T^{loc} in Eq. (4.14), in several BEM formulations [56].

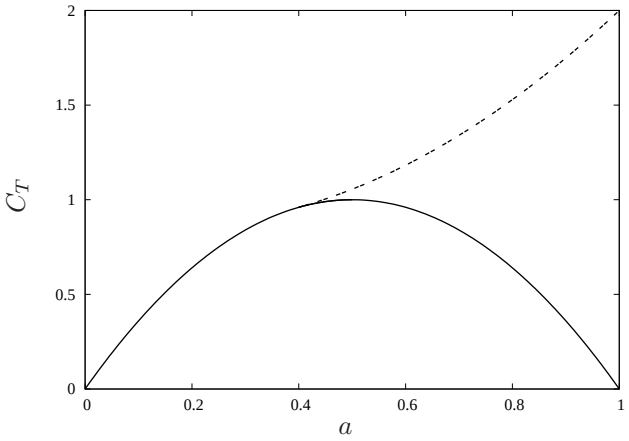

Figure 4.5: Thrust curve: (——) original BEM formulation, (- - - -) Glauert best-fit parabola

With this *ad hoc* correction, the BEM theory can be used to evaluate the performance of operating wind turbines once the geometry and the aerodynamics coefficients of the blade are known. Such results can be useful to make first-order assessments or comparisons with more refined – and computationally expensive – tools, such as LES.

A simple BEM code has been developed and some results are reported in Figure 4.6 for the reference 5-MW turbine designed at the National Renewable Energy Laboratory (NREL) [33]. Reference data were obtained with commercial code AeroDyn [56] which is based on a BEM formulation as well. The figure shows the power and thrust coefficients as function of the tip speed ratio $TSR = \omega R/U_\infty$ which is an important parameter which characterises the operating condition of the wind turbine and may be seen as analogous to the induction factor a.

Wake Models

Due to the increased demand for renewable energy, larger park with multiple rotors began to be designed (wind farm). This motivated researchers and engineers to look in deeper detail into wind turbine aerodynamics in order to characterise wake interactions in clustered configurations of wind turbines.

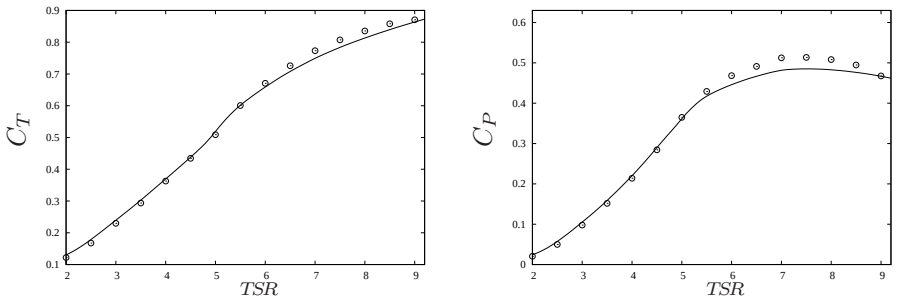

(a) Thrust coefficient: (———) NREL data, ∘ BEM code

(b) Power coefficient: (———) NREL data, ∘ BEM code

Figure 4.6: Performance curves of NREL 5-MW Turbine

The resulting models are often referred to as *wake models* since they aim at describing the effect of the rotor in the whole flow field and particularly the wakes of the turbines. They generally assume simplifying hypotheses, such as wake being self similar, axisymmetric or having a prescribed shape. Even though such assumptions may be not realistic and leading to inaccurate results [3], these models have a very low computational cost and can be run on a workstation in a few seconds and thus have represented a valuable tool for wind farm designers.

A notable example is the Jensen model [29], also known as Jensen-Park model, which has historically been the first model to be developed. It assumes the velocity deficit in the wake to be analogous to a negative jet. The wake behind the rotor expands linearly and has a uniform velocity which depends only on the distance from the rotor and on the constant κ which can be interpreted as a measure of the turbulence intensity and controls the wake expansion.

In the Jensen model, the wake is axisymmetric with diameter D_w and velocity u_w given by:

$$D_w = D(1 - 2\kappa s) \tag{4.24}$$

$$u_w = U_\infty \left[1 - \frac{1 - \sqrt{1 - C_T}}{(1 - 2\kappa s)^2}\right] \tag{4.25}$$

where $s = x/D$ is the adimensional streamwise distance from the rotor and C_T is the operating thrust coefficient which can be determined, for instance, through the BEM theory. In Figure 4.7 colour contours of the streamwise velocity at the hub plane are shown for a turbine operating with $C_T = 0.75$ and $\kappa = 0.075$ which is a typical value for on-shore wind turbines[3].

4.2 Large-Eddy Simulations

Differently from the techniques presented above, the LES approach does not assume any simplifying hypothesis but aims at giving a high fidelity description of flow field past a wind turbine. As consequence, a large number of information is obtained from a LES. The disadvantage is that substantial computational

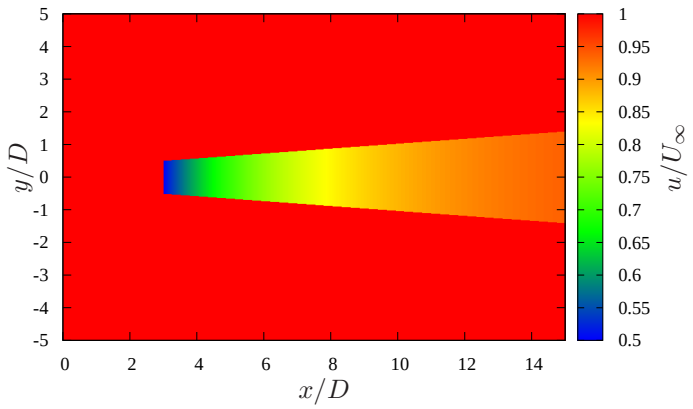

Figure 4.7: Streamwise velocity at hub plane. Rotor centre is at $(x/D = 3, y/D = 0)$, $C_T = 0.75$ and $\kappa = 0.075$

resources are required and hence the cost of a Large-Eddy Simulation is much higher than that connected to the models described above.

Nevertheless, the use of LES for the analysis of wind turbine flows may be justified in reason of the deep physical insight into the flow dynamics that they can provide because of the richness of the flow features which are considered.

4.2.1 Computational Setup

Simulations were performed for the NREL 5-MW reference turbine[33]: it is a three-bladed horizontal axis wind turbine (HAWT) with a rotor diameter $D = 126\,\mathrm{m}$, a hub height $h_{\mathrm{hub}} = 90\,\mathrm{m}$ and a design power production of $P_{\mathrm{des}} = 5\,\mathrm{MW}$, which are the typcal sizes of a modern utility-scale wind turbine.

The computational domain adopted for the simulations extends for $9D$ in the streamwise direction, $10D$ in the wall-normal (vertical) direction and $3D$ in the spanwise direction (as shown in Figure 4.8). The turbine is placed $3D$ from the inlet. The number of points used for the numerical evaluation is $512 \times 384 \times 256$ for the streamwise, wall-normal and spanwise direction respectively.

The grid is uniform in the streamwise and spanwise directions, direction x and z respectively, while it is stretched in the wall-normal direction (see Table 4.1 for details).

The stretching is designed such that the resolution is finer in the rotor area. This is required by the ALM since previous studies [48] have shown that 35 - 40 grid points are need to obtain accurate results. In Figure 4.9 details of the grid along the y-axis are shown.

Periodic boundary conditions are imposed on the lateral boundaries of the domain (spanwise direction): this mimics an infinite number of side-by-side turbines. The 'virtual' spacing, however, is large enough that lateral interaction

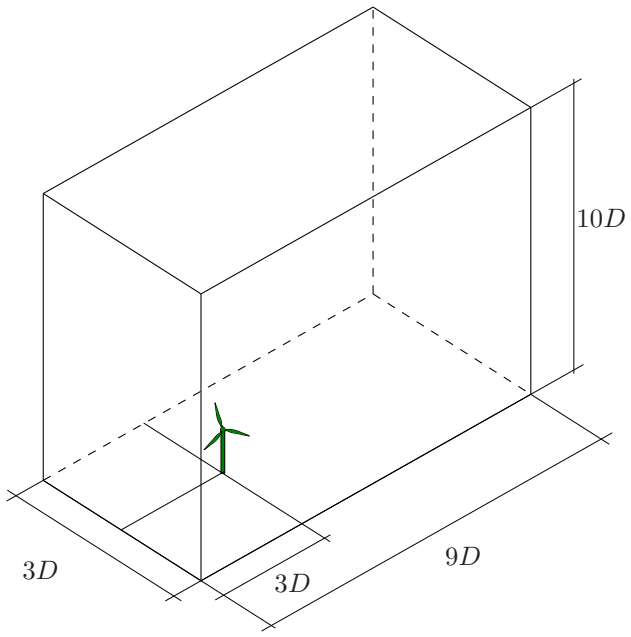

Figure 4.8: Computational domain

axis	range	N_{points}	$\Delta_{\min}/D$	$\Delta_{\max}$/D
x	$[0:9D]$	512	0.018	0.018
y	$[0:10D]$	384	0.014	0.042
z	$[0:3D]$	256	0.012	0.012

Table 4.1: Mesh details

is avoided.

On the lower boundary (ground) a no-slip condition is prescribed, on the upper a free-slip condition is applied. This boundary condition justifies the rather large height of the domain. Since the free-slip condition corresponds to imposing a straight streamline parallel to the ground at the boundary location, if the boundary is placed too close to the body (wind turbine), the flow would be over-constrained and unphysically high forces and velocities would be obtained from the numerical simulation. This effect is analogous to the *blockage effect* which is experienced in closed-wall wind tunnels.

At the inlet a uniform velocity U is prescribed as inflow profile. At the outlet a radiative boundary condition is imposed:

$$\frac{\partial u_i}{\partial t} - c\frac{\partial u_i}{\partial x_i} = 0 \tag{4.26}$$

(no summation over i is implied). The (adimensional) convection velocity is taken to be $c = 1$.

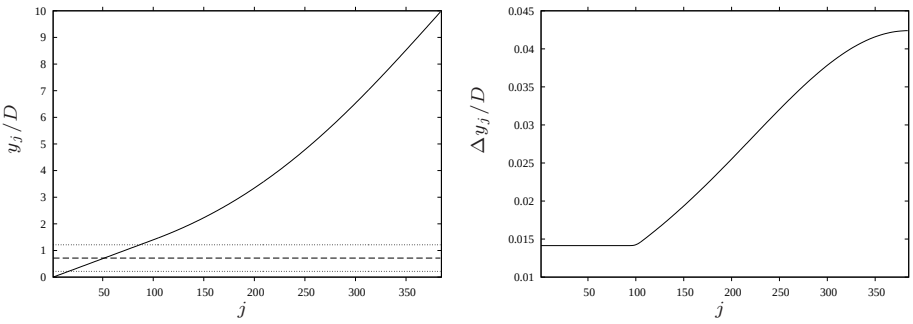

(a) Ordinate value: rotor centre (– – – –) and bottom e top blade tips (·····) are also shown.

(b) Grid spacing

Figure 4.9: Wall-normal grid details

The tower and the nacelle of the turbine are effectively modeled in the simulation through the Immersed Boundary Method (see Section 2.2). A no-slip condition is imposed on the surfaces of these bodies as well.

The rotor of the turbine has been modeled with both the Actuator Line Method and the Rotating Actuator Disk Method described in Section 2.4. A detailed comparison of the two methods is provided.

The effect of the Reynolds number has also been investigated: simulations have been carried at two different Reynolds numbers, namely $Re = 40\,000$ and $Re = 400\,000$. The Reynolds number is here defined as:

$$Re = \frac{UD}{\nu} \tag{4.27}$$

Considering the usual operating values of wind velocities, which ranges approximately from $3\,\mathrm{m\,s^{-1}}$ to $20\,\mathrm{m\,s^{-1}}$, and the typical dimensions it follows that the actual Reynolds number at which a modern wind turbine is likely to operate is $Re = \mathcal{O}(10^8)$. Such a Reynolds number is however beyond present capabilities even for a LES approach (see Section 2.3 for explanations). However results do not show a significant sensitivity to the Reynolds number for a value larger than 10^5 and the analysis may be justified even though the complete dynamic similarity is not satisified.

As for the SGS tensor, the classic Smagorinsky model has been employed. The model constant has been set to $C_s = 0.09$ after an *a priori* analysis was performed with the Dynamic model. The Dynamic model, Eq. (2.34), was applied to the results of a no-model simulation and the resulting tri-dimensional constant, Eq. (2.38), was averaged in time. Figure 4.10 shows the color contour of $C_s = \sqrt{\overline{C_d}}$ in a vertical plane containing the tower centreline.

In the present simulations the wind turbine is supposed to be working at a constant, selected *TSR*. The rotational speed ω is computed accordingly (Figure 4.11a). The power generated and the thrust applied by the turbine are computed on-line directly from the forces which the turbine applies to the flow (Figure 4.11b).

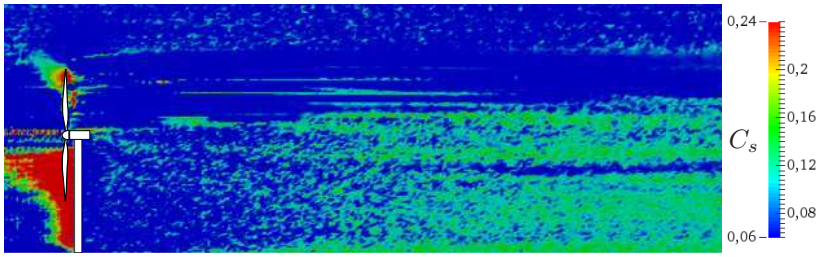

Figure 4.10: Time-averaged tridimensional Smagorinsky constant computed with the Dynamic model

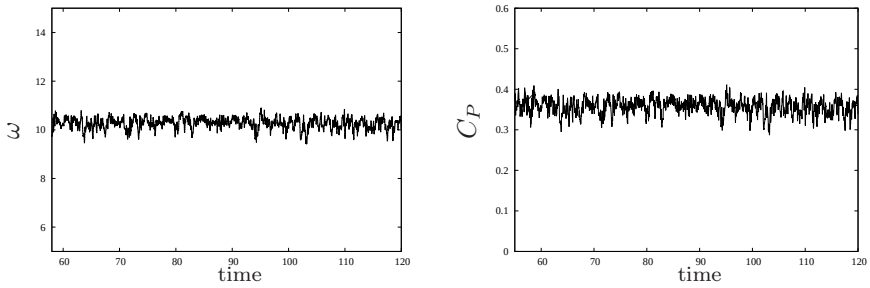

(a) Time history of rotor angular speed ω (b) Time history of power coefficient C_P

Figure 4.11: Code outputs, $TSR = 5.0 \quad Re = 400\,000$

Various tip speed ratios have been considered in order to cover a wide range of operating conditions.

4.2.2 Results

All the statistics have been computed by means of time average. Given a quantity $q(x, y, z, t)$, its time-average $\langle q \rangle(x, y, z)$ is computed as:

$$\langle q \rangle(x, y, z) = \frac{1}{T} \int_{t_0}^{t_0+T} q(x, y, z, t)\, \mathrm{d}t$$

where the initial time t_0 is chosen such that the turbine wake has fully developed in the domain (i.e. it has reached the outlet) and the sampling time T is large enough for the statistics to be converged.

The fluctuation of q is denoted by a prime and defined as:

$$q'(x, y, z, t) = q(x, y, z, t) - \langle q \rangle(x, y, z) \tag{4.28}$$

In Figure 4.12 the evolution of the time-average of the streamwise velocity averaged over the area swept by rotor is shown:

$$u_{\mathrm{rot}} = \frac{1}{A} \iint_A u\, \mathrm{d}A \tag{4.29}$$

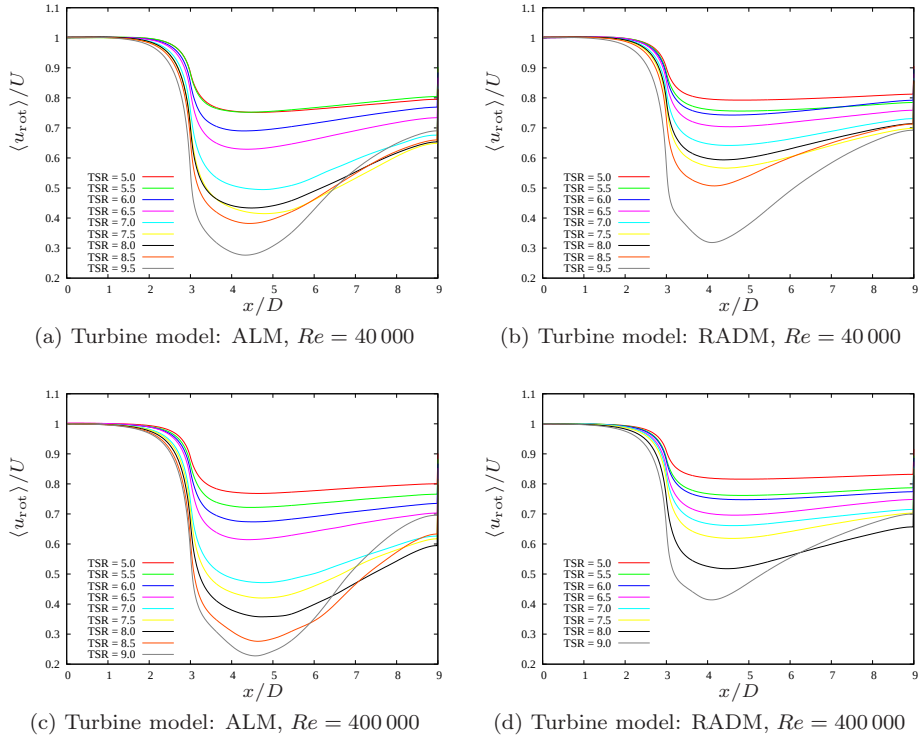

(a) Turbine model: ALM, $Re = 40\,000$

(b) Turbine model: RADM, $Re = 40\,000$

(c) Turbine model: ALM, $Re = 400\,000$

(d) Turbine model: RADM, $Re = 400\,000$

Figure 4.12: Rotor Averaged Velocity

This quantity may be helpful to draw comparisons with the simpler methods described above to evaluate wind turbine aerodynamics.

It is first noted that the rotor averaged velocity has a very steep gradient in proximity of the rotor position. This may cast some doubts over the choice of the induction factor, which can be computed as $a = 1 - \langle u_{\mathrm{rot}} \rangle / U$, as performance parameter. Indeed its evaluation involves a low accuracy procedure because of the high rate of change. On the contrary, the *TSR* appears a far more reliable variable to characterise the turbine operating status and is often employed in wind turbine controller.

The curves in Figure 4.12 also show that the wake recovery has a marked dependence upon the tip speed ratio. The slope of the curves downstream the turbine increases as the *TSR* increases. This is due to the fact that the turbulence level in the wake increases as well, because the swirling imparted by the rotating blades to the flow is enhanced. As a consequence the mixing between the wake and the surrounding high speed region is incremented and an *entrainment* of kinetic energy takes place in the wake.

This feature has very important consequences, especially when one considers aligned configurations of wind turbines. At a first analysis a high level of turbulence in the wake may appear as undesirable because of the fluctuating fatiguing loads which are experimented by the waked turbines. On the other hand a proper combination of longitudinal spacing and *TSR* may result in a

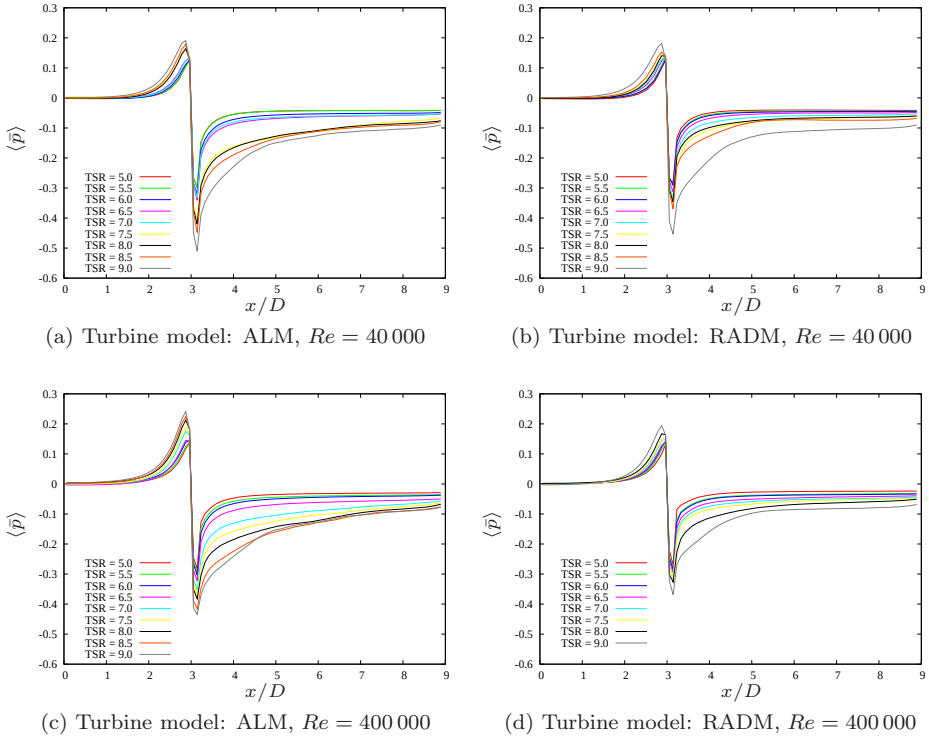

(a) Turbine model: ALM, $Re = 40\,000$

(b) Turbine model: RADM, $Re = 40\,000$

(c) Turbine model: ALM, $Re = 400\,000$

(d) Turbine model: RADM, $Re = 400\,000$

Figure 4.13: Time-Averaged pressure at hub height

faster wake recovery from the upstream turbine: in this way more energy in the wind would be available for the trailing turbine.

Simple wake models, such as the Jensen model, assume wake self-similarity respect to the *TSR*, which is not evident in Figure 4.12, hence do not capture this phenomenon. Other wake models have been developed with the aim of including the effect of the entrainment. However, they are based on a constant that has to be tuned with experimental measurements. LES, albeit at a higher computational cost, model the non linear effects in the wake and the entrainment without the need of *ad hoc* constants.

Finally, it can also be noted that the velocity 'drop' across the rotor disk is an increasing function of the *TSR*. This is related to the fact that the thrust coeffienct C_T is also a monotonic function of the *TSR* as shown in Figure 4.6a and this confirms the arguments which led to Equation (4.8).

In Figure 4.13 it is shown the behaviour of the time-averaged pressure at hub height $\langle \bar{p} \rangle (x, y_{hub}, z_{hub})$. At the outlet of the domain the pressure is still not fully recovered ($p|_{x/D=9} \neq p_\infty$): this was one the hypothesis underlying the BEM theory and thus casts some doubts over the use of such method for the evaluation of clustered configurations. In fact the typical spacing bewteen the turbines is around 5 - 7D. This is the so-called *far wake* region where to flow is expected to be influenced just indirectly from the upstream turbine. However,

as it appears from Figure 4.13, the wake not only is far from being recovered but also the effect of the *TSR* of the upstream turbine still is evident since the pressure deficit depends on it.

These arguments are supported by the flow visualisation reported in Figures 4.14–4.17. In Figures 4.14 and 4.15 color contours of time-averaged streamwise velocity at the hub height are shown. It can be observed that large regions downstream the turbine are characterised by rather low values of the velocity. The extent of this low velocity regions and the magnitude of the velocity deficit increase as the *TSR* increases. Clearly, this is due to larger thrust force which the turbine exerts on the flow.

In addition, in the so-called near wake region, i.e. within a 1-2D distance from the tower, the transversal expansion is qualitatively proportional to *TSR*. This contradicts the predictions of Jensen model which assumes the wake expansion to be dependent only on the coefficient κ representative of the incoming turbulence intensity, Eq. (4.24). This suggests that the wake self similarity hypothesis may be inappropriate.

Proceeding downstream, the behaviour is found to further deviate from the wake model assumption. As the *TSR* grows the wake region becomes thinner. The enhanced recovery for the high *TSR* cases is due to turbulence mixing which is promoted by rotational effects imparted by the blades. This effect was already observed when analysing the behaviour of the rotor averaged velocity as a function of the *TSR* (Figure 4.12).

It also emerges that the velocity in the wake is far from being uniform as assumed by the Jensen-Park model. Other commonly used Gaussian-like wake shapes also prove not to be very accurate especially in the proximity of the rotor due to the presence of tower and nacelle. The wake of the two bodies interacts with that of rotor blades. As shown in Figures 4.16-4.17 the presumed axisymmetry of the rotor wake is broken by the presence of tower and nacelle.

The importance of considering the effects of the tower and the nacelle when analysing wind turbine flows can be best appreciated from Figure 4.18. In this Figure color contours of the Turbulent Kinetic Energy (TKE) q are shown. The TKE is defined as:

$$q = \frac{1}{2}\left[\langle u'^2\rangle + \langle v'^2\rangle + \langle w'^2\rangle\right] \tag{4.30}$$

where $u'(x,y,z,t) = u(x,y,z,t) - \langle u\rangle(x,y,z)$ (and analogously for the other two components) is the streamwise velocity fluctuation. The TKE quantifies the kinetic energy contained in the turbulent eddies of the flow and is a measure of the local turbulence intensity.

It can be seen how most of energy is due to the wake of tower and nacelle. As it has been already stated above, turbulence motion has a significant impact on the wake characteristic and thus on the performances of the trailing turbines. As a consequence, since most of the turbulence production is due to the tower and nacelle, proper modeling of these bodies is required to obtain high-fidelity predictions of flow characteristics.

In Figure 4.18 it can be observed that, besides the tower, the region where the highest turbulence activity is observed is the blade tip. This could have

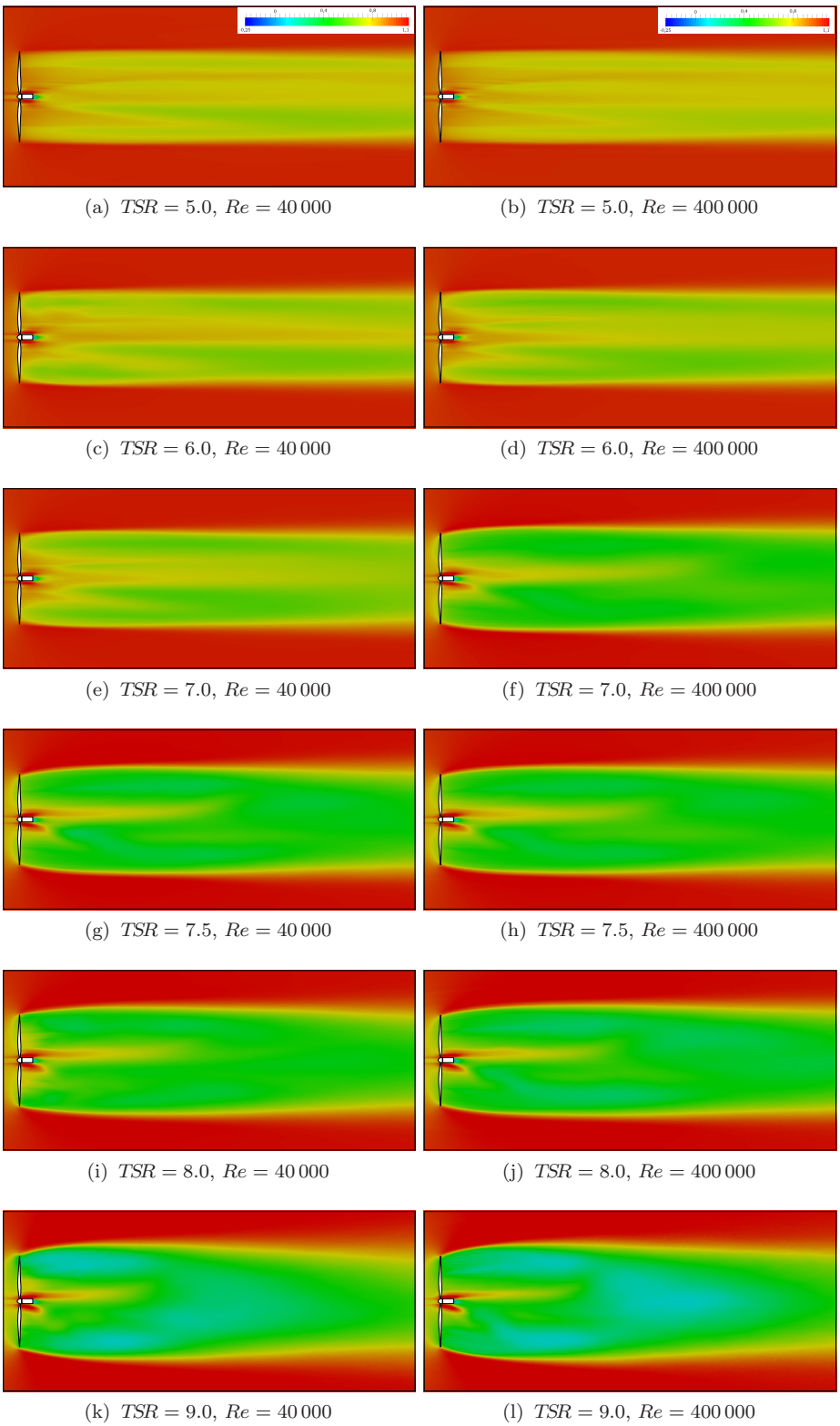

(a) $TSR = 5.0,\ Re = 40\,000$ (b) $TSR = 5.0,\ Re = 400\,000$

(c) $TSR = 6.0,\ Re = 40\,000$ (d) $TSR = 6.0,\ Re = 400\,000$

(e) $TSR = 7.0,\ Re = 40\,000$ (f) $TSR = 7.0,\ Re = 400\,000$

(g) $TSR = 7.5,\ Re = 40\,000$ (h) $TSR = 7.5,\ Re = 400\,000$

(i) $TSR = 8.0,\ Re = 40\,000$ (j) $TSR = 8.0,\ Re = 400\,000$

(k) $TSR = 9.0,\ Re = 40\,000$ (l) $TSR = 9.0,\ Re = 400\,000$

Figure 4.14: Color contours of time-averaged streamwise velocity at hub plane. Model: ALM

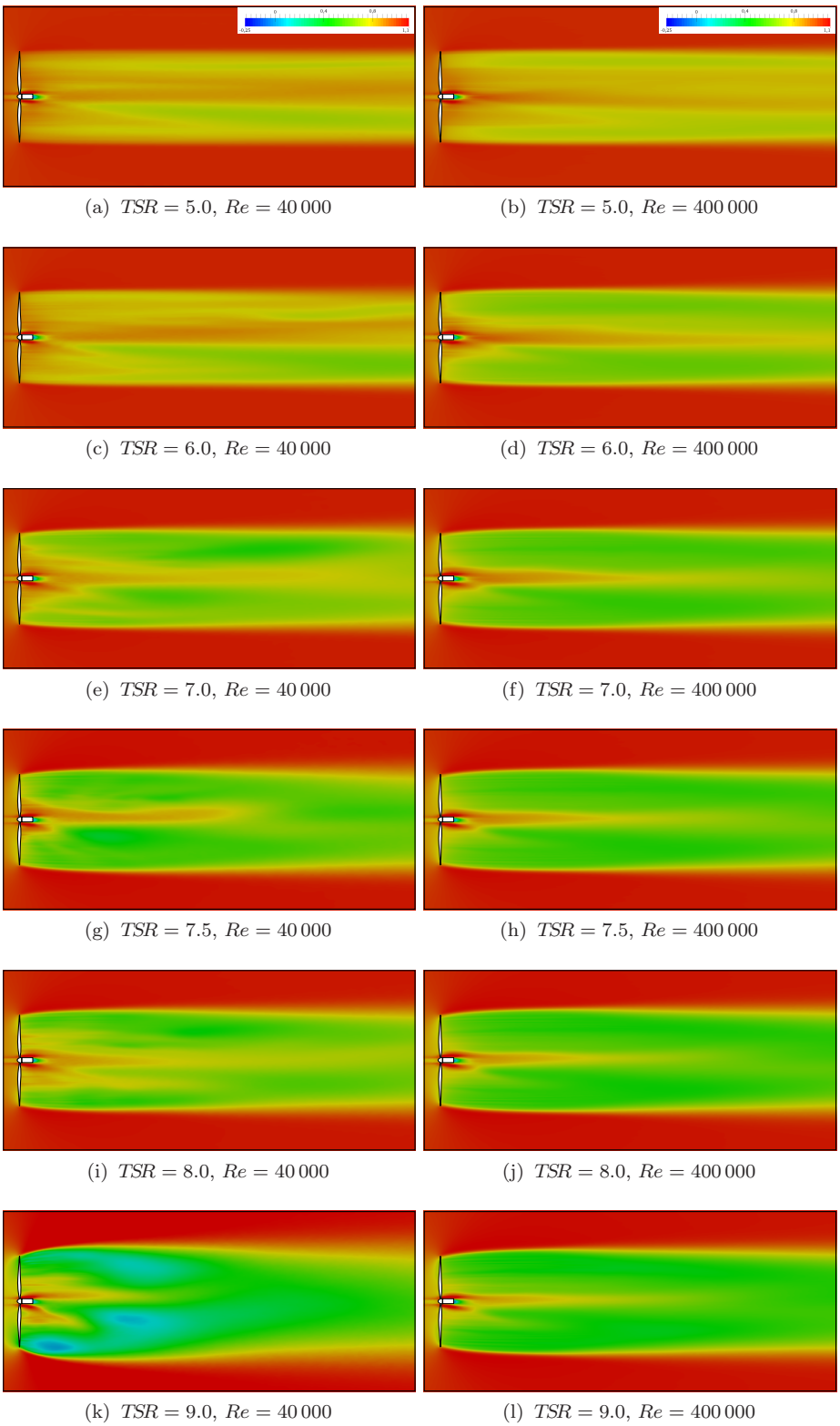

(a) $TSR = 5.0,\ Re = 40\,000$ (b) $TSR = 5.0,\ Re = 400\,000$

(c) $TSR = 6.0,\ Re = 40\,000$ (d) $TSR = 6.0,\ Re = 400\,000$

(e) $TSR = 7.0,\ Re = 40\,000$ (f) $TSR = 7.0,\ Re = 400\,000$

(g) $TSR = 7.5,\ Re = 40\,000$ (h) $TSR = 7.5,\ Re = 400\,000$

(i) $TSR = 8.0,\ Re = 40\,000$ (j) $TSR = 8.0,\ Re = 400\,000$

(k) $TSR = 9.0,\ Re = 40\,000$ (l) $TSR = 9.0,\ Re = 400\,000$

Figure 4.15: Color contours of time-averaged streamwise velocity at hub plane. Model: RADM

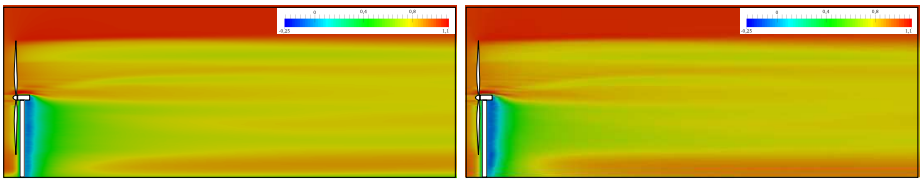

(a) $TSR = 5.0$, $Re = 40\,000$

(b) $TSR = 5.0$, $Re = 400\,000$

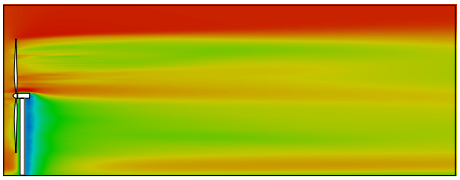

(c) $TSR = 6.0$, $Re = 40\,000$

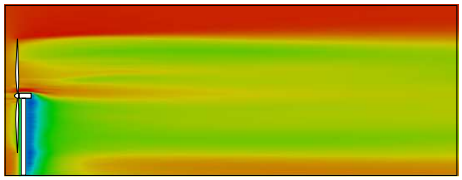

(d) $TSR = 6.0$, $Re = 400\,000$

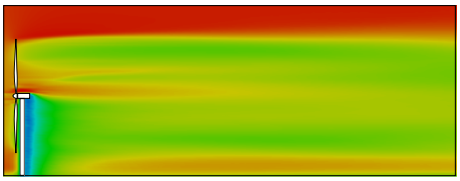

(e) $TSR = 7.0$, $Re = 40\,000$

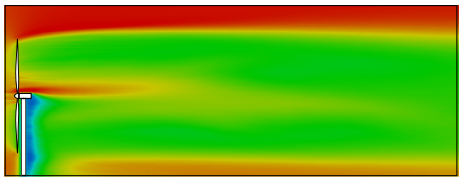

(f) $TSR = 7.0$, $Re = 400\,000$

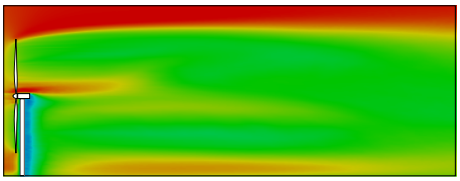

(g) $TSR = 7.5$, $Re = 40\,000$

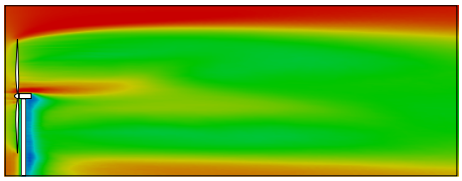

(h) $TSR = 7.5$, $Re = 400\,000$

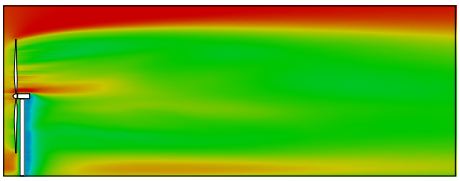

(i) $TSR = 8.0$, $Re = 40\,000$

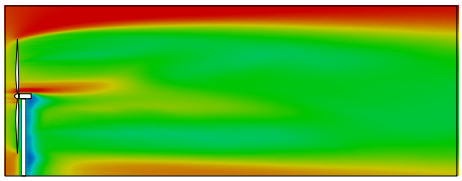

(j) $TSR = 8.0$, $Re = 400\,000$

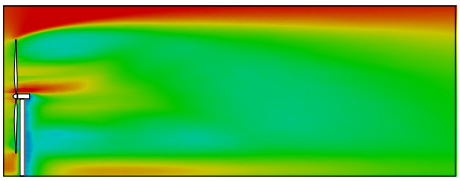

(k) $TSR = 9.0$, $Re = 40\,000$

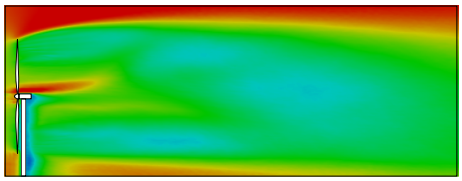

(l) $TSR = 9.0$, $Re = 400\,000$

Figure 4.16: Color contours of time-averaged streamwise velocity in the vertical plane passing for the tower axis. Model: ALM

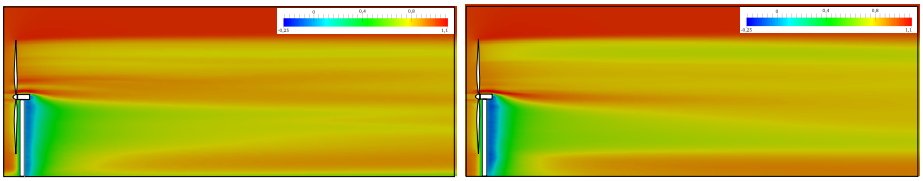

(a) $TSR = 5.0$, $Re = 40\,000$

(b) $TSR = 5.0$, $Re = 400\,000$

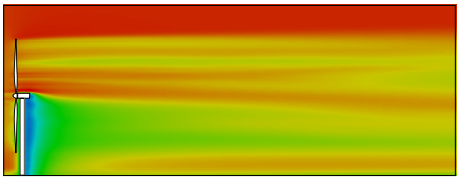

(c) $TSR = 6.0$, $Re = 40\,000$

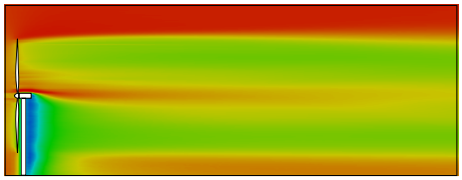

(d) $TSR = 6.0$, $Re = 400\,000$

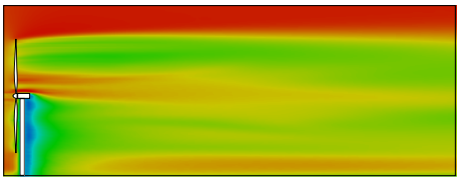

(e) $TSR = 7.0$, $Re = 40\,000$

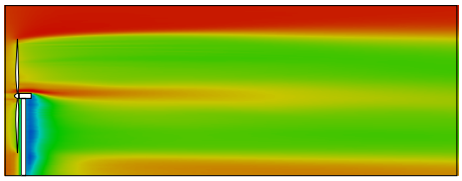

(f) $TSR = 7.0$, $Re = 400\,000$

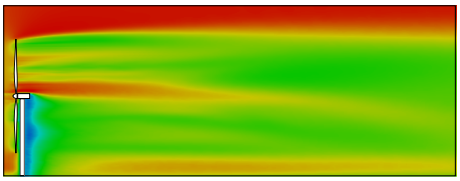

(g) $TSR = 7.5$, $Re = 40\,000$

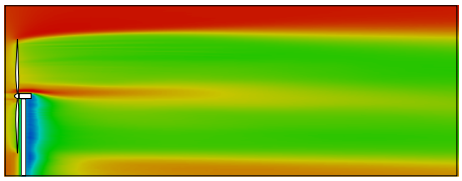

(h) $TSR = 7.5$, $Re = 400\,000$

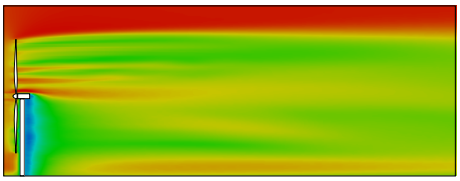

(i) $TSR = 8.0$, $Re = 40\,000$

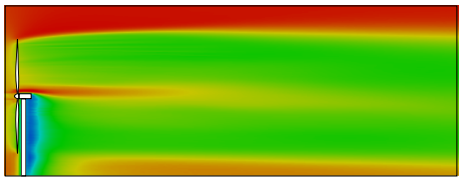

(j) $TSR = 8.0$, $Re = 400\,000$

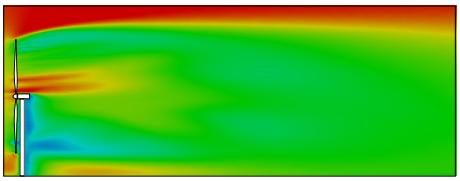

(k) $TSR = 9.0$, $Re = 40\,000$

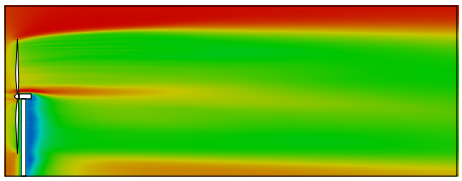

(l) $TSR = 9.0$, $Re = 400\,000$

Figure 4.17: Color contours of time-averaged streamwise velocity in the vertical plane passing for the tower axis. Model: RADM

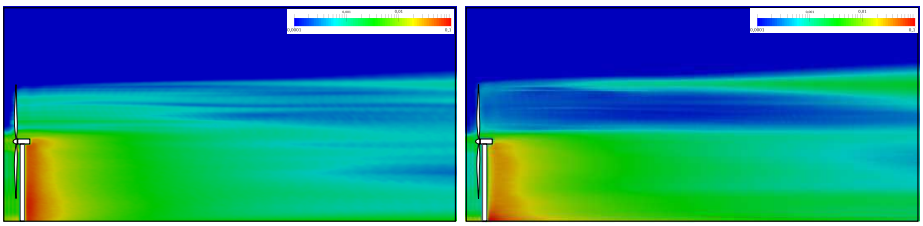

(a) $TSR = 5.0,\ Re = 40\,000$ (b) $TSR = 5.0,\ Re = 400\,000$

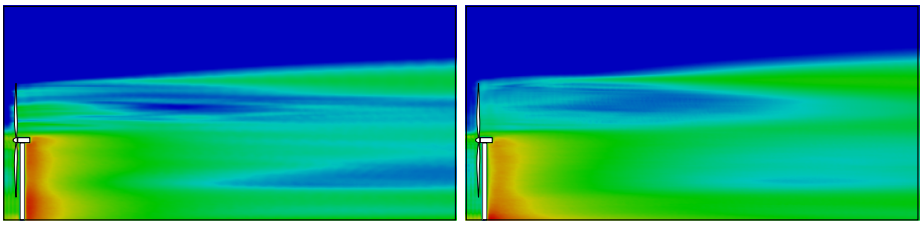

(c) $TSR = 6.0,\ Re = 40\,000$ (d) $TSR = 6.0,\ Re = 400\,000$

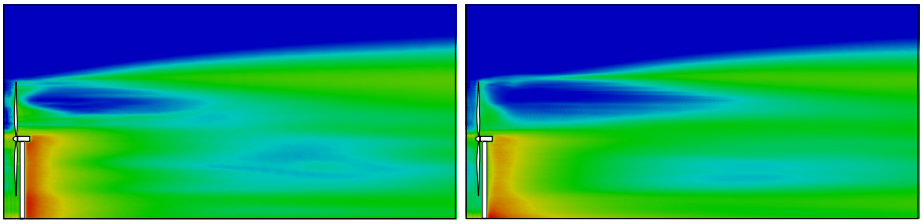

(e) $TSR = 7.0,\ Re = 40\,000$ (f) $TSR = 7.0,\ Re = 400\,000$

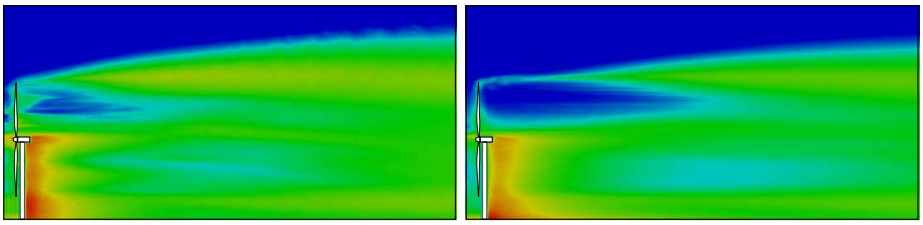

(g) $TSR = 7.5,\ Re = 40\,000$ (h) $TSR = 7.5,\ Re = 400\,000$

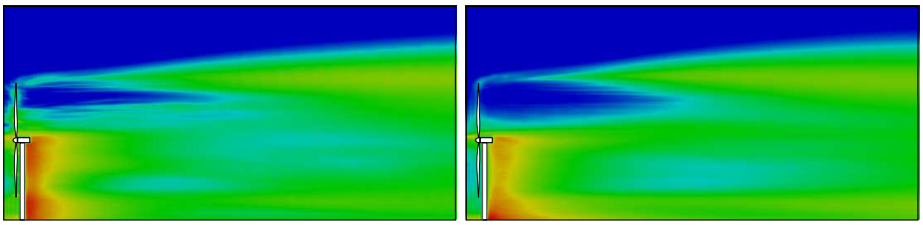

(i) $TSR = 8.0,\ Re = 40\,000$ (j) $TSR = 8.0,\ Re = 400\,000$

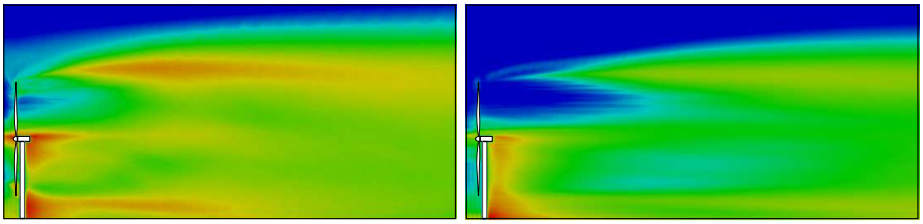

(k) $TSR = 9.0,\ Re = 40\,000$ (l) $TSR = 9.0,\ Re = 400\,000$

Figure 4.18: Color contours (logarithmic scale) of TKE in the vertical plane passing for the tower axis. Model: RADM.

been expected from the high shear observed in that region in Figures 4.14-4.17. The peak of the TKE occurs after the near wake region. As the *TSR* increases, it grows in intensity and moves closer to the turbine. This is in accordance with changes of slope and the different recovery observed in Figure 4.12. For the high *TSR* conditions the entrainment of kinetic energy from the high speed region above the top tip height, promoted by the turbulent activity, is greater in intensity and in axial extent: hence the faster wake recovery.

From a physical point of view the different turbulent activity, depending on the operating *TSR*, in different regions of the wake also coincides with a change in the structures of the wake. In the near wake region the turbulent, diffusive phenomena are overcome by the convective mechanisms which are characterised by smaller time scales. This implies that the large scale structures which originates from the bound vorticity on the blades surface are transported downstream quite coherently. The wake is characterized by the helicoidal path which is followed by the tip vortex departing from the blade tip and by the trailing vorticity which originates from the blade trailing edge.

As the wake moves downstream and the turbulent mixing increases, the large coherent structures are progressively dissipated into smaller ones with the typical mechanisms of the energy cascade. The so-called *vortex breakdown* occurs and the wake is no longer helicoidal but fully turbulent and characterised by small chaotic eddies.

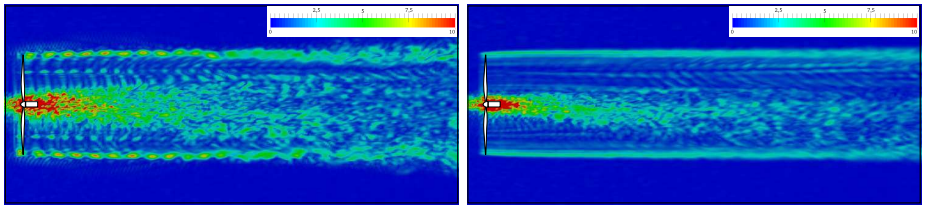

(a) $TSR = 5.0$, model: ALM (b) $TSR = 5.0$, model: RADM

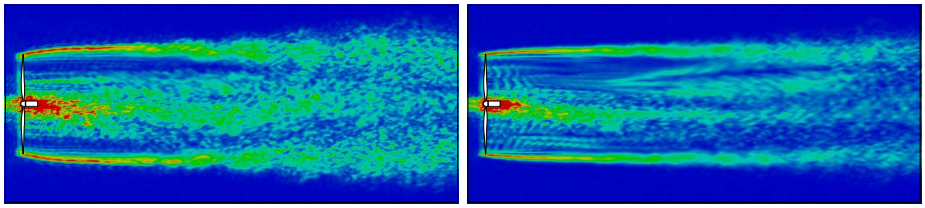

(c) $TSR = 7.0$, model: ALM (d) $TSR = 7.0$, model: RADM

Figure 4.19: Color contours of vorticity magnitude at hub plane, $Re = 40\,000$

The behaviour described above is particular evident in Figure 4.19a, where contours of the vorticity magnitude are shown. Each individual tip vortex, corresponding to the passage of a blade, is clearly visibly as well as the pattern of the blade rotation. The *TSR* is relatively low and the vortices are convected downstream coherently until the breakdown occurs.

As the *TSR* increases, Fig. 4.19c, the rotational velocity of the blades increases and the frequency with which a blade passes through increases. This results in an increment in the frequency with which the tip vortices are released

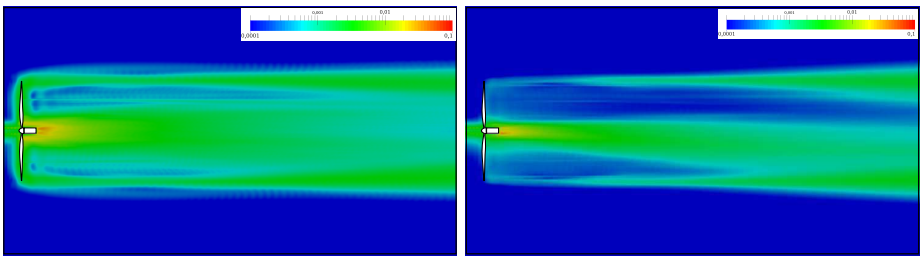

(a) $TSR = 5.0$, model ALM

(b) $TSR = 5.0$, model RADM

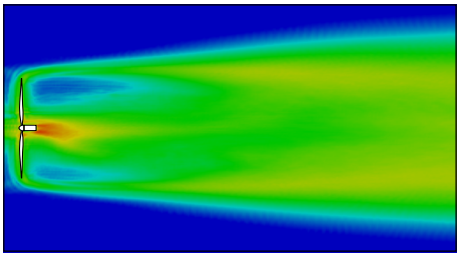

(c) $TSR = 7.5$, model: ALM

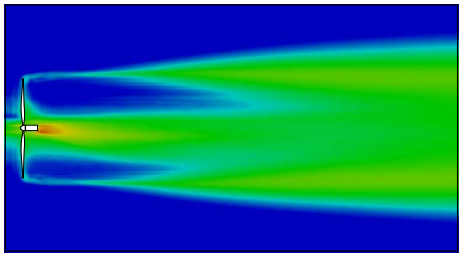

(d) $TSR = 7.5$, model: RADM

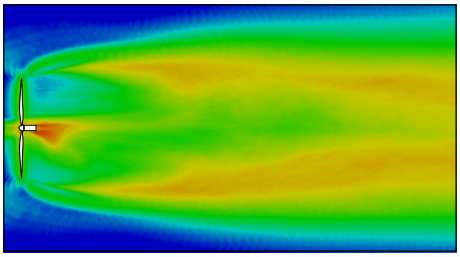

(e) $TSR = 9.0$, model: ALM

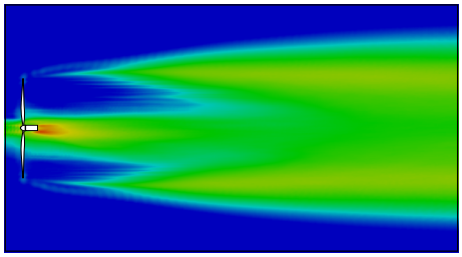

(f) $TSR = 9.0$, model: RADM

Figure 4.20: Color contour of TKE at hub plane, $Re = 400\,000$

and thus they are much closer one to each other such that they can merge together. The turbulence in the wake is increased to and the breakdown occurs earlier (more upstream).

From Figure 4.19 it is also possible to appraise the differences between the models employed for the turbine rotor. As expected, the ALM provide a more detailed characterisation of the field structure. The RADM does not capture distinctly the tip vortices since the local effect of the blade tip is obviously lost because of the larger force spreading. However, it is still possible to recognize the pattern of the rotation of the disk, which represents an improvement with respect to the traditional Actuator Disk.

It is interesting to notice that the RADM yields a field which is globally smoother. As can be seen in Figure 4.19, the smallest scales structures present in the ALM field are 'filtered' out by the RADM. This aspect can be observed also in Figure 4.20 by comparing the Turbulent Kinetic Energy field. Although both models show the trends and features discussed above, the turbulence intensity of the RADM field is generally lower than that of the ALM.

The reason for this behaviour may be indentified exactly in the fact that the RADM does not describe all the detailed dynamics which occurs in the wake. It is thus evident that these small scales affect significantly vorticity and TKE, while on the other hand the average velocity (Figures 4.16-4.15) is less sensitive. The overall agreement between the two models is good and the loss in accuracy connected with the use of the RADM instead of the ALM is partially compensated by the much lower computational cost.

Regarding the Reynolds number dependence, as already anticipated, the results do not show a significant sensitivity to this parameter, with only the TKE showing a weak dependence (this fact could have easily been expected since the TKE is a measure of the turbulence intensity which is closely related to the Reynolds number). Therefore numerical simulations can be performed at a lower Reynolds number than 10^8 and still having meaningful results. On the other hand, it would be incautious to state that wind turbine flows are practically *Re*-independent. Although computer capabilities have increased dramatically over the years, simulation of some flow features, in particular the blade boundary layer, is still not feasible – the blade boundary layer has been somewhat indirectly modeled through the airfoil force coefficients. The blade boundary layer is very likely to be dependent from the Reynolds number in many respects (separation and transition points, re-attachments among others). Consequently, it should be said that the resolved scales are not significantly influenced by the Reynolds number, while it is possible that a dependence occurs at smaller scale level.

4.3 Conclusions

The results of LES of a single wind turbine have been shown and discussed. With respect to classic engineering methods employed for wind turbine flow analysis LES certainly represents a most expensive tools in terms of computational resources and computational time.

However it has been shown that the expense is worth, since LES is capable of providing accurate results and overcome some drawbacks that engineering methods have because of their simplifying assumptions. These models fail in correctly predicting the wake behaviour, while they provide quite good results on overall perfomances such as the power production of a single turbine. However, this former aspect is crucial since the interaction between a turbine wake and the trailing turbines in clustered configurations affects significantly the performances of the waked turbines and thus of the whole park of turbines. The large demand of energy from renewable sources is leading to the construction of larger and larger wind farms and so a good understanding of wake interactions is necessary to optimise efficiency and management of these wind parks.

Furhtermore, the use of LES guarantees an unprecendentedly large amount of informations on flow features which can give a deep insight into the flow mechanisms. Once this knowledge is acquired and mastered could also be exploited for optimisation of wind turbine components design, for instance.

Chapter 5

Effects of Subgrid-Scale Modeling

In this chapter the effect of the SGS tensor modeling is investigated. The subgrid scale tensor plays a very important role in LES and is generally expected to have a significant impact on the quality of the results.

All the simulations performed in Chapter 4 employed the classic Smagorinsky model which has the valuable advantage of being very efficient from a computational point of view and also very simple to be implemented. However, as reported in Section 2.3.2, the Smagorinsky model suffers from the following major drawbacks which can have a potential negative impact on the LES of wind turbine flows:

i. isotropy

ii. flow-dependent model constant

iii. non-vanishing eddy viscosity in presence of a solid wall

Though many more sophisticated SGS models have been employed over the years, a systematic analysis to assess the influence of subgrid tensor modeling on the results has not been addressed in the literature so far for the flow past wind turbines. A recent exception is consituted by the work of Sarlak *et al.*[75]. A comparison between the Smagorinsky model and two "mixed scale" models, in which the velocity scale used to build the SGS viscosity is obtained from a scale-similarity model [71], was carried out. It was found that the impact of the turbulence models on the results is smaller compared to that of other parameters which were considered. This insensitivity was attributed to the common belief that, as long as the large scales features of wake-dominated flows – such as wind turbine flows – are correctly represented in the simulation, the impact of the smaller scales is negligible.

Nontheless, the analysis in this thesis is justified by the fact the turbine tower and nacelle are directly represented in the present simulations through the Immersed Boundary Method, while in [75] they were represented through the introduction of volume forces in the domain. Santoni & Leonardi[74] have shown the importance of taking into account the presence of the two bodies for accurately representing the near wake field and demonstrated that the IBM

provides close agreement with experimental results for the same configuration considered in the present analysis. It may expected that the characteristics of the SGS model do have an impact on the results, especially in the region of separated flow behind the tower and in proximity of the bodies walls.

5.1 Numerical setup

The numerical setup of the simulations performed for the SGS modeling evaluation reproduces that of the experiment conducted at the Norwegian University of Science and Technology (NTNU) in 2011[39]. A small wind turbine was placed inside the wind tunnel facility at NTNU and various measurements were performed.

The experiment was designed to provide a benchmark case against which to test CFD codes within the blindtest organised jointly by NOWITECH and NORCOWE[39]. In view of this aim the turbine was not designed to represent a realistic machine, but rather its geometry was designed in an easily reproducible way. Details of the design can be found in [39, 40, 16].

For the same reason the rather large size of the turbine compared to the tunnel dimensions was not considered to be an issue. Indeed, if the numerical setup faithfully reproduces the experimental configuration the blockage effects, which are expected to be rather large given a blockage factor[1]around 12%, will be included in the results with no need of corrections.

Furthermore the experiment was designed so as to have a uniform velocity and a low level of turbulence intensity at the inlet of the test section. This kind of incoming flow is not representative of realistic operating conditions. However it is easily reproducible by numerical codes and thus is well-suited for the aim of the experiment.

A schematic representation of the experimental (and numerical) setup is shown in Figure 5.1. The rotor diameter D is 0.894 m and the inflow velocity is $U_\infty = 10\,\mathrm{m\,s^{-1}}$. This gives a Reynolds number based on the turbine diameter and the incoming velocity of $Re = U_\infty D/\nu = 6.3 \cdot 10^5$

The numerical configuration was set to reproduce the experimental one. A no-slip condition was prescribed at the lower and upper buondary to mimick the tunnel walls. The lateral walls were simulated through the IBM method, as well as the tower and the nacelle. A no-slip condition was assigned at these "boundaries" too.

At the inflow a uniform velocity was assigned in agreement with the experimental inlet. At the outflow, the same radiative boundary condition in Eq. (4.26) was applied.

The turbine rotor was modeled with the RADM. This choice was suggested by the necessity of performing various simulations for testing the SGS models. Therefore the RADM was preferred to the ALM for computational reasons.

[1]The blockage factor is defined as the ratio between the frontal area of the model tested S to the area of the wind tunnel cross section A. Common values for S/A are around 5-10% for which an appreciable correction is necessary [15].

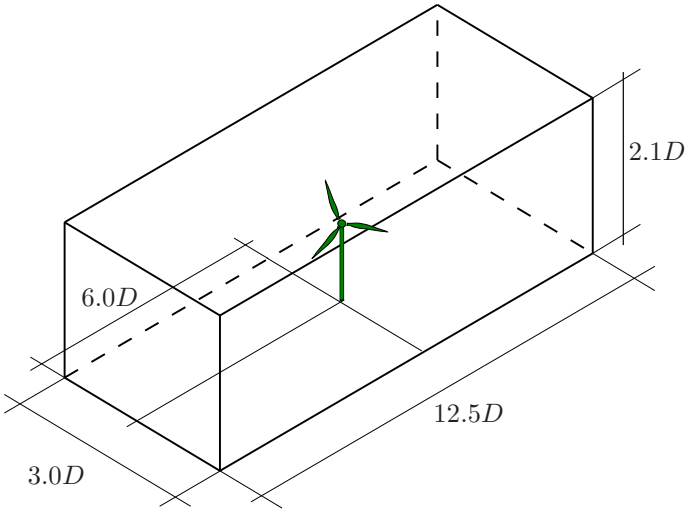

Figure 5.1: Experimental and numerical configuration

Despite this involves a moderate loss in accuracy, as it was shown in Section 4.2.2 most of the important wake features are still retained.

5.2 *A priori* tests

Before directly evaluating the perfomances of SGS models in LES of wind turbines *a priori* tests were conducted to obtain preliminary information on the models behaviour. *A priori* tests are a validation method which is based on the knowledge of the 'exact' solution of the problem under consideration [71]. The explicit application of a filtering operator leads to the definition of a resolved field and a known subgrid one. In this way the predictions yielded by the application of the model to the resolved, filtered, field can be compared with the 'exact' subgrid field. The 'exact' solution is usually obtained through a well-resolved Direct Numerical Simulation, generally performed at rather low Reynolds number because of computational limitations.

A priori tests can give useful information on models behaviour and on hypothesis underlying modeling efforts. However, it must be noted that numerous factors which concur in an actual simulation (*a posteriori* test) to determine the overall quality of the results – and therefore the quality of the SGS model – cannot be included in this kind of analysis. In practice the field obtained from an actual LES would be different from the resolved field obtained from the 'exact' solution because of modeling and numerical errors [71]. For this reason, the conclusions drawn from *a priori* tests can be misleading sometimes and a thorough analysis should include both *a priori* and *a posteriori* tests.

5.2.1 Test case

For the present analysis a no-model simulation was carried out on a rather fine grid at $Re = 10\,000$ for an operating constant $TSR = 3.0$. Details of the uniform grid employed are reported in Table 5.1.

axis	range	N_{points}	$\Delta x_i/D$
x	$[0 : 12.5D]$	1024	0.012
y	$[0 : 2.1D]$	512	0.004
z	$[0 : 3.0D]$	512	0.006

Table 5.1: Mesh details

The velocity field obtained from this simulation has been filtered with a second-order commuting discrete filter [89]. Given the discrete unfiltered mono-dimensional variable $\phi_k = \phi(x_k)$ this filtering operation reads as:

$$\tilde{\phi_k} = \sum_{l=-1}^{l=1} w_l \phi_{k+l} \tag{5.1}$$

where the weights w_l are given by:

$$w_{-1} = \frac{1}{4} \qquad w_0 = \frac{1}{2} \qquad w_1 = \frac{1}{4} \tag{5.2}$$

The filtering operation has been performed in all three directions by tensorization of the kernel (5.1). A comparison between the unfiltered and the filtered field is provided in Figure 5.2 where color contours of the time-averaged streamwise velocity are reported for the vertical plane passing through the tower axis.

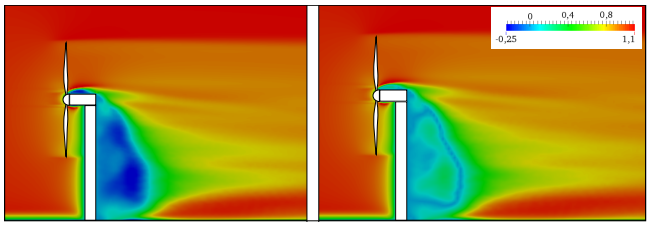

Figure 5.2: Color contours of time-averaged streamwise velocity in the tower axis vertical plane: left unfiltered field, right filtered field

The SGS models described in Section 2.3.2 were tested. The models input parameters are shown in Table 5.2

For the Smagorinsky model, the value of the constant was chosen according to the test performed with the Dynamic model for the NREL turbine described in Section 4.2.1. As for the other eddy-viscosity models, the value was chosen following the respective authors' suggestions. Tests with the Dynamic model were also carried out. The dynamic model parameter resulting from Eq. (2.38) was averaged in time.

SGS model	constant
Smagorinsky	$C_s = 0.09$
σ-model	$C_\sigma = 1.35$
Vreman	$C_V = 2.5\, C_s^2$
WALE	$C_W = 0.5$

Table 5.2: LES models input parameters

5.2.2 Results

In this section the results of the *a priori* tests are reported. The average in time of a variable $q(x, y, z, t)$ is defined as:

$$\langle q \rangle (x, y, z) = \frac{1}{T} \int_{t_0}^{t_0+T} q(x, y, z, t)\, \mathrm{d}t \tag{5.3}$$

where the initial time t_0 is chosen such that the turbine wake has fully developed in the domain (i.e. it has reached the outlet) and the sampling time T is large enough for the statistics to be converged.

In Figure 5.3 color contours of time-averaged eddy viscosity in the tower axis vertical plane are shown. The subgrid viscosity assumes large values in the wake, especially in the re-circulating region behind the tower (cf. Figure 5.2). This result was expected since the presence of the bluff body causes separation of the boundary layer and transition to turbulence. The interaction with the helicoidal wake of the rotor causes the early breakdown of the coherent vortices and the diffusion of vorticity. This enhances the mixing further and so the eddy viscosity increases.

The eddy viscosity predicted by the WALE model has generally the highest value among the considered models and locally attains very large values. On the other hand the Vreman model provides the lowest values in the domain. These trends are in accordance with previous studies on the same models [63]. The σ-model lies between the WALE model and the Smagorinsky model.

The Dynamic model is characterised by large fluctuations in space. As already discussed in Section 2.3.2 these fluctuations are likely to cause numerical instability: this was indeed the case when *a posteriori* tests were performed. This suggests the use of a different kind of average for the constant computation. This is a typical problem in LES of inhomogeneous flows, such as wind turbine flows. The lack of homogeneous directions along which to perform ensamble averages requires the adoption of more complex kinds of average rather than the simple time-averge which may not provide enough samples for the average to be converged.

In Figure 5.4, color contours of $\langle \nu_{\mathrm{sgs}} \rangle$ in the horizontal plane at hub height are reported. The figure confirms the observations made above regarding the value of the eddy viscosity predicted by the SGS models. Again the largest values are found in the tower and nacelle wake region, with only the WALE model presenting a subgrid viscosity significantly different from zero in the tip region. This region is generally characterised by a high shear, although in this case it is rather low because of the slow rotation of the blades ($TSR = 3$) and

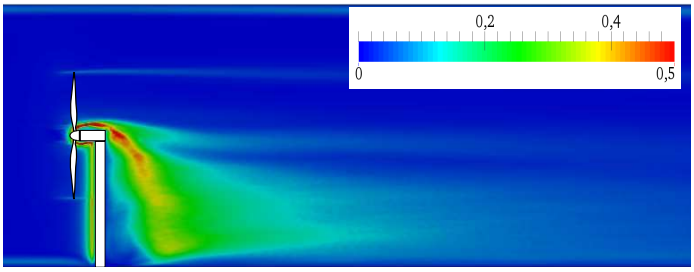

(a) Smagorinsky model

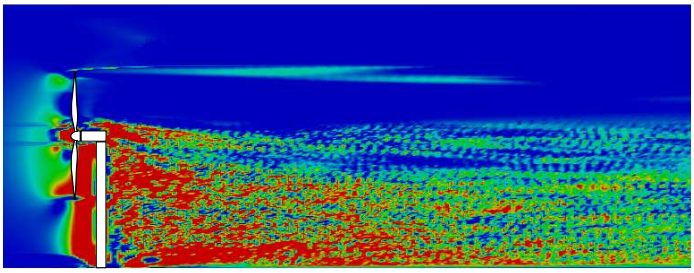

(b) Dynamic model

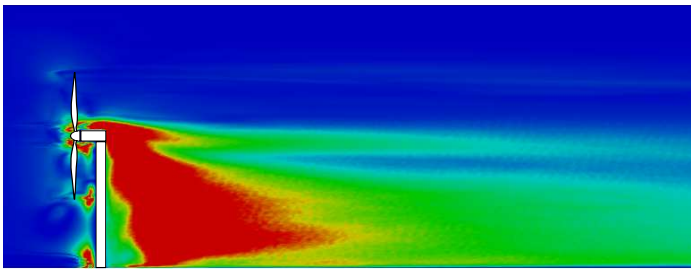

(c) σ-model

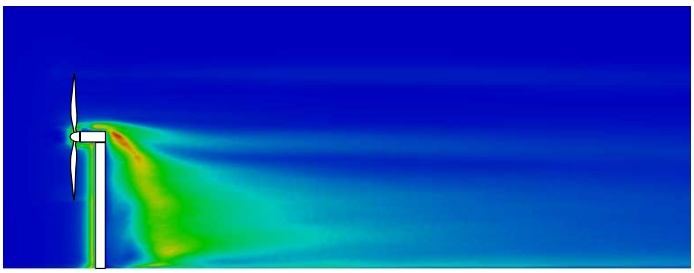

(d) Vreman model

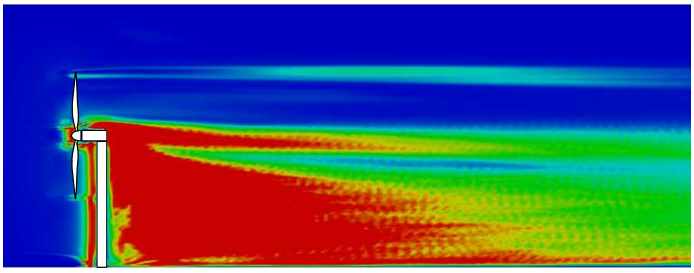

(e) WALE model

Figure 5.3: Color contours of $\langle \nu_{\text{sgs}} \rangle / \nu$ in the vertical passing through the tower axis

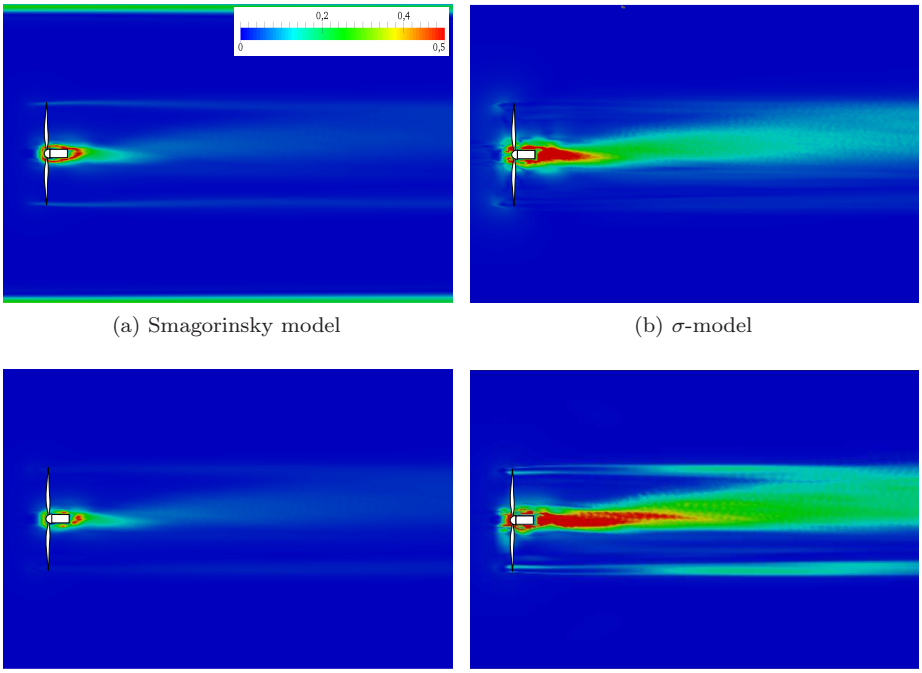

(a) Smagorinsky model (b) σ-model

(c) Vreman model (d) WALE model

Figure 5.4: Color contours of $\langle \nu_{\text{sgs}} \rangle / \nu$ in hub plane

the consequent moderate intensity of the tip vortex.

It is important to notice that the Smagorinsky model yields a non-zero viscosity near the vertical walls of the wind tunnel. This is due to the fact that the model constant was not damped in this region whereas van Driest correction, Eq. (2.31), is succesfully implemented for the bottom wall (see Fig. 5.3a). Conversely, the other models show the expected vanishing viscosity.

The near wall behaviour of the SGS models is particularly interesting in the area where the tower and nacelle are present. In fact the complex geometry of the two bodies makes the use of van Driest correction unfeasible. Therefore the possibility to adopt a SGS model which yields the correct value of the subgrid viscosity eliminates a potential source of error. However, from Figure 5.3 it appears that the viscosity is non vanishing near the immersed boundaries. This is confirmed in Figure 5.5 where color contours of $\langle \nu_{\text{sgs}} \rangle$ in the vertical plane passing through the tower axis normal to the flow direction.

Although a slight improvement respect to the Smagorinsky can be noticed, at least for the Vreman and σ-model, the overall result is not as expected. This may be due to the filtering operator which introduces an errors near the body contour: possibly the adoption of a high-order filter may improve the results. Also an increase in the grid resolution is bound to yield better outcomes because the description of the body contour would be more accurate. Indeed only a few points are inside the nacelle volume which is the body for which the results are farthest from the expected values.

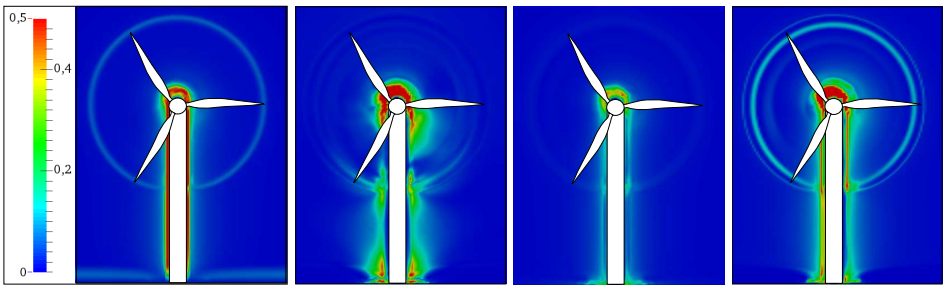

(a) Smagorinsky model (b) σ-model (c) Vreman model (d) WALE model

Figure 5.5: Color contours of $\langle \nu_{\text{sgs}} \rangle / \nu$ in the tower axis cross-sectional plane.

Figure 5.6 shows color contours of the subgrid dissipation $\langle \varepsilon_{\text{sgs}} \rangle = \langle \tau_{ij} \overline{S}_{ij} \rangle$ in the vertical plane through the tower centreline.

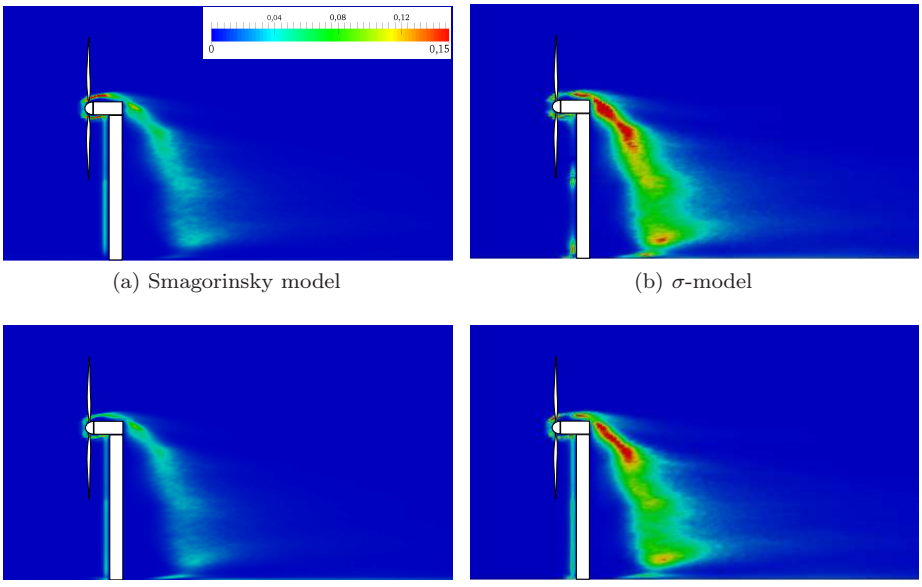

(a) Smagorinsky model (b) σ-model

(c) Vreman model (d) WALE model

Figure 5.6: Color contours of $\langle \varepsilon_{\text{sgs}} \rangle$ in vertical plane through the tower axis.

It is evident that the Vreman model is the least dissipative model. This result could have been anticipated from the low values predicted for the eddy viscosity (see Figs. 5.3-5.4). When *a posteriori* tests were performed the subgrid dissipation proved to be too small and the solution diverged. This suggests that the value adopted for the model constant (see Table 5.2) should be increased for the sake of numerical stability. Determine the value of the model constant for a complex type of flow, like the one under consideration, is one of the most concerning problems in the LES framework. Since analytical theories are scarcely available for complex turbulence problems, it is often difficult to find a basis upon which to evaluate the constant.

5.2.3 Conclusions

From the *a priori* tests it can be concluded that the value of the eddy viscosity model is strongly affected by the model employed. In particular the WALE model provides the highest values and the Vreman model the lowest one. The σ-model is intermediate between the WALE model and the classic Smagorinsky.

As it has already been anticipated, this results in different estimates for the subgrid dissipation with the Vreman model being not enough dissipative. Indeed, it was not possible, during the simulation, to avoid instability. A possible overcome can be an increase in the value of the model constant.

The models near wall behaviour was also addressed . The models did not provide the expected result near the immersed buondaries. The use of the σ-model, Vreman model and WALE model instead of the traditional Smagorinsky model may then be questioned on the basis of these *a priori* results.

However for a thourogh assessment of the models performances it is worthy to carry out *a posteriori* tests since no additional computational expense is involved with the use of these models compared to the Smagorinsky model. Moreover, as stressed above, the outcome of an actual LES can be quite different from the prediction of the *a priori* validation due to the interaction between the SGS model and the numerical code.

5.3 *A posteriori* tests

A posteriori tests consist actually in performing an LES. This is a dynamic evaluation of the SGS model performance which takes into account all the factors occurring in a simulation.

Indeed, these *a posteriori* tests cannot give the same insight on modeling hypotheses as the *a priori* validation since it is not possible to evaluate the extent of the modeling errors respect to the other sources of error (numerical error, resolution error etc...) [71].

Nevertheless, good *a posteriori* results are what definitely matters for the success of the LES approach [65].

5.3.1 Test case

The LES were carried out at $Re = 6.3 \cdot 10^5$, the same as in the experiment. The tip speed ratio at which the turbine is operating is $TSR = 3.0$ as in the *a priori* tests. The grid employed for the simulations is uniform in the three directions and is coarser respect to the one used for the *a priori* tests. Details are reported in Table 5.3.

For the SGS models, the same input parameters in Table 5.2 were adopted for the large-eddy simulations. Simulations with the Vreman and the Dynamic model were not successfully terminated due to numerical instability. As already discussed in the *a priori* validation, the Vreman model is not enough dissipative. This result is in accordance with the findings of a similar study [63] where an

axis	range	N_{points}	$\Delta x_i/D$
x	$[0 : 12.5D]$	512	0.024
y	$[0 : 2.1D]$	256	0.008
z	$[0 : 3.0D]$	256	0.012

Table 5.3: Mesh details

increased value of the numerical viscosity was adopted when this model was used. This suggests that the model constant should be increased or possibly that the relation (2.45), approximately derived for homogeneous isotropic turbulence, is not as accurate for highly anisotropic flows.

The Dynamic model, on the other hand, suffers from an inadequate constant averaging. In order to smooth the constant large fluctuations a more robust average than the time-average could be used. Indeed, several authors employ local averaging or Langrangian averaging [25, 97, 49].

5.3.2 Results

In this section the results of the large-eddy simulations are presented. The average in time is defined as in Equation (5.3).

In Table 5.4 the time-averaged power and thrust coefficient, C_P and C_T respectively, are shown together with the values yielded by the BEM code described in Section 4.1 and the ones measured at NTNU.

		C_P	C_T
LES:			
	Smagorinsky model	0.190	0.327
	σ-model	0.171	0.302
	WALE model	0.162	0.294
BEM		0.126	0.303
Exp.		0.120	0.393

Table 5.4: Power and thrust coefficient: experimental results are taken from [40]

The predictions of the three models are similar, with the Smagorinsky model yielding higher coefficients compared to the other eddy viscosity models. When compared to the experimental results the three models show a similar trend with the power coefficient being overpredicted and thrust coefficient being underestimated. The difference of LES results from the experimental measurements should not be deemed too negative since it is in line with the state of the art in predicting turbine performances. In Figure 5.7 the results of the blindtest organised by NOWITECH and NORCOWE are reported. A large scatter for on- and off-design conditions is observed.

A considerable disagreement with the experimental results was generally found in the blindtest. No correlation was found systematically between the model employed and the accordance with results, with BEM codes being in

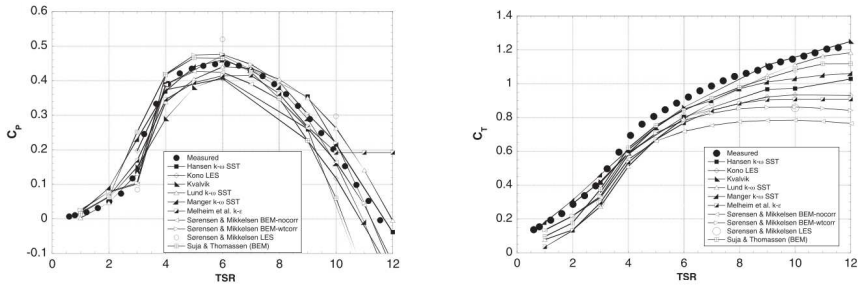

(a) Power coefficient (b) Thrust coefficient

Figure 5.7: Results of the NOWITECH/NORCOWE Blind Test: reproduced from [39]

some case as good as (or more than) LES – which are expected to yield the most accurate predictions. This shows how, at the present state, prediction of C_P and C_T remains probably the most demanding problem in wind turbine flows.

Moreover, the case considered in the present simulations is particularly challenging, because the tip speed ratio is quite far from design condition ($TSR = 6.0$) and the blade is almost fully stalled [39]. This may also give a key to understand the reason for the lack of agreement obtained. In fact, when an airfoil is working in stalled conditions the 3D effects are most evident. Consequently, it is reasonable to expect the 2D theory employed for the force prediction (see Section 2.4) being quite inaccurate. This last argument is supported by the fact that the scatter among LES simulations is rather low and the BEM code yields a very good estimate of the C_P: this is quite surprising since this method does not take into account the blockage effect which, as stated above, is expected to be not negligible.

In Figures 5.8a-5.8b the time-averaged streamwise velocity profiles at hub height at two different downstream positions are reported together with experimental results for comparisons.

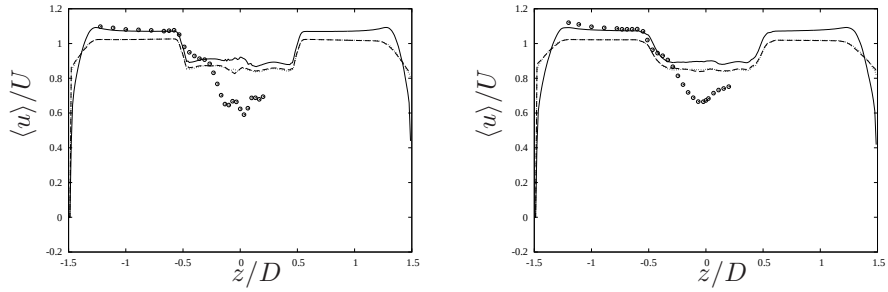

(a) $1.0D$ downstream rotor position (b) $3.0D$ downstream rotor position

Figure 5.8: Time-averaged streamwise velocity profile at hub height: Smagorinsky (———), σ-model (·····), WALE (– – – –); ∘ experiments.

In Figures 5.9a-5.9b the time-averaged Turbulent Kinetic Energy profiles at

hub height at the same downstream positions are shown.

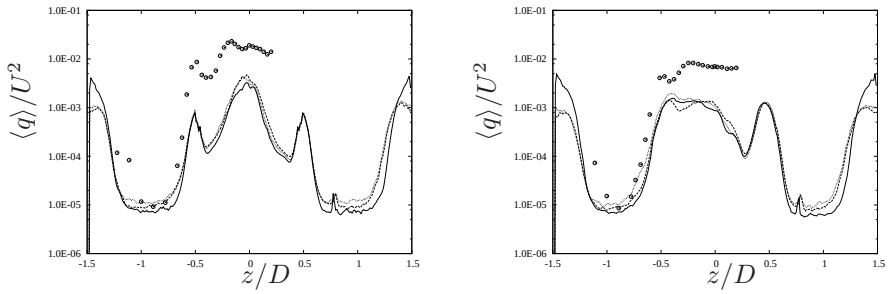

(a) $1.0D$ downstream rotor position (b) $3.0D$ downstream rotor position

Figure 5.9: Time-averaged streamwise TKE at hub height: Smagorinsky (———), σ-model (·····), WALE (– – – –); ∘ experiments.

The three models yield similar predictions. The results in Figure 5.8 are actually quite surprising since the same code used in the present thesis provided excellent agreement with the experimental measurements [74]. The reason for this discrepancy may be found in the different model employed for representing the turbine rotor. While in [74] the more accurate ALM is used, the RADM adopted for these simulations may to a certain extent 'shadow' the effect of tower and nacelle which are the cause of the large velocity deficit in the centre of the wake, as was shown in [74]. The different predictions may also be affected by the coarser resolution which is used in the present simulations.

In Figure 5.9 the shape of the profile is reproduced quite well although the magnitude of the TKE is underestimated in the core of the wake. This is in accordance with the trend observed in Section 4.2.2 regarding the smoothing effect that the RADM has on the small scale turbulence which is generated by the rotor blades. The TKE predicted by the RADM was found to be lower compared to the ALM field especially in the near wake region.

Overall the comparison with the reference results is satisfactorily, with discrepancies being of the same order as, or less than, those observed within the blindtest comparison [39].

The Smagorinsky model furnishes higher values of the turbulent kinetic energy near the lateral wall of the tunnel respect to the other two models, Fig. 5.9. It is believed the latter models reproduce a more realistic value of the turbulence intensity. It must be remembered that there is no damping of the model constant in this region of the domain (cf. Figure 5.4a) and the eddy viscosity is too large. This is confirmed also by the velocity profiles in Figure 5.8: the SGS model drains too much energy from the resolved field and the velocity is lower in the boundary layer. The visualisation of the TKE field in Figure 5.10 is in accordance with the previous arguments.

This different behaviour can be further appreciated in Fig. 5.11 where color contours of vorticity magnitude are shown in the horizontal plane at hub height.

The higher value of the eddy viscosity indicates a higher level of turbulence activity. The mixing is enhanced and the vortical structures are diffused more rapidly away from the wall.

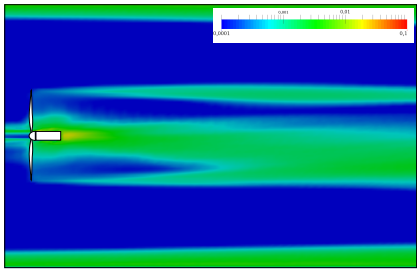

(a) Smagorinsky model

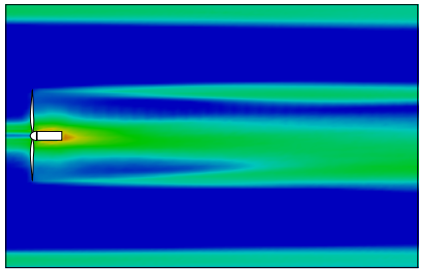

(b) WALE model

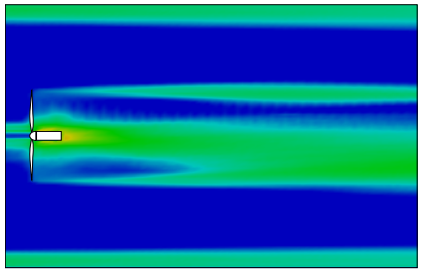

(c) σ-model

Figure 5.10: Color contours of time-averaged TKE in the hub plane

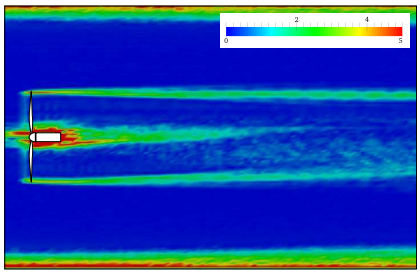

(a) Smagorinsky model

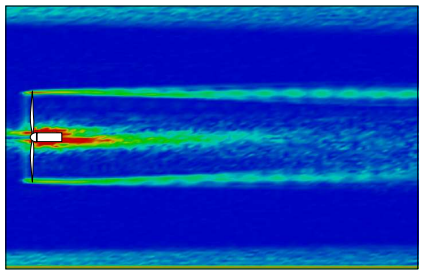

(b) WALE model

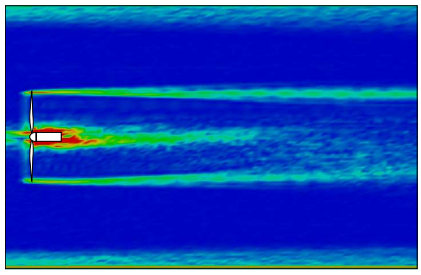

(c) σ-model

Figure 5.11: Color contours of vorticity magnitude in the hub plane

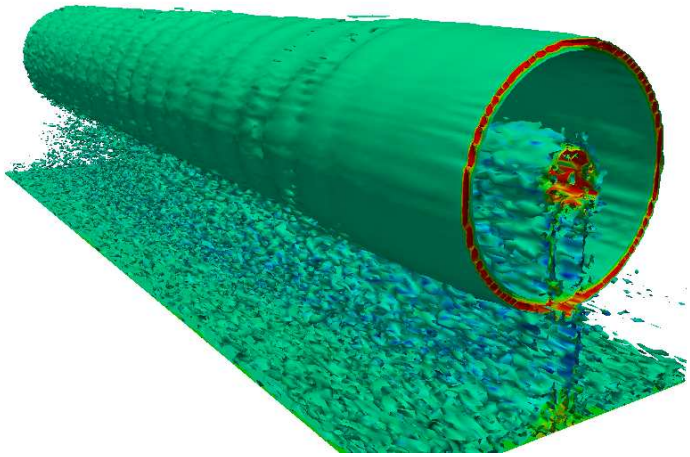

Figure 5.12: Iso-surfaces of vorticity magnitude: WALE model

Though the *TSR* is low it is not possible to distinguish the tip vortices in Fig. 5.11. The lack of these details, which was partially expected, was already observed when comparing the RADM with the ALM (see Fig. 4.19). However, it is worthy to notice that in Fig. 5.11 a vortical structure is observed in the far wake which appears similar to the helicoidal path formed by the tip vortices. Instead, those vortices are not helicodail but are rather 'ring' vortices which develops for Kelvin-Helmoltz instability [8] due to the shear which occurs between the free-stream region and the turbine wake (cf. Fig. 5.8). This structure can be appreciated in Figure 5.12 where iso-surfaces of vorticity magnitude are shown.

In general the results do not seem to be significantly affected by the SGS models. A similar trend is observed for the time-averaged streamwise velocity and the turbulent kinetic energy in the vertical plane thorugh the tower centerline shown in Figures 5.13 and 5.14.

The recirculation bubble behind the tower shows a moderate sensitivity to the model employed. The length of the recirculation bubble is larger for the least dissipative Smagorinsky model and shorter for the WALE and σ-model which according to the *a priori* tests provide a larger amount of subgrid viscosity. This behavior is more evident below the rotor bottom tip where the interaction with the turbine wake is less significant. The same dependence on the SGS viscosity was found in a previous study on the flow past a circular cylinder [63].

While a dependence on the SGS models is scarcely observed on flow features, some differences can be observed in the prediction of the eddy viscosity. Color contours of the time-averaged eddy viscosity $\langle \nu_{\text{sgs}} \rangle / \nu$ are shown in Figure 5.15.

In Figure 5.16 the time-averaged subgrid dissipation $\varepsilon_{\text{sgs}} = \tau_{ij} \overline{S}_{ij}$ is also shown.

All models result to be more dissipative and provide a higher subgrid viscosity than what was predicted from the *a priori* tests. Apart from the model-simulation interaction mentioned above, this behaviour can also be related to the quite different Reynolds number. Even though the overall flow features were shown not to be severely affected by the Re in Section 4.2.2, the eddy viscosity

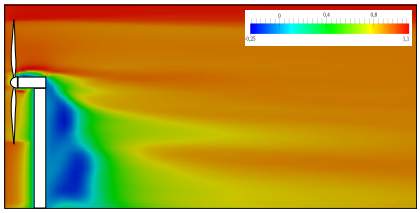

(a) Smagorinsky model

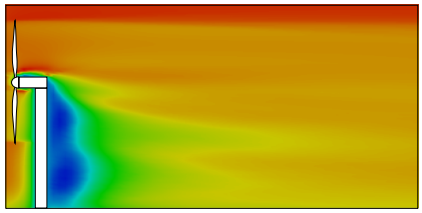

(b) WALE model

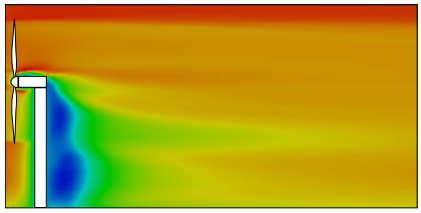

(c) σ-model

Figure 5.13: Color contours of time-averaged streamwise velocity in the tower axis vertical plane

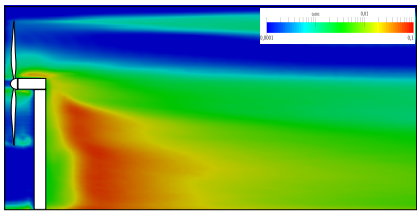

(a) Smagorinsky model

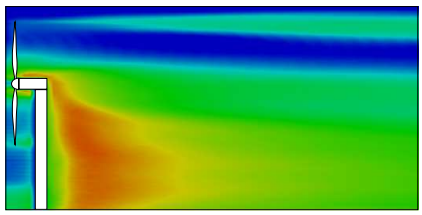

(b) WALE model

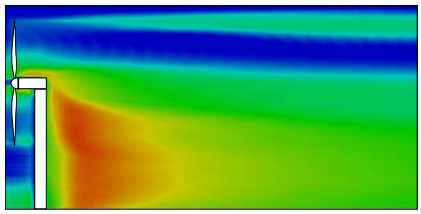

(c) σ-model

Figure 5.14: Color contours of time-averaged TKE in the tower axis vertical plane

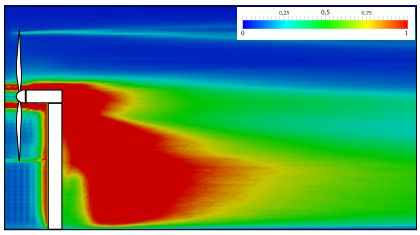

(a) Smagorinsky model

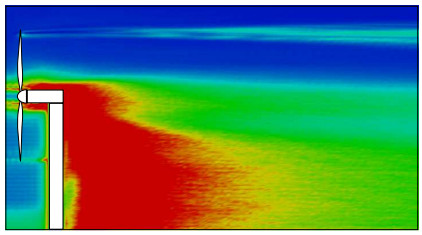

(b) WALE model

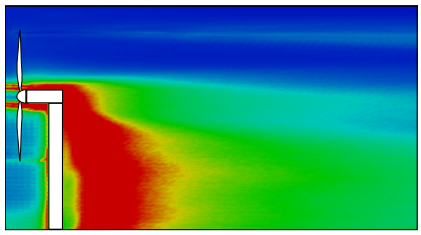

(c) σ-model

Figure 5.15: Color contours of time-averaged $\langle \nu_{\text{sgs}} \rangle / \nu$ in the tower axis vertical plane

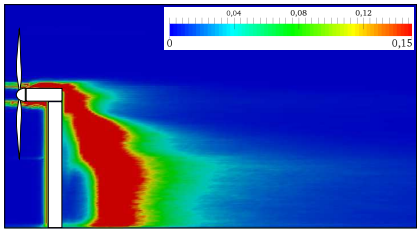

(a) Smagorinsky model

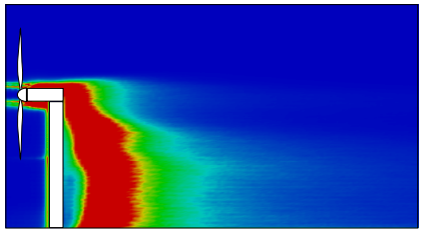

(b) WALE model

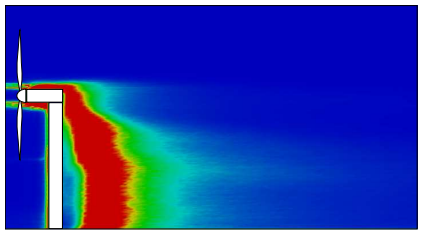

(c) σ-model

Figure 5.16: Color contours of time-averaged $\langle \varepsilon_{\text{sgs}} \rangle$ in the tower axis vertical plane

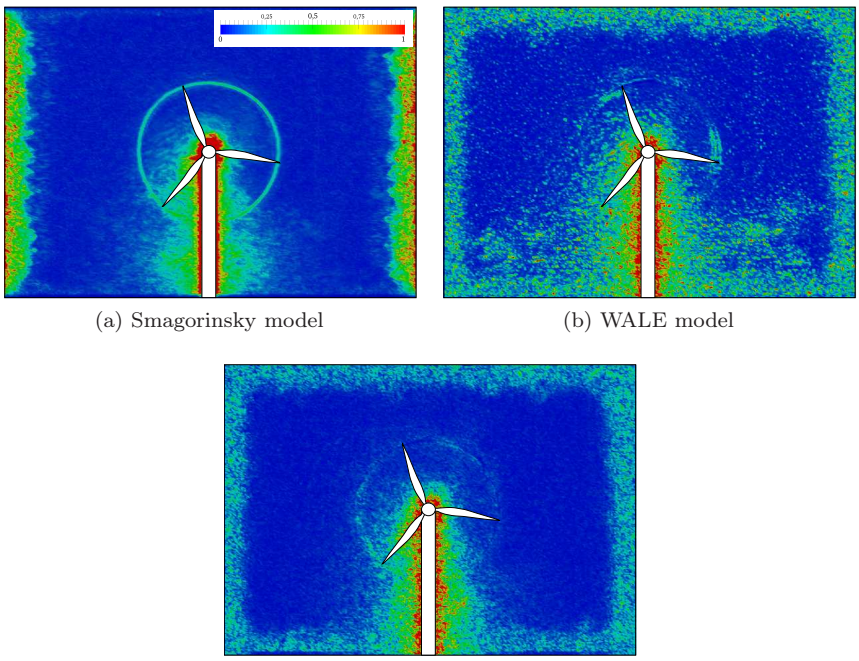

(a) Smagorinsky model

(b) WALE model

(c) σ-model

Figure 5.17: Color contours of instanteneous $\langle \nu_{\text{sgs}} \rangle / \nu$ in the tower axis vertical plane normal to the flow direction

does depend on the Reynolds number. Moreover, the grid employed for the *a posteriori* tests is coarser than the one employed for the *a priori* tests: consequently the subgrid-scale contribution is expected to be larger. Some trends previously individuated have been confirmed. The WALE model is globally more dissipative with the σ-model being intermediate between the Smagorinsky the WALE models.

As for the near wall behaviour, the *a posteriori* tests do not show an improvement respect to the prediction of the *a priori* tests. Both the WALE model and the σ-model yield a non vanishing eddy viscosity near the immersed boundaries. This is shown also in Figure 5.17.

This results may possibly be improved by the use of a finer grid or by an *ad hoc* modification of the Immersed Boundary procedure. Indeed, with the resolution reported in Table 5.3 approximately only 4×10 gridpoints are present inside a horizontal section of the tower which may not guarantee an accurate description of the geometry.

5.3.3 Conclusions

Large-eddy simulations employing different SGS models have been performed. The accordance with the reference experimental measurements was not excellent but comparable to the state of the art. The flow past wind turbines poses particular challenges to researchers because of the wide range of scales active in the flow, the turbulent motion and anisotropy. More accurate modeling, especially

of wind turbine rotors, is required to improve predictions.

Conformly to a similar study in the literature [75], the impact of the SGS model on the result is found to be rather small. The main flow features are dependent especially on the large scale structures which are directly simulated and thus the effects of the subgrid tensor is evident mainly in secondary aspects (such as the tower wake mean recirculation length). Possibly a major sensitivity could be devised employing ALM rather than RADM. This latter method does not describe in very detail small scale sctrutures – for example the tip vortex – where the influence of the SGS model could be significant.

The behaviour of the eddy viscosity near the bodies walls was also investigated. Although results were not encouraging, this respect may be further analysed possibly with the finer body resolution which permits an accurate description of the geometry.

Chapter 6

Conclusions

Large-Eddy Simulations have been applied to the flow past wind turbines and wind farms only in recent years. Its diffusion is yet to be large because of the computational requirements that this technique involves. The standard tools for the prediction and the analysis of wind turbine performances are still represented by the simple engineering models. These tools are easy to be implemented and capable of providing results in a very short time. These models often rely on simplifying assumptions about flow behaviour whose derivation and validity are rather questionable from a physical point of view.

The numerical evaluations performed have shown that the wind turbine wakes are a turbulent inhomogeneous anistropic flow. It is very hard to give a simple analytical description of its features: no evidence of axisymmetry or uniformity, as assumed by wake models, was observed.

The wake evolution was found to be significantly influenced by the turbulence level. The highest the turbulence intensity the faster is the wake recovery. It is very important to take into account the dynamics of turbulent motion when dealing with wind turbine wakes. In fact, a faster wake recovery would allow manufacturers to reduce the turbine spacing in clustered configuration and to reduce the size of a wind park or to increase the number of turbines, and thus the total power, within the same area. On the other hand, turbulence is the cause for fluctuating fatiguing loads on the turbine structure and this is a concern from the point of view of durability and maintenance.

These considerations would have a significant impact in the design process of a new wind farm or in the management strategy of an existing one. Consequently it is evident that it is very important to take into account turbulent motion. Unfortunately turbulence is a very complex phenomenon whose dynamics and effects are difficult to be parameterised within simple analytical models such as wake models.

Therefore LES represents a valuable method to obtain accurate predictions and gain a deeper knowledge of flow mechanisms. In fact, the real advantage of using LES lies not only in the possibility of obtaining more reliable estimates on overall performances such as the power production – for which, at least for the single turbine configuration, wake models are quite accurate –, but also in the rich amount of information which is provided by these simulations.

LES furnish a detailed description of the aerodynamic field which is not even comparable to the output of wake models. These data can provide a physical insight into flow dynamics and allow engineers and researchers to understand physical mechanisms which occur in the flow and so to control and master them. We believe that this analysis is even more important than the simple prediction of a particular turbine production because can give a fundamental knowledge on the flow dynamics which can be exploited in every future application. This is an invaluable feature which LES can bring to the analysis of wind turbine flows.

In LES of wind turbine flows the rotor is modeled through the forces it applies to the flow. A new model, the Rotating Actuator Disk Model, was proposed. The model was validated against the more accurate, but more time-expensive, Actuator Line Model. An overall good agreement between the predictions of the two models was observed. Indeed, the average velocity field obtained from RADM simulations is very similar to that of ALM ones. Some discrepancies were found when comparing turbulence kinetic energy fields. This is explained by the fact that the RADM is not capable of representing all the small scales structure which characterises the wake and give a non-negligible contribution to TKE.

Overall the RADM retains most of the essential features of the wake. Its main advantage lies in the relaxation of numerical time-step constraints which are connected to the use of the ALM. Since the computational resources required to perform LES represents a major concern in its use, this can be positively regarded as being a minor step towards the industrial feasibility of LES of wind turbines flows.

The effect of the subgrid-scale model was also investigated. The SGS model plays a key role in LES since it is expected to introduce the small scales which are not directly simulated. Various eddy-viscosity models have been tested. Eddy-viscosity models are a classic and widely used method for describing the subgrid-scales interactions, even if they may not give the most accurate description of the subgrid scales structures, but just reproduce their global average effect.

Though the eddy-viscosity itself showed a pronounced dependence on the model, the overall results were rather insensitive to it. This is probably due to fact that the variable analised are rather dominated by the large scale flow features which are directly represented on the computational grid and somewhat independent to the subgrid modes. Averaged velocity fields as well as vortical structures seem to be more sensitive to other flow parameters, primarily the turbine model. Overall performances, such as power and thrust, showed a similar trend with the various models yielding similar predictions. A similar study in the literature confirms this conclusion. Moreover the analysis focused more on the overall effect of the subgrid tensor, i.e. on its dissipative effect on the resolved kinetic energy. Possibly a more significant sensitivity may be devised considering detailed features of the SGS tensor such as the subgrid stress structures.

A small influence of the SGS model was observed in the recirculating region behind the tower which is directly represented in these simulations. The result is not surprising since this area is characterised by separated flow and turbulence modeling becomes important. Explicit simulation of the tower and the nacelle,

through the Immersed Boundary Method, is particular to the code presently employed, and it has been shown in previous works, and to a minor extent in this thesis, that it is crucial for an accurate representation of the near wake field.

Future works should possibly be aimed at improving rotor modeling which is crucial for the overall quality of the simulation. As for the SGS model further analysis is required, e.g. by investigating the effects of grid refinement or by focussing on the coupling between the different SGS models with the Immersed Boundary Method.

Bibliography

[1] M. Abkar and F. Porté-Agel. The effect of atmospheric stability on wind-turbine wakes: A large-eddy simulation study. *J. Phys. Conf. Ser.*, 524:012138, June 2014.

[2] J. Bardina, J. H. Ferziger, and W. C. Reynolds. Improved turbulence models based on large eddy simulation of homogeneous, incompressible turbulent flows. Technical Report May 1983, Stanford University, 1983.

[3] R. J. Barthelmie, L. Folkerts, G. C. Larsen, K. Rados, S. C. Pryor, S. T. Frandsen, B. Lange, and G. Schepers. Comparison of wake model simulations with offshore wind turbine wake profiles measured by sodar. *J. Atmos. Ocean. Technol.*, 23(7):888–901, 2006.

[4] G. K. Batchelor. *An introduction to Fluid Dynamics*. Cambridge University Press, 1967.

[5] A. Betz. Schraubenpropeller mit geringstem Energieverlust. Mit einem Zusatz von L. Prandtl. *Nachrichten von der Gesellschaft der Wissenschaften zu Göttingen, Math. Klasse*, pages 193–217, 1919.

[6] A. Betz. Das maximum der theoretisch möglichen ausnutzung des windes durch windmotoren. *Zeitschrift für das gesamte Turbinenwesen*, 26:307–309, 1920.

[7] M. L. Buhl. A New Empirical Relationship between Thrust Coefficient and Induction Factor for the Turbulent Windmill State. Technical Report August, NREL/TP-500-36834, 2005.

[8] G. Buresti. *Elements of Fluid Dynamics*. ICP fluid mechanics. Imperial College Press, 2012.

[9] M. Calaf, C. Meneveau, and J. Meyers. Large eddy simulation study of fully developed wind-turbine array boundary layers. *Phys. Fluids*, 22(1):1–16, 2010.

[10] M. J. Churchfield, S. Lee, P. J. Moriarty, L. A. Martínez-Tossas, S. Leonardi, G. Vijayakumar, and J. G. Brasseur. A Large-Eddy Simulation of Wind-Plant Aerodynamics Preprint. *50th AIAA Aerosp. Sci. Meet.*, pages AIAA 2012–0537, 2012.

[11] R. A. Clark, J. H. Ferziger, and W. C. Reynolds. Evaluation of subgrid-scale models using an accurately simulated turbulent flow. *J. Fluid Mech.*, 91(1):1–16, 1979.

[12] G. Comte-Bellot. *Contribution à l'étude de la turbulence de conduite*. Ph.d dissertation, University of Grenoble, 1963.

[13] R. Courant, K. Friedrichs, and H. Lewy. On the Partial Difference Equations of Mathematical Physics. *IBM J.*, 1967.

[14] J. W. Deardoff. A numerical study of three-dimensional turbulent channel flow at large Reynolds numbers. *J. Fluid Mech.*, 41(2):453–480, 1970.

[15] Engineering Sciences Data Unit. Blockage correction for bluff bodies in confined flows. Technical report, ESDU 80024, 1980.

[16] P. E. Eriksen and P.-Å. Krogstad. Experimental results for the NOWITECH/NORCOWE blindtest. *Energy Procedia*, 24(January):378–384, 2012.

[17] E. A. Fadlun, R. Verzicco, P. Orlandi, and J. Mohd-Yusof. Combined Immersed-Boundary Finite-Difference Methods for Three-Dimensional Complex Flow Simulations. *J. Comput. Phys.*, 161(1):35–60, June 2000.

[18] C. A. J. Fletcher. *Computational Techiniques for Fluid Dynamics*, volume 2. Springer-Verlag, second edition, 1991.

[19] U. Frisch. *Turbulence: The Legacy of A. N. Kolmogorov*. Cambridge University Press, 1995.

[20] R. E. Froude. On the part played in propulsion by differences of fluid pressure. *Transactions of the Royal Institution of Naval Architects*, 30:390, 1889.

[21] W. Froude. On the elementary relation between pitch, slip and propulsive efficiency. *Transactions of the Royal Institution of Naval Architects*, 19:47–57, 1878.

[22] M. Germano. A proposal for a redefinition of the turbulent stresses in the filtered Navier–Stokes equations. *Phys. Fluids*, 29(7):2323–2324, 1986.

[23] M. Germano. Turbulence: the filtering approach. *J. Fluid Mech.*, 238:325–336, 1992.

[24] M. Germano, U. Piomelli, P. Moin, and W. H. Cabot. A dynamic subgrid-scale eddy viscosity model. *Phys. Fluids A Fluid Dyn.*, 3(7):1760–1765, 1991.

[25] S. Ghosal and P. Moin. The Basic Equations for the Large Eddy Simulation of Turbulent Flows in Complex Geometry. *J. Comput. Phys.*, 118:24–37, 1995.

[26] H. Glauert. *The Elements of Aerofoil and Airscrew Theory*. Cambridge University Press, Cambridge, second (1946) edition, 1926.

[27] G. Grötzbach and U. Schumann. Direct numerical simulation of turbulent velocity, pressure and temperature fields in channel flows, 1979.

[28] S. Ivanell, J. N. Sørensen, R. Mikkelsen, and D. Henningson. Analysis of numerically generated wake structures. *Wind Energy*, 12(1):63–80, 2009.

[29] N. O. Jensen. A note on wind generator interaction. *Risø-M-2411 RisøNatl. Lab. Roskilde*, pages 1–16, 1983.

[30] A. Jimenez, A. Crespo, E. Migoya, and J. Garcia. Advances in large-eddy simulation of a wind turbine wake. *J. Phys. Conf. Ser.*, 75:012041, 2007.

[31] A. Jimenez, A. Crespo, E. Migoya, and J. Garcia. Large-eddy simulation of spectral coherence in a wind turbine wake. *Environ. Res. Lett.*, 3(015004):1–10, 2008.

[32] J. Jiménez and P. Moin. The minimal flow unit in near-wall turbulence. *J. Fluid Mech.*, 225:213–240, 1991.

[33] J. Jonkman, S. Butterfield, W. Musial, and G. Scott. Definition of a 5-MW reference wind turbine for offshore system development. Technical Report February, NREL/TP-500-38060, 2009.

[34] A. Kasahara and W. M. Washington. Global General Circulation Model of the Atmosphere. *Mon. Weather Rev.*, 95(7):389–402, 1967.

[35] C. A. Kennedy, M. H. Carpenter, and R. M. Lewis. Low-storage, explicit Runge-Kutta schemes for the compressible Navier-Stokes equations. *Appl. Numer. Math.*, 35:177–219, 2000.

[36] J. Kim and P. Moin. Application of a Fractional-Step Method to Incompressible Navier-Stokes Equations. *J. Comput. Phys.*, 59:308–323, 1985.

[37] J. Kim, P. Moin, and R. D. Moser. Turbulence statistics in fully developed channel. *J. Fluid Mech.*, 177:133–166, 1987.

[38] A. N. Kolmogorov. The local structure of turbulence in incompressible viscous fluid for very large Reynolds numbers. *Dokl. Akad. Nauk SSSR*, 30(1890):301–305, 1941.

[39] P.-Å. Krogstad and P. E. Eriksen. "Blind test" calculations of the performance and wake development for a model wind turbine. *Renew. Energy*, 50:325–333, 2013.

[40] P.-Å. Krogstad and J. A. Lund. An experimental and numerical study of the performance of a model wind turbine. *Wind Energy*, 15:443–457, 2012.

[41] P. K. Kundu and I. M. Cohen. *Fluid Mechanics*. Academic Press, fourth edition, 2008.

[42] A. Leonard. Energy cascade in large-eddy simulations of turbulent fluid flows. In *Advances in Geophysics: Turbulent Diffusion in Environmental Pollution*, volume 18, pages 237–248, 1974.

[43] S. Leonardi. Simulazione diretta di un flusso turbolento in un canale con cavità. Master's thesis, Università di Roma 'La Sapienza' – Dipartimento di Meccanica e Aeronautica, 1999.

[44] S. Leonardi. *Turbulent channel flow with roughness: Direct Numerical Simulations*. PhD thesis, Università di Roma 'La Sapienza' – Dipartimento di Meccanica e Aeronautica, 2002.

[45] M. Lesieur. *Turbulence in Fluids*. Fluid Mechanics and Its Applications. Springer, 2008.

[46] D. K. Lilly. A proposed modification of the Germano subgrid-scale closure method. *Phys. Fluids A Fluid Dyn.*, 4:633–635, 1992.

[47] H. Lu and F. Porté-Agel. A modulated gradient model for large-eddy simulation: Application to a neutral atmospheric boundary layer. *Phys. Fluids*, 22(1):015109, 2010.

[48] L. A. Martínez-Tossas, M. J. Churchfield, and S. Leonardi. Large eddy simulations of the flow past wind turbines: Actuator line and disk modeling. *Wind Energy*, 17:657–669, 2014.

[49] C. Meneveau, T. S. Lund, and W. H. Cabot. A Lagrangian dynamic subgrid-scale model of turbulence. *J. Fluid Mech.*, 319:353–385, apr 1996.

[50] J. Meyers and C. Meneveau. Large Eddy Simulations of large wind-turbine arrays in the atmospheric boundary layer. In *48th AIAA Aerosp. Sci. Meet. Incl. New Horizons Forum Aerosp. Expo.*, page 10, Orlando, FL, January 2010.

[51] J. Meyers and P. Sagaut. Is plane-channel flow a friendly case for the testing of large-eddy simulation subgrid-scale models ? *Phys. Fluids*, 19(048105):1–4, 2007.

[52] R. Mikkelsen. *Actuator Disc Methods Applied to Wind Turbines*. PhD thesis, Techical University of Denmark (DTU), 2003.

[53] J. Mohd-Yusof. Combined immersed-boundary/B-spline methods for simulations of ow in complex geometries. *Annu. Res. Briefs. NASA Ames Res. Cent.*, pages 317–327, 1997.

[54] P. Moin and J. Kim. Numerical investigation of turbulent channel flow. *J. Fluid Mech.*, 118:341 – 377, 1982.

[55] P. Moin, W. C. Reynolds, and J. H. Ferziger. Large eddy simulation of incompressible turbulent channel flow. Technical Report May 1978, NASA, Stanford, California, 1978.

[56] P. J. Moriarty and A. C. Hansen. AeroDyn Theory Manual. Technical Report January, NREL/TP-500-36881, 2005.

[57] R. D. Moser, J. Kim, and N. N. Mansour. Direct numerical simulation of turbulent channel flow up to $Re_\tau = 590$. *Phys. Fluids*, 11(4):943–945, 1999.

[58] F. Nicoud, H. Baya Toda, O. Cabrit, S. Bose, and J. Lee. Using singular values to build a subgrid-scale model for large eddy simulations. *Phys. Fluids*, 23(8):085106, 2011.

[59] F. Nicoud and F. Ducros. Subgrid-Scale Stress Modelling Based on the Square of the Velocity Gradient Tensor. *Flow, Turbul. Combust.*, 62:183–200, 1999.

[60] K. Nilsson, S. Ivanell, K. S. Hansen, R. F. Mikkelsen, J. N. Sørensen, S.-P. Breton, and D. S. Henningson. Large-eddy simulations of the Lillgrund wind farm. *Wind Energy*, 17(February 2014):657–669, 2014.

[61] P. Orlandi. *Fluid Flow Phenomena: a numerical toolkit*. Kluwer Academic Publishers, 2000.

[62] P. Orlandi and S. Leonardi. DNS of turbulent channel flows with two- and three-dimensional roughness. *J. Turbul.*, 7(53):1–23, jan 2006.

[63] H. Ouvrard, B. Koobus, A. Dervieux, and M. V. Salvetti. Classical and variational multiscale LES of the flow around a circular cylinder on unstructured grids. *Comput. Fluids*, 39(7):1083–1094, Aug. 2010.

[64] R. Peyret and T. Taylor. *Computational Methods for Fluid Flow*. Springer Series in Computational Physics. Springer-Verlag, 1983.

[65] S. B. Pope. *Turbulent flows*. Cambridge University Press, first edition edition, 2000.

[66] F. Porté-Agel, H. Lu, and Y.-T. Wu. A large-eddy simulation framework for wind energy applications. *CWE2010*, page 21, 2010.

[67] F. Porté-Agel, Y.-T. Wu, H. Lu, and R. J. Conzemius. Large-eddy simulation of atmospheric boundary layer flow through wind turbines and wind farms. *J. Wind Eng. Ind. Aerodyn.*, 99(4):154–168, Apr. 2011.

[68] L. Prandtl. Motion of fluids with very little viscosity. *NACA Tech. Memo.*, 452, 1928.

[69] L. Prandtl. Report on investigation of developed turbulence. *NACA Tech. Memo.*, 1231:1–8, 1949.

[70] W. Rankine. On the mechanical principles of the action of propellers. *Transactions of the Royal Institution of Naval Architects*, 6:13–39, 1865.

[71] P. Sagaut. *Large Eddy Simulation for Incompressible Flows: An Introduction*. Scientific Computation. Springer, 2000.

[72] M. V. Salvetti. Modellistica della turbolenza. Slide per il corso di Modellistica della Turbolenza – *Università di Pisa* A.A. 2005/2006.

[73] M. V. Salvetti and S. Banerjee. A priori tests of a new dynamic subgrid-scale model for finite-difference large-eddy simulations. *Phys. Fluids*, 7(11):2831–2847, 1995.

[74] C. Santoni and S. Leonardi. Effect ot tower and nacelle in the wake of a wind turbine. Submitted to Wind Energy (2015).

[75] H. Sarlak, C. Meneveau, and J. N. Sørensen. Role of subgrid-scale modelling in large eddy simulation of wind turbine wake interactions. *Renew. Energy*, 77:386–399, 2014.

[76] H. Schlichting and G. K. *Boundary layer theory*. Springer-Verlag, 8th edition edition, 2000.

[77] U. Schumann. *Ein Verfahren zur direkten numerischen Simulation turbulenter Strömungen in Platten- und Ringspaltkanälen und über seine anwendung zur Untersuchung von Turbulenzmodellen.* Ph.d dissertation, Universität Karlsruhe (TH), 1973.

[78] U. Schumann. Subgrid Scale Model for Finite Difference Simulations of Turbulent Flows in Plane Channels and Annuli. *J. Comput. Phys.*, 18:376–404, 1975.

[79] J. Smagorinsky. General ciruclation experiments with the primitive equations. *Mon. Weather Rev.*, 91(3):99–164, 1963.

[80] J. Smagorinsky, S. Manabe, and J. L. Holloway. Numerical Results From a Nine-Level General Circulation Model of the Atmosphere 1. *Mon. Weather Rev.*, 93:727–768, 1965.

[81] J. N. Sørensen. Aerodynamic Aspects of Wind Energy Conversion. *Annu. Rev. Fluid Mech.*, 43(1):427–448, 2011.

[82] J. N. Sørensen, R. F. Mikkelsen, D. S. Henningson, S. Ivanell, S. Sarmast, and S. J. Andersen. Simulation of wind turbine wakes using the actuator line technique. *Philos. Trans. thr R. Soc.*, 373(29149971):1–16, 2015.

[83] J. N. Sørensen and W. Z. Shen. *Computation of Wind Turbine Wakes using Combined Navier-Stokes/Actuator-line Methodology*, pages 156–159. EWEA, 1999.

[84] P. R. Spalart. Direct simulation of a turbulent layer up to $Re_\theta = 1410$. *J. Fluid Mech.*, 187:61–98, 1988.

[85] F. S. Stoddard. Discussion Of Momentum Theory For Windmills. Technical report, University of Massachusettes/Amherst, Amherst, Massachusetts 01002, 1976.

[86] N. Troldborg. *Actuator Line Modeling of Wind Turbine Wakes.* Phd thesis, Techical University of Denmark (DTU), Lyngby, 2008.

[87] N. Troldborg, J. N. Sørensen, and R. Mikkelsen. Numerical simulations of wakes of wind turbines operating in sheared and turbulent inflow. In *Eur. Wind Energy Conf. Exhib. 2009, EWEC 2009*, volume 2, pages 1374–1396, 2009.

[88] E. R. Van Driest. On Turbulent Flow Near a Wall. *J. Aeronaut. Sci. (Institute Aeronaut. Sci.)*, 23(11):1007–1011, 1956.

[89] O. V. Vasilyev, T. S. Lund, and P. Moin. A General Class of Commutative Filters for LES in Complex Geometries. *J. Comput. Phys.*, 146(1):82–104, Oct. 1998.

[90] T. von Kármán. Mechanical Similitude and Turbulence. *NACA Tech. Memo.*, 661:1–22, 1930.

[91] A. W. Vreman. An eddy-viscosity subgrid-scale model for turbulent shear flow: Algebraic theory and applications. *Phys. Fluids*, 16(10):3670–3681, 2004.

[92] B. Vreman, B. Geurts, and H. Kuerten. Realizability conditions for the turbulent stress tensor in large-eddy simulation. *J. Fluid Mech.*, 278:351, 1994.

[93] R. E. Wilson and P. B. S. Lissaman. *Applied Aerodynamics of Wind Power Machines*. Oregon State University, Corvallis, Oregon 97331, 1974.

[94] Y.-T. Wu and F. Porté-Agel. Large-Eddy Simulation of Wind-Turbine Wakes: Evaluation of Turbine Parametrisations. *Boundary-Layer Meteorol.*, 138(3):345–366, Dec. 2010.

[95] Y. T. Wu and F. Porte-Agel. Simulation of Turbulent Flow Inside and Above Wind Farms: Model Validation and Layout Effects. *Boundary-Layer Meteorol.*, 146(2):181–205, 2013.

[96] Y.-T. Wu and F. Porté-Agel. Modeling turbine wakes and power losses within a wind farm using LES: An application to the Horns Rev offshore wind farm. *Renew. Energy*, 75:945–955, Mar. 2015.

[97] Y. Zang, R. L. Street, and J. R. Koseff. A dynamic mixed subgrid-scale model and its application to turbulent recirculating flows. *Phys. Fluids A Fluid Dyn.*, 5(12):3186, 1993.